

UC Irvine

UC Irvine Electronic Theses and Dissertations

Title

The Study of Dusty Star-Forming Galaxies Through Far-Infrared Observations

Permalink

<https://escholarship.org/uc/item/3xx7t5mz>

Author

Calanog, Jae Alyson Basada

Publication Date

2014

Peer reviewed|Thesis/dissertation

UNIVERSITY OF CALIFORNIA,
IRVINE

The Study of Dusty Star-Forming Galaxies in the Early Universe Through Far-Infrared
Observations

DISSERTATION

submitted in partial satisfaction of the requirements
for the degree of

DOCTOR OF PHILOSOPHY

in Physics

by

Jae Alyson Calanog

Dissertation Committee:
Professor Asantha Cooray, Chair
Professor Michael Cooper
Professor Steve Barwick

2014

DEDICATION

To all the giants whose shoulders I've stood upon.

TABLE OF CONTENTS

	Page
LIST OF FIGURES	v
LIST OF TABLES	vi
ACKNOWLEDGMENTS	vii
CURRICULUM VITAE	viii
ABSTRACT OF THE DISSERTATION	xi
1 Introduction	1
1.1 <i>Herschel</i> Space Observatory	3
1.1.1 <i>Herschel</i> -SPIRE Surveys	3
1.2 Dust-Obscured Galaxies	4
1.2.1 Mid-Infrared Selection of High Redshift Galaxies	4
1.2.2 Properties of Dust-Obscured Galaxies	6
1.2.3 <i>Herschel</i> 's Role in Studying Dust Obscured Galaxies	7
1.3 Sub-millimeter Galaxies	9
1.3.1 The Negative K-Correction	9
1.3.2 Properties of Sub-millimeter Galaxies	10
1.3.3 Observational Challenges	12
1.4 The Discovery Of HFLS3: A Starbursting Galaxy At $z=6.34$	15
2 The Far-Infrared Emission from Dust Obscured Galaxies	17
2.1 Background	17
2.2 Data and Sample Selection	20
2.2.1 Far-Infrared Data	20
2.2.2 Optical and Mid-Infrared Data	20
2.2.3 Sample Selection	21
2.2.4 Redshifts	22
2.3 Analyses and Results	25
2.3.1 Far-Infrared Spectral Energy Distributions	25
2.3.2 Infrared Luminosity Function at $z \sim 2$	32
2.3.3 Stellar Mass Build-up	38

3	Gravitationally Lensed <i>Herschel</i>-selected Galaxies	42
3.1	Background	42
3.2	Lensed Candidate Selection and near-IR Observations	47
3.2.1	Selection of Lensed Candidates	47
3.2.2	Keck NIRC2/LGS-AO	50
3.2.3	HST/WFC3	51
3.3	Classification of Lensing Candidates	53
3.3.1	Visual Identification of Lensing Morphologies	53
3.3.2	Redshift Availability	55
3.3.3	Near-IR Strong Lensing Identification Efficiency	56
3.4	Lens Models	58
3.4.1	General Methodology	58
3.4.2	Notes on Individual Lens Models	63
3.5	Results and Discussion	76
3.5.1	Differential Lensing and Source Sizes	76
3.5.2	Morphological Comparison With Previous Near-IR Studies of SMGs .	83
3.5.3	Rest-Frame Optical Photometry	85
4	HFLS3: A Massive Dust-Obscured Starburst at $z = 6.34$	90
4.1	Background	90
4.2	<i>Hubble Space Telescope</i> Observations	93
4.3	Rest-frame UV fluxes of HFLS3	97
4.4	Lens Modeling	97
4.5	SED Modeling	103
4.6	Discussion	107
5	Conclusions	116
5.1	Summary of Main Results	117
5.1.1	The Far-Infrared Emission From Dust-Obscured Galaxies	117
5.1.2	Gravitationally Lensed <i>Herschel</i> -selected Galaxies	118
5.1.3	The Rest-Frame UV Emission of HFLS3	119
5.2	Future Studies:	120
	Bibliography	124
A	Data Tables and Supplementary Figures	135
A.1	Data Tables for <i>Herschel</i> Lensed Candidates	135
A.2	Lens Models using Sub-mm Parameters	144
A.3	Supplementary Near-IR Images	146

LIST OF FIGURES

	Page
1.1 Spectral Energy Distributions of the Background Light	2
1.2 Examples of mid-IR SEDs for DOGs.	5
1.3 Composite SED of bump (star-forming) DOGs.	8
1.4 Negative K-Correction for LIRGs.	11
1.5 Multi-wavelength Image Stamps of SMGs.	13
2.1 r^+ -[24] as a function of 24 μm flux.	23
2.2 Photometric redshift distribution of DOGs in the COSMOS field.	24
2.3 Sample FIR SED fits for DOGs.	27
2.4 Sample FIR stacking results of DOGs observed by <i>Herschel</i>	28
2.5 IR luminosity as a function of redshift for DOGs.	30
2.6 Dust temperatures and IR luminosities for DOGs.	31
2.7 IR luminosity function of DOGs at $z \sim 2$	33
2.8 Star formation rate density (ρ_{SFR}) of all DOGs.	35
2.9 Star formation rates and specific star-formation rates for DOGs at $z \sim 2$	39
3.1 S_{350}/S_{500} and S_{500} for SPIRE galaxies in HerMES and H-ATLAS.	48
3.2 Cumulative frequency distribution of S_{500}	54
3.3 Grade 1 lensed candidates	59
3.4 Near-IR lens models of Grade 1 systems.	65
3.5 Comparison of near-IR and sub-mm magnifications	78
3.6 Intrinsic sizes of SMGs in the near-IR and sub-mm.	80
3.7 Near-IR magnifications and sizes for lensed SMGs.	82
3.8 Intrinsic M_B and redshift.	88
3.9 Intrinsic M_B and S_{500} for lensed SMGs.	89
4.1 HST imaging of HFLS3.	95
4.2 <i>Spitzer</i> IRAC Image of HFLS3.	96
4.3 Lens Model of HFLS3.	100
4.4 Probability distribution function of μ_{lens}	102
4.5 SEDs and best-fit HYPERZ models for the HFLS3 lensing system.	104
4.6 Best-fit composite SED of HFLS3.	106

LIST OF TABLES

	Page
2.1 SPIRE Stacking Results	28
2.2 Average DOG IR Luminosities and Dust Temperatures	30
2.3 The IR Luminosity Function for DOGs at $z = 1.5 - 2.5$	36
3.1 Grading Rubric Summary for Lensed SMGs	55
3.2 Properties of the Foreground Lenses of Grade 1 Systems	74
3.3 Properties of the Background Lensed Galaxy for Grade 1 Systems.	75
3.4 Near-IR Photometry of Lensed SMGs	86
4.1 IR Properties of HFLS3 and Nearby Galaxies	112
A.1 Summary of High Resolution Data	136
A.2 Observed Properties of SMG Lens Candidates	140

ACKNOWLEDGMENTS

Firstly, I would like to thank Professor Asantha Cooray for getting me involved with interesting research projects and surrounding me with the best collaborators in my field of study. As an advisor, he has provided me with everything I have needed in order to be successful, which includes (and not limited to) his mentorship, research funding, and networking opportunities.

Secondly, I'd like to thank Dr. Julie Wardlow and Professor Hai Fu for everything you've taught me in this field. Both have been instrumental in my development as a scientist and I appreciate all of our insightful discussions. I am also grateful for the assistance of all of my collaborators: Joseph Smidt, Sam Kim, Jon Michael O'Bryan, Cameron Thacker, Ketrion Mitchell-Wynne, Ryan Keeley, Ali Khostovan, Chris Frazer, Brian Ma, Alex Chiu, Nicholas Timmons, Willow Osage, Ryan Keeley, Carrollann Simmons, and everyone from the HerMES and H-ATLAS collaborations.

Thirdly, I would like to thank my family, for their support and encouragement throughout my graduate schooling. Special thanks also goes out to my better half, Aizel Agustino and her family for all of the weekend getaways in San Diego, for housing and feeding me, and any kind of assistance you've provided me in the last 4 years. To Claire Dorman and Samuel Halverson, thank you for positively peer-pressuring me to go to graduate school and continuing to be a source of inspiration. For all the (break)dancers with whom I connected with, you also have my gratitude for providing me a healthy, creative outlet during difficult times.

I would like to acknowledge financial support from the GAANN fellowship, Presidential Dissertation Year Fellowship, and NSF AST-1313319.

This thesis has made use of data from the HerMES project (<http://hermes.sussex.ac.uk/>). HerMES is a Herschel Key Programme utilizing Guaranteed Time from the SPIRE instrument team, ESAC scientists and a mission scientist. The data presented in this paper is released through the HerMES Database in Marseille, HeDaM (<http://hedam.oamp.fr/HerMES/>). In addition, I also use Herschel-ATLAS data in this thesis. H-ATLAS is a project with Herschel, which is an ESA space observatory with science instruments provided by European-led Principal Investigator consortia and with important participation from NASA. The H-ATLAS website is <http://www.h-atlas.org/>.

The text of this thesis/dissertation is a reprint of the material as it appears in “HerMES: The Far-IR Emission From Dust-Obscured Galaxies” (ApJ, 771, 65), “Lens Models of Herschel-Selected Galaxies From High-Resolution Near-IR Observations” (ApJ, submitted), “HerMES: The Rest-Frame UV Emission and A Lensing Model for the $z=6.34$ Luminous Dusty Starburst Galaxy HFLS3” (ApJ, accepted). The co-authors listed in these publications directed and supervised research which forms the basis for the thesis/dissertation. Finally, I would like to acknowledge the Astrophysical Journal and the American Astronomical Society for granting me permission to reproduce my previous work in this thesis.

CURRICULUM VITAE

Jae Alyson Calanog

EDUCATION

Doctor of Philosophy in Physics	2014
University of California, Irvine	<i>Irvine, CA</i>
Masters of Science in Physics	2012
University of California, Irvine	<i>Irvine, CA</i>
Bachelors of Arts in Physics	2009
University of California, Berkeley	<i>Berkeley, CA</i>

RESEARCH EXPERIENCE

Graduate Student Researcher	2011–2014
University of California, Irvine	<i>Irvine, California</i>
Undergraduate Research Apprentice	2008–2009
University of California, Berkeley	<i>Berkeley, California</i>
Lawrence Berkeley Laboratory Summer Research Intern	2008
University of California, Berkeley	<i>Berkeley, California</i>

TEACHING/OUTREACH EXPERIENCE

California Community College Intern	2013–2014
University of California, Irvine/Santa Ana College	<i>Irvine/Santa Ana, CA</i>
Math and Physics Tutor	2013–2014
a College Trail Tutors	<i>Laguna Beach, CA</i>
Founder of ReREAD	2012
University of California, Irvine	<i>Irvine, CA</i>
Astronomy Outreach Volunteer	2011–2012
University of California, Irvine	<i>Irvine, CA</i>
Graduate Student Instructor	2010–2011
University of California, Irvine	<i>Irvine, CA</i>

TELESCOPE EXPERIENCE

Keck-NIRC2 LGS/AO
Keck-NIRSPEC

> 40 hours
> 20 hours

PROFESSIONAL TRAINING

Astro 101: Approaches For Teaching A Diverse Audience Workshop (2013)
NASAs Center for Astronomy Education Tier I Workshop (2012)
UCO Graduate Student Observing Workshop (2011)
East Bay Consortiums Prospective Teacher Program (2009)
LBNL Center for Science and Engineering Education s Preservice Teacher Program (2008)
UC Berkeley California Math and Science Teaching Program (2007-2008)

REFEREED JOURNAL PUBLICATIONS

First-authored:

Lens Models of *Herschel*-Selected Galaxies From High-Resolution Near-IR Observations 2014
ApJ, submitted

HerMES: The Far-IR Emission of Dust-Obscured Galaxies 2013
ApJ, accepted

Co-authored:

HerMES: The Rest-Frame UV Emission and A Lensing Model for the $z=6.34$ Luminous Dusty Starburst Galaxy HFLS3 (Cooray et al.) 2014
ApJ, submitted

Constraining the Lyman Alpha Escape Fraction with Far-Infrared Observations of Lyman Alpha Emitters (Wardlow et al.) 2014
ApJ, accepted

Gravitational Lens Models Based on Submillimeter Array Imaging of *Herschel*-selected Strongly Lensed Submillimeter Galaxies at $z>1.5$ (Bussmann et al.) 2013
ApJ, accepted

A Gas-Rich Major Galaxy Merger at $z=2.3$ Signposts to a Massive Galaxy In Formation (Fu et al.)	2013
Nature, accepted	
The Discovery of a Dust-Obscured Massive Hyper Starburst Galaxy at $z=6.34$ (Riechers et al.)	2013
Nature, accepted	
H-ATLAS: A Binary HYLIRG Pinpointing a Cluster of Starbursting Proto- Ellipticals (Iverson et al.)	2013
ApJ, accepted	
HerMES: Candidate Gravitationally Lensed Galaxies and Lensing Statistics at Submillimeter Wavelengths (Wardlow et al.)	2013
ApJ, accepted	
Lensed Galaxies in CANDELS (Cooray et al.)	2011
ApJ, submitted	

Talks/Presentations

Talk: Gravitationally Lensed Sub-millimeter Galaxies	2014, April
University of California, Santa Cruz Friday Lunch Astrophysics Seminar Hour	
Poster: Far-IR Emission of Dust-Obscured Galaxies in COSMOS	2013, January
221st AAS Conference	
Poster: Far-IR Properties of Dust-Obscured Galaxies in the Boötes Field at $z \approx 2$	2012, January
219th AAS Conference	

ABSTRACT OF THE DISSERTATION

The Study of Dusty Star-Forming Galaxies in the Early Universe Through Far-Infrared Observations

By

Jae Alyson Calanog

Doctor of Philosophy in Physics

University of California, Irvine, 2014

Professor Asantha Cooray, Chair

In this thesis I use far-infrared (far-IR) observations performed by the *Herschel Space Observatory* to study dusty star-forming galaxies, which are believed to be the likely progenitors of massive elliptical galaxies. More specifically, I investigate the far-IR emission of dust-obscured galaxies (DOGs), analyze the near-IR imaging of *Herschel*-selected lensed galaxies, and investigate the rest-frame UV emission of HFLS3, a $z = 6.34$ *Herschel*-selected starburst.

DOGs are a UV-faint, infrared-bright galaxy population that reside at $z \sim 2$ and are believed to be in a phase of dusty star-forming and AGN activity. I present far-IR observations of a complete sample of DOGs in the 2 deg^2 of the Cosmic Evolution Survey (COSMOS). The 3077 DOGs have $\langle z \rangle = 1.9 \pm 0.3$ and are selected from $24 \mu\text{m}$ and r^+ observations using a color cut of $r^+ - [24] \geq 7.5$ (AB mag) and $S_{24} \geq 100 \mu\text{Jy}$.

Based on the mid-IR spectral energy distributions, 47% are bump DOGs (star-formation dominated) and 10% are power-law DOGs (AGN-dominated). I use SPIRE far-IR photometry from the *Herschel* Extragalactic Multi-tiered Survey (HerMES) to calculate the IR luminosity and characteristic dust temperature for the 1572 (51%) DOGs that are detected at $250 \mu\text{m}$ ($\geq 3\sigma$). For the remaining 1505 (49%) that are undetected, I perform a median stacking analysis to probe fainter luminosities.

I find that detected and undetected DOGs have average luminosities of $(2.8 \pm 0.4) \times 10^{12} L_{\odot}$ and $(0.77 \pm 0.08) \times 10^{12} L_{\odot}$, and dust temperatures of (34 ± 7) K and (31 ± 3) K, respectively. DOGs contribute 30% to the $24 \mu\text{m}$ -selected galaxies' infrared luminosity function, calculated using far-infrared data. If the IR luminosity is extrapolated using the $24 \mu\text{m}$ flux density alone, it is overestimated by a factor of 2 on average.

DOGs contribute 10 – 30% to the total star formation rate density of the Universe at $z = 1.5 - 2.5$, dominated by $250 \mu\text{m}$ detected and bump DOGs, compared to around 40% for all $24 \mu\text{m}$ galaxies above our flux limit. DOGs have a large scatter about the star-formation main sequence and their specific star-formation rates show that the observed phase of star-formation could be responsible for their observed stellar mass at $z \sim 2$.

In the second part of this thesis, I present Keck-Adaptive Optics and *Hubble Space Telescope* high resolution near-IR imaging for SPIRE $500 \mu\text{m}$ -bright lensed candidates identified by the *Herschel* Multi-tiered Extragalactic Survey (HerMES) and *Herschel* Astrophysical Terahertz Survey (H-ATLAS). Out of 87 candidates with near-IR imaging, 16 ($\sim 18\%$) display clear near-IR lensing morphologies.

I derive near-IR lens models to reconstruct and recover basic rest-frame optical morphological properties of the background galaxies from 12 new systems. Sources with the largest μ_{NIR} also tend to be the most compact, consistent with the size bias predicted from simulations and previous lensing models for sub-millimeter galaxies.

For four sources that also have high-resolution sub-mm maps, I test for differential lensing between the stellar and dust components and find that the $880 \mu\text{m}$ magnification factor (μ_{880}) to be ~ 1.5 times higher than the near-IR magnification factor (μ_{NIR}), on average. I also find that the stellar emission is ~ 2 times more extended in size than dust. The rest-frame optical properties of our sample are consistent with that of unlensed SMGs, indicating that they are similar populations assuming similar star-formation histories and levels of dust obscuration.

In the final chapter, I discuss the rest-frame ultraviolet emission from the starbursting galaxy HFLS3 at a redshift of 6.34. The galaxy was discovered in *Herschel*/SPIRE data due to its *red* color in the sub-mm wavelengths from 250 to 500 μm .

The apparent instantaneous star-formation rate of HFLS3 inferred from the total far-IR luminosity measured with over 15 photometric data points between 100 and 1000 μm is $2900 M_{\odot} \text{yr}^{-1}$. Keck/NIRC2 K_s -band adaptive optics imaging data showed two potential near-IR counterparts near HFLS3. Previously, the northern galaxy was taken to be in the foreground at $z = 2.1$ while the southern galaxy was assumed to be HFLS3's near-IR counterpart.

The recently acquired *Hubble*/WFC3 and ACS imaging data show conclusively that both optically-bright galaxies are in the foreground at $z < 6$. A new lensing model based on the *Hubble* imaging data and the mm-wave continuum emission yields a magnification factor of 2.2 ± 0.3 . The lack of multiple imaging constrains the lensing magnification to be lower than either 2.7 or 3.5 at the 95% confidence level for the two scenarios, which attribute one or two components to HFLS3 in the source plane.

Once accounting for the possibility of gravitational lensing, the instantaneous star-formation rate is $1320 M_{\odot} \text{yr}^{-1}$ with the 95% confidence lower limit around $830 M_{\odot} \text{yr}^{-1}$. Using models for the rest-frame UV to far-IR spectral energy distribution (SED) we determine the average star-formation rate over the last 100 Myr to be around $660 M_{\odot} \text{yr}^{-1}$. The dust and stellar masses of HFLS3 from the same SED models are at the level of $3 \times 10^8 M_{\odot}$ and $\sim 5 \times 10^{10} M_{\odot}$, respectively, with large systematic uncertainties on assumptions related to the SED model.

With *Hubble*/WFC3 images we also find diffuse near-IR emission about 0.5 arcseconds (~ 3 kpc) to the South-West of HFLS3 that remains undetected in the ACS imaging data. The emission has a photometric redshift consistent with either $z \sim 6$ or a dusty galaxy template at $z \sim 2$. If at the same redshift as HFLS3 the detected diffuse emission could be part of

the complex merger system that could be triggering the starburst. Alternatively, it could be part of the foreground structure at $z \sim 2.1$ that is responsible for lensing of HFLS3.

Chapter 1

Introduction

Far-infrared observations have proved invaluable in probing the early Universe. Its significance was initially demonstrated when the first measurements of the energy spectrum from the cosmic far-IR background was observed to approximately equal the optical background (Fig. 1.1; Puget et al., 1996; Fixsen et al., 1998; Hauser et al., 1998; Schlegel et al., 1998; Lagache et al., 1998). This discovery implied that $\sim 50\%$ of the integrated rest-frame ultraviolet (UV) and optical light can be observed as thermally reprocessed radiation emitted by dust in far-IR wavelengths. Hence, the star-formation rate (SFR) derived from optical and UV measurements represented a lower limit, with a significant fraction being missed without accounting for the far-IR contribution (Madau et al., 1998). This issue worsens at higher redshifts, since the total comoving infrared luminosity density evolves as $\propto (1+z)^4$ out to $z \sim 1$ (Le Flocc'h et al., 2005) whereas the ultraviolet density displays a slower evolution, $\propto (1+z)^{1.5-2.5}$ (Wilson et al., 2002; Oesch et al., 2010). Therefore, at $z \gtrsim 0.7$, dust-enshrouded star-formation dominates the total star-formation activity.

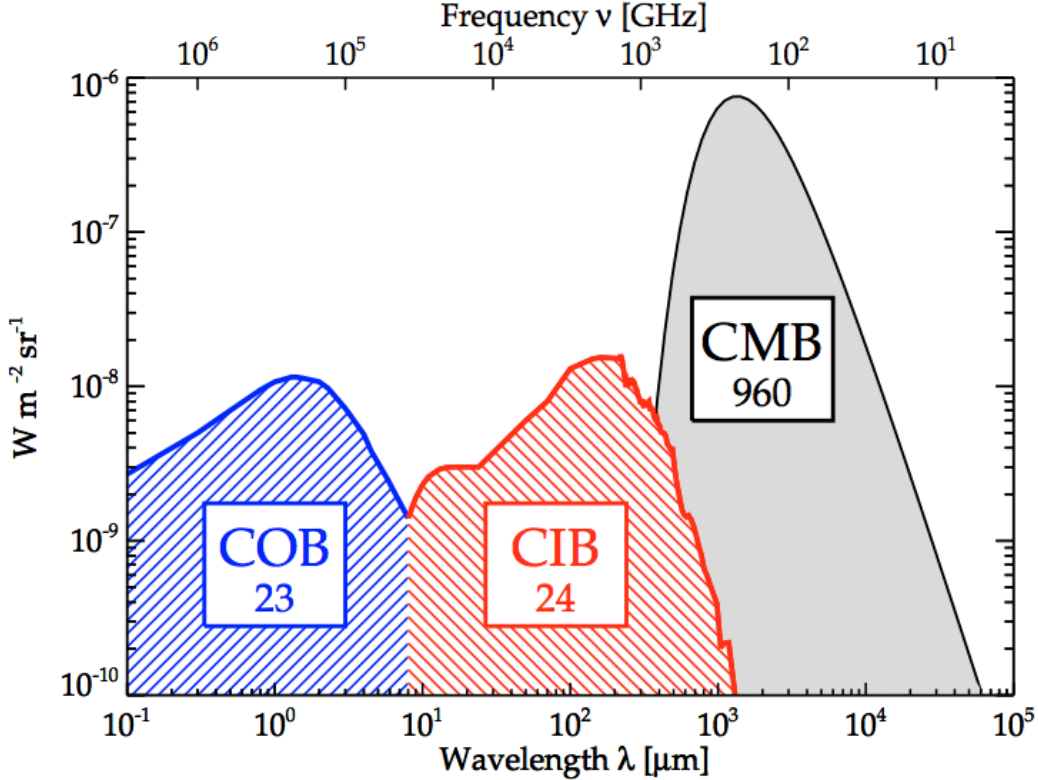


Figure 1.1: Spectral Energy Distributions of the Background Light

This figure is reproduced from Dole et al. (2006) with permission from the authors and AAS. It shows the energy spectrum from the cosmic optical background (COB), cosmic infrared background (CIB), and cosmic microwave background (CMB). The integrated intensity for each wavelength regime is written inside the boxes. The optical and infrared background light have roughly equal contributions to the extragalactic background light.

The results from measuring the cosmic infrared background left a strong impression to astronomers at the time that a population of infrared-luminous galaxies were waiting to be discovered. It would take almost a decade later until the blank field pointings of Sub-millimeter Common-User Array (SCUBA, Holland et al., 1999) mounted on the James Clerk Maxwell Telescope (JCMT) detected far-IR/sub-mm bright and optically faint galaxies for the first time (Smail et al., 1997; Barger et al., 1998; Hughes et al., 1998). Since their initial discovery, many instruments that performed ground, balloon, and space-based observations in the mid-infrared, far-IR, and sub-mm wavelength regimes have become operational and have identified different populations of infrared luminous galaxies. As a result, the study of dusty star-forming galaxies at high redshift have become an observational testbed for theories on

galaxy evolution and formation.

1.1 *Herschel* Space Observatory

The *Herschel* Space Observatory (Pilbratt et al., 2010) has provided the deepest and largest view of the far-IR Universe during the four years (May 2009 - April 2013) it was operational. It had two cameras, the Photodetector Array Camera and Spectrometer (PACS Poglitsch et al., 2010) and the Spectral Photometric and Imaging Receiver (SPIRE, Griffin et al., 2010; Swinyard et al., 2010). PACs observed in shorter far-IR wavelengths at 70, 100, and 160 μm that reached sensitivities of 0.4, 0.4, and 0.9 mJy, respectively and spatial resolutions of 5'', 7'', and 12'', respectively. SPIRE observed at 250, 350, and 500 μm and was confusion limited at 5.8, 6.3, and 6.8 mJy, respectively, while achieving spatial resolutions of 18'', 26'', and 36'', respectively. For comparison, the *Spitzer* Multiband Imaging Photometer and Spectrometer (MIPS, 2003-2009, Rieke et al., 2004), which also observed at 70 and 160 μm had beam sizes that were larger by a factor of three and sensitivities shallower by a factor of 2 to 10. The Balloon-borne Large Aperture Sub-millimeter Telescope (BLAST, Devlin et al., 2004), which performed observations in 2006-2007 at 250, 350, and 500 μm , featured beam sizes and sensitivity depths that were roughly twice larger than SPIRE. Indeed, both instruments offered significant improvement over previous far-IR instruments. For this thesis, we focus on using the deep wide-area observations using the SPIRE instrument to perform our analysis on dusty star-forming galaxies at high redshift ($z \geq 1$).

1.1.1 *Herschel*-SPIRE Surveys

The *Herschel* Multi-tiered Extragalactic Survey (HerMES, Oliver et al., 2012) and the *Herschel* Astrophysical Terahertz Large Area Survey (H-ATLAS Eales et al., 2010) are the two

largest *Herschel* surveys. H-ATLAS has a total coverage area of 510 deg² of the sky that includes three fields on the equator, which coincides with the Galaxy And Mass Assembly Redshift Survey (GAMA, Driver et al., 2009), one field near the northern galactic plane (NGP) and two fields near the southern galactic plane (SGP). The H-ATLAS SPIRE maps reach a 5σ point source depth of 57, 62, and 64 mJy beam⁻¹, which includes confusion and instrumental noise in the 250, 350, and 500 μm bands (Pascale et al., 2011). Although the main goal of H-ATLAS was to calculate the dust-enshrouded star-formation and dust masses for nearby galaxies detected in the Sloan Digital Sky Survey (SDSS, Abazajian et al., 2003), in this thesis we also use H-ATLAS data to search for rare gravitationally lensed SMGs.

HerMES is the second largest *Herschel*-SPIRE survey, with a total area coverage of 380 deg². The main science goal of the survey is to understand galaxy formation and evolution by studying the dust properties of infrared luminous galaxies from intermediate to high redshifts. In order to successfully meet this goal, HerMES chose fields known to have ancillary data in all wavelengths and expects to detect 100, 000 galaxies at $\geq 5\sigma$. A summary of the covered fields are found in Table 5 of Oliver et al. (2012). Similarly to H-ATLAS, we use the SPIRE maps from HerMES to isolate bright sources that are lensed candidates through a far-IR/sub-mm flux density cut at 500 μm . However, we also use HerMES data to select the reddest ($S_{250} \geq S_{350} \geq S_{500}$) galaxies that could lie at higher redshifts (Dowell et al., 2014). The individual study of the $z = 6.3$ galaxy HFLS3 highlights this application.

1.2 Dust-Obscured Galaxies

1.2.1 Mid-Infrared Selection of High Redshift Galaxies

The launch of the *Spitzer Space Telescope* in 2003 allowed detailed studies of high-redshift luminous infrared galaxies (LIRGs) in the near to mid-infrared for the first time. Its in-

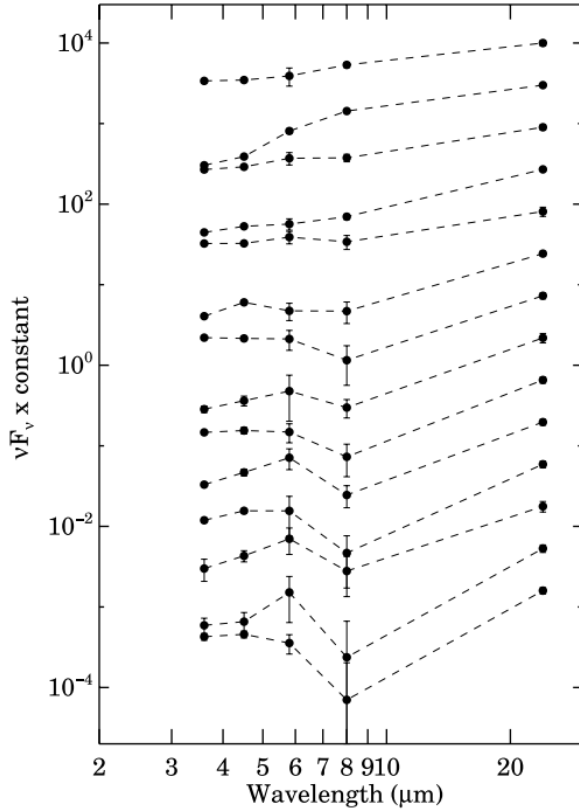


Figure 1.2: Examples of mid-IR SEDs for DOGs.

This figure is reproduced from Dey et al. (2008) with permission from the authors and AAS. The mid-infrared SEDs of DOGs from the observed $3 - 8 \mu\text{m}$ show a power-law feature or a local maximum, indicative of AGN or star-formation activity, respectively.

struments are able to observe in $3 - 25 \mu\text{m}$, which is a wavelength regime rich of spectral emission line features from polycyclic aromatic hydrocarbons (PAH). The detection of PAH emission lines at rest-frame ($6 - 12 \mu\text{m}$) is an indicator for ongoing star-formation while their absence and the presence of a mid-infrared continuum suggests that the observed emission is likely due to active galactic nuclei (AGN) activity. For these reasons, selection schemes that incorporated mid-infrared observations were used to efficiently select LIRGs (e.g. Yan et al., 2004; Brand et al., 2006; Yan et al., 2007; Dey et al., 2008).

Dust-obscured galaxies (DOGs, Dey et al., 2008) at $z \sim 2$ are among these LIRGs, selected for having $R - [24] \geq 14$ Vega or effectively, $F_{24}/F_R \geq 982$. This mid-infrared to optical selection was designed to select dusty star-forming galaxies that lie at $z \geq 1$ that have

no local counterparts (Dey et al., 2008). Above some flux density limit, the distribution of $24\ \mu\text{m}$ flux densities for DOGs is statistically indistinguishable to its parent sample, the $24\ \mu\text{m}$ bright population. This indicates that their large mid-infrared to optical flux density ratios is due to the attenuation of the rest-frame UV emission from severe dust obscuration (Penner et al., 2012).

The mid-infrared selection for DOGs selects a heterogeneous population of both star-forming galaxies and AGN. Analysis of their mid-infrared SEDs is required in order to discriminate between the two subpopulations. Figure 1.2 shows examples of typical mid-infrared SEDs of DOGs. At $z \sim 2$, DOGs that are dominated by star-formation typically feature a local maximum in the observed frame $3 - 8\ \mu\text{m}$, which is interpreted to be the rest-frame $1.6\ \mu\text{m}$ stellar bump present in older stellar populations (e.g. Simpson & Eisenhardt, 1999; Sawicki, 2002; Desai et al., 2009). Alternatively, DOGs that feature a power-law in their near-infrared SEDs are believed to host an AGN.

1.2.2 Properties of Dust-Obscured Galaxies

The current picture of how elliptical galaxies are formed shows their progenitors experiencing a rapid burst of star-formation that is likely followed by an episode of black-hole accretion. Feedback mechanisms either due to AGN or supernovae explosions expel gas reservoirs in the interstellar medium, effectively quenching star-formation and will eventually cause the galaxy to settle into the red sequence (e.g. Genzel et al., 2001; Farrah et al., 2003). In this context, previous studies have speculated that DOGs represent a transitional phase between the peaks of star-formation and AGN activity. The IR luminosities ($\geq 10^{12}L_{\odot}$), dust temperatures ($T_{\text{dust}} \sim 30 - 60\ \text{K}$), stellar masses ($M_{\text{DOGs}} \sim 1.5 - 2 \times M_{\text{SMGs}}$), clustering lengths ($\sim 7\ h^{-1}\text{Mpc}^{-3}$, Brodwin et al., 2008) and the SED shapes of DOGs are comparable with SMGs at $z \sim 2.5$ (Pope et al., 2008b; Bussmann et al., 2012), which suggest that these

two populations could be connected. Hydrodynamic N-body simulations of gas-rich galaxies undergoing an intense merger-driven phase of star-formation also show that DOGs can be selected as SMGs (Narayanan et al., 2010). This has also been supported observationally, as Pope et al. (2008b) found that 30% of their SMG sample are also selected as DOGs. Evidence in support for this evolutionary picture is also found within the two subpopulations of DOGs. From a morphological perspective, high-resolution optical and near-infrared observations reveal that bump DOGs are more extended ($r_{\text{eff}} \geq 8$ kpc), irregular galaxies than their power-law counterparts ($r_{\text{eff}} = 1 - 5$ kpc). These findings are consistent with the idea that merger-induced star-formation in galaxies will have extended diffuse surface brightness profiles that will evolve into more compact morphologies as AGN activity starts to dominate (Bussmann et al., 2009b, 2011).

1.2.3 *Herschel's* Role in Studying Dust Obscured Galaxies

Prior to wide-field deep far-IR surveys, studies on the cold dust properties of DOGs were limited. Although DOGs are mid-infrared bright, they are intrinsically faint in the far-IR. This was shown by Pope et al. (2008b) when SMG SED templates had to be scaled by a factor of 8 in order to match their stacked far-IR and sub-mm flux densities (Fig. 1.3). Moreover, the limited field of view of ground-based far-IR instruments resulted in small sample sizes. CSO/SHARC-II 350 μm observations of 24 DOGs by Bussmann et al. (2009a) only resulted in four $\geq 3\sigma$ detections (ignoring the contribution from confusion noise).

The advent of the *Herschel Space Observatory* in 2009 allowed deep far-IR observations of DOGs over a wide area, free from the observational limitations of ground-based far-IR instruments. The SPIRE channels sample near the rest-frame peak of the cold dust blackbody emission, placing constraints on the far-IR SEDs of DOGs at $z \sim 2$. The study of Melbourne et al. (2012) highlights the first application of *Herschel* observations on DOGs,

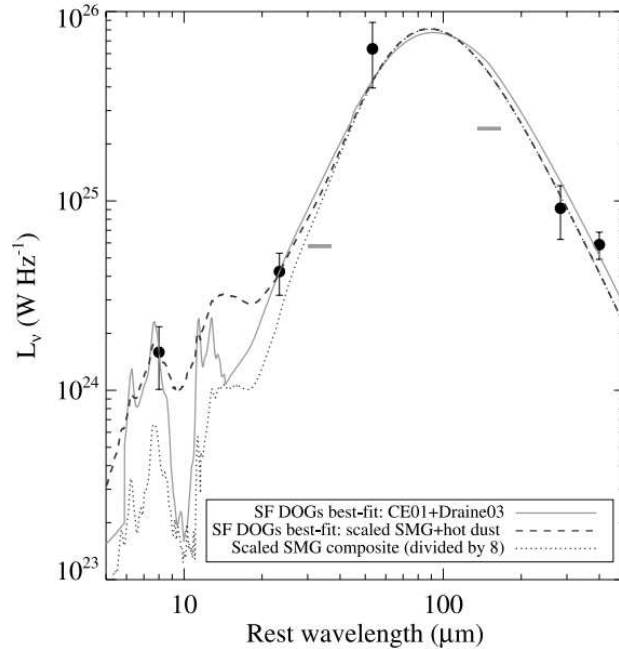


Figure 1.3: Composite SED of bump (star-forming) DOGs.

This figure has been reproduced from (Pope et al., 2008b) with permission from the authors and AAS. The filled symbols represent average fluxes and the solid line represents the best fit template model from Chary & Elbaz (2001)+Draine SED templates. The dotted curve is a composite SMG template from (Pope et al., 2008a) that was normalized by a factor of 8 to fit the observed far-IR and sub-mm fluxes. The dashed curve is a scaled composite SMG SED with a hot dust component ($T = 350$ K). DOG SEDs are similar to SMGs, in which their IR luminosities are dominated by a cold dust component with an average temperature of $T \sim 30$ K.

in which they analyzed the far-IR SEDs of 113 DOGs with spectroscopic redshifts covered in 9 deg^2 of the Boötes field. By comparing mid and far-IR flux density ratios with local ultra-luminous infrared galaxies (ULIRGs, $L_{\text{IR}} \geq 10^{12} L_{\odot}$), they found that power-law DOGs have SEDs similar to local quasi-stellar object (QSO) Mrk231 while bump DOGs resemble NGC 6240, a local star-bursting ULIRG believed to be major merger remnant with two AGN.

In this thesis, we extend the study of DOGs in the far-IR. Using a complete sample of ~ 3000 DOGs with $S_{24} \geq 80 \text{ mJy}$ in the Cosmic Evolution Survey (COSMOS, Scoville et al., 2007) field and HerMES SPIRE data, we derive their IR luminosity function and calculate their contribution to the total dust-enshrouded star-formation rate density (ρ_{SFR}) at $z \sim 2$. We note that previous studies of DOGs have dealt with incomplete samples due to the lack of available redshifts, and our study uses both spectroscopic and accurate photometric redshifts ($\sigma_z/(1+z) = 0.02$ for sources with $z = 1.5 - 3$ and the same range in Subaru r^+ band) derived from 30 bands of photometry.

1.3 Sub-millimeter Galaxies

1.3.1 The Negative K-Correction

The term K-correction (Hogg et al., 2002) refers to the correction applied to an observed absolute magnitude (or flux) in order to convert it into an equivalent measurement in the rest frame of the object. Observations through a single band only covering a fraction of the spectrum require a K-correction, which is derived from the inferred shape of the SED. Similar to the convention used in magnitudes, a K-correction is “positive” if an object gets fainter with increasing redshift and is “negative” if it gets brighter with increasing redshift.

Galaxies selected for being bright at sub-millimeter wavelengths experience a negative K-

correction. This is because the rest-frame far-IR SED resembles a blackbody that peaks at $\lambda \sim 100 \mu\text{m}$. Classical SMGs are selected for being bright at $850 - 880 \mu\text{m}$, which at $z \geq 1$ lies within the long wavelength regime of cold dust emission referred to as the Rayleigh-Jeans tail. In this region of the SED at $0.5 \leq z \leq 3$, the observed flux density at some frequency, S_ν , behaves as $S_\nu(z) \propto \nu^{2+\beta}/(1+z)^4 \propto \nu_{\text{rest}}^{2+\beta}(1+z)^{2+\beta}/(1+z)^4$, where ν is the observed frequency, ν_{rest} is the rest-frame frequency, and β is the emissivity spectral index. Previous findings from studying dusty star-forming galaxies show that $\beta = 1 - 2$ (Hildebrand, 1983; Dunne & Eales, 2001; Draine, 2003a; Chapin et al., 2011) and is usually fixed to equal 1.5. Therefore, the observed flux density can be approximated to be constant, which equivalently defines an almost uniform infrared luminosity limit, across a wide range of redshift (Fig. 1.4).

1.3.2 Properties of Sub-millimeter Galaxies

Since their discovery in the late 1990's, our knowledge about SMG properties have grown. As their name implies, SMGs are sub-millimeter bright and are typically selected to have $S_{850} \geq 5$ mJy. They lie at $z \sim 2.5$ (Chapman et al., 2005; Wardlow et al., 2011; Simpson et al., 2013), confirmed using both spectroscopic (OII, OIII, H α , Ly α emission line identifications) and photometric methods (SED fitting of ≥ 15 bands of optical to mid-infrared photometry) to measure their redshifts. SMGs are rich in cold dust, indicated by the prominent dust peak at rest-frame $\sim 100 \mu\text{m}$. This is also reflected in their measured IR luminosities $L_{\text{IR}} \sim 10^{12-13} L_\odot$, measured from far-IR SED fitting. Using the Kennicutt (1998) conversion factor on the measured IR luminosity of SMGs yield SFRs as large as $\sim 10^3 M_\odot \text{yr}^{-1}$, the largest measured at any epoch. Furthermore, the measured dust mass to stellar mass ratios of SMGs are $\sim 30\times$ larger than local spiral galaxies and are $\sim 6\times$ larger than local ULIRGs (Santini et al., 2010). Measurements of CO line luminosities converted into molecular hydrogen masses show that SMGs have massive gas reservoirs ($M_{\text{gas}} \sim 10^{10-11} M_\odot$) that are 20-50% of the dynamical mass (Greve et al., 2005; Tacconi et al., 2008; Ivison et al., 2011).

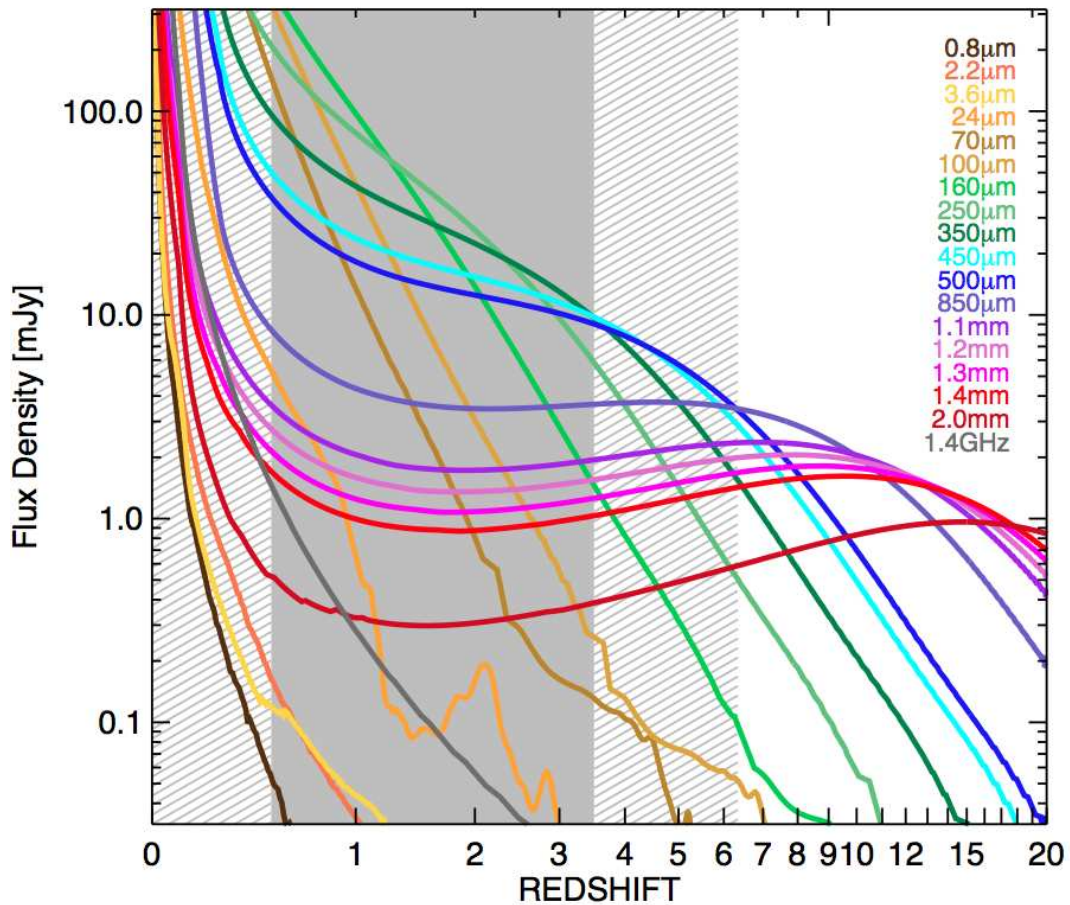


Figure 1.4: Negative K-Correction for LIRGs.

This figure has been reproduced from Casey et al. (2014) with the permissions from the authors and AAS. The predicted flux densities at different wavelengths as a function of redshift for a typical ultra-luminous infrared galaxy ($L_{\text{IR}} \geq 10^{12} L_{\odot}$) is approximately constant from $z \sim 0.5 - 8$ for sub-mm to mm wavelengths.

However, these gas reservoirs are quickly depleted (as hinted by their large SFRs), with depletion timescales on the order of 40 – 100 Myr (Greve et al., 2005). Clustering analyses reveal that SMGs reside in the largest dark matter halos ($M_{\text{halo}} \sim 10^{13} M_{\odot}$) in their epoch. The halo mass and the clustering length for SMGs are consistent with optically selected QSOs at $z \sim 2.5$. This finding supports evolutionary scenarios that link starbursts and QSOs, which are most likely triggered by the similar mechanisms (Hickox et al., 2012).

1.3.3 Observational Challenges

While SMGs contain important information on understanding how galaxies form and evolve, their intrinsic properties present observational challenges to the instruments currently available. At sub-millimeter and far-IR wavelengths, SMGs are readily detected but the instruments that performed previous deep wide-area surveys (e.g. Smail et al., 1997; Barger et al., 1998; Hughes et al., 1998; Weiß et al., 2009; Eales et al., 2010; Oliver et al., 2012) are characterized by large beam sizes ($\sim 15 - 40''$). Given that high redshift galaxies are typically compact in size ($0.1 - 0.3''$ Bouwens et al., 2004), a single source detected in the sub-mm can easily contain multiple sources in optical and near-IR observations. This makes identification of SMG counterparts from follow-up observations at higher resolutions difficult to identify.

Significant progress has been made in order to identify SMGs at non sub-mm wavelengths. Under the assumption that the observed local far-IR/radio correlation for star-forming galaxies also applies at high-redshift, deep high-resolution single-dish radio imaging can be used to constrain SMG positions within $\sim 1''$ (Smail et al., 2000). While this method allowed detailed follow-up studies of 75 SMGs (Swinbank et al., 2004; Chapman et al., 2004, 2005), radio-selected SMGs are biased to redshifts $z \leq 3$, due to the strong dependence of the radio continuum to luminosity distance ($I \sim (1 + z)^{-4+\alpha}$, $\alpha = 0.8$, Condon, 1992). This led to the need to use high-resolution sub-mm interferometry to unambiguously identify

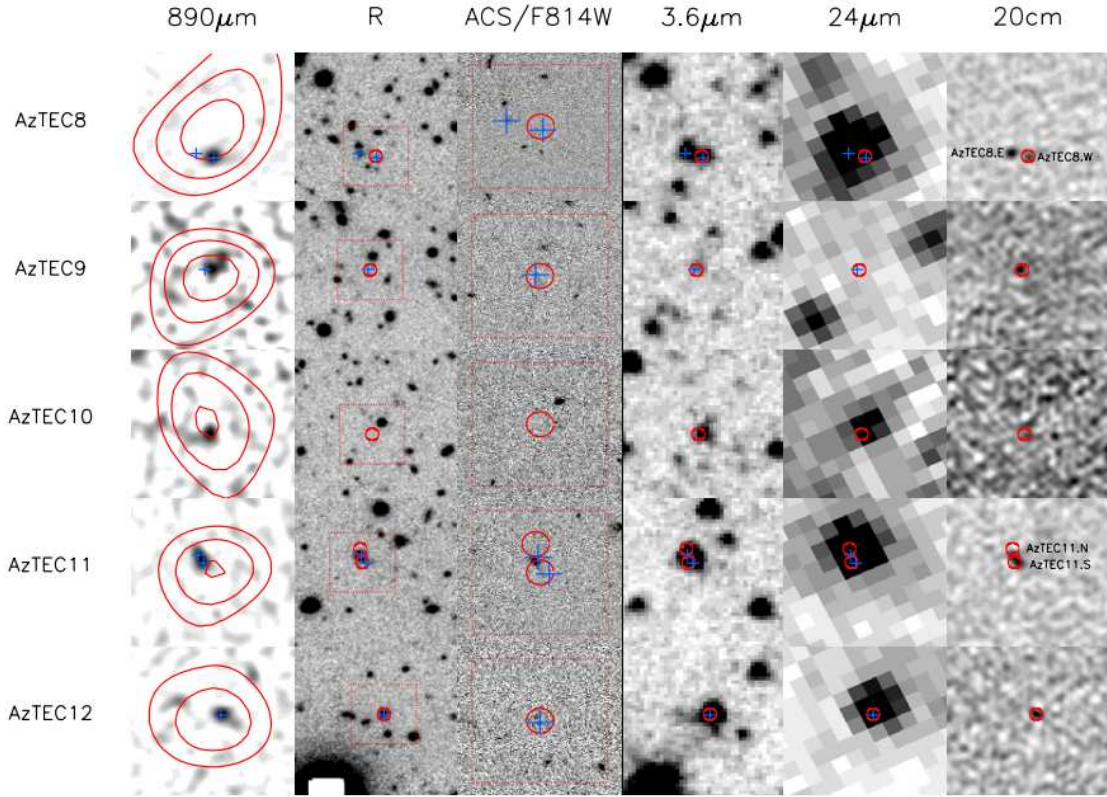


Figure 1.5: Multi-wavelength Image Stamps of SMGs.

This figure has been reproduced from Younger et al. (2009) with permission from the authors and AAS. The observed wavebands are labeled above the top row of the images. The red contours are from the AzTEC 1.1 mm map starting at 3σ with 1σ intervals. Blue crosses denote the measured radio centroids from 20 cm VLA observations. This demonstrates that multiple sources in the optical and near-infrared are covered within the area of a single detection due to the large beam sizes of wide-field sub-mm/mm instruments. High-resolution sub-mm interferometry provides the most unambiguous method of identifying SMG counterparts in shorter wavelengths.

SMG counterparts (Younger et al., 2007, 2009) that include both radio-detected and undetected populations. The use of sub-mm interferometry, shown in Fig. 1.5, is the most reliable method of identifying SMG counterparts but its smaller field of view is inefficient for larger samples. Therefore, more efficient but also less reliable statistical methods using wide-area deep near to mid-IR observations (Pope et al., 2006; Yun et al., 2008; Kim et al., 2012) from *Spitzer* (where SMGs are also expected to be detected) have also been implemented, in which the most recent study was able to identify $\geq 80\%$ of ~ 150 SPIRE-selected SMGs (Kim et al., 2012).

Although identifying SMGs at shorter wavelengths has definitely improved, they are intrinsically faint in near-IR observations, which traces the stellar emission. SMGs can have near-IR magnitudes of ≥ 20 (Swinbank et al., 2010; Targett et al., 2011; Aguirre et al., 2013; Targett et al., 2013), most likely due to the effects of dust extinction (Adelberger & Steidel, 2000). Therefore, the current near-IR studies of SMGs, which have been small in sample size (typically ≤ 25), could be biased in detecting only the sources that are brighter than a threshold surface brightness dictated by the instrument. Furthermore, previous near-IR size measurements of SMGs have an average angular size of $\sim 0.3''$ (Swinbank et al., 2010; Targett et al., 2011; Aguirre et al., 2013; Targett et al., 2013), comparable to the PSF FWHM of instruments that offer the highest spatial resolution. Near-IR observations that are diffraction-limited could explain why previous high-resolution studies of SMG morphologies have yielded mixed results, in which they have been found to be both irregular shaped galaxies (suggestive of major mergers) (Chapman et al., 2003) and axisymmetric disks (supports the smooth accretion model) (Targett et al., 2011, 2013). Alternatively, another possibility could also be that SMGs are galaxies simply born from different formation mechanisms (Narayanan et al., 2010; Davé et al., 2010).

In this thesis, we use gravitational lensing with our high-resolution near-IR imaging to investigate the stellar properties and morphologies of SMGs at an unprecedented detail. The boost in both apparent flux and spatial resolution can be exploited to provide near-IR observations of SMGs that are currently unachievable with the current generation of instruments. The sample of lensed SMGs is assembled from the brightest sources in *Herschel*-SPIRE 500 μm channel. This highlights one of the most useful, alternative applications of far-IR/sub-mm emission, which is selecting a gravitationally lensed galaxy population by applying a cut at large flux densities (Blain, 1996; Perrotta et al., 2002; Negrello et al., 2007; Paciga et al., 2009). We derive lens models for systems that display obvious lensing morphology to reconstruct the source plane and recover their intrinsic properties, such as their physical size and rest-frame optical luminosity.

1.4 The Discovery Of HFLS3: A Starbursting Galaxy At $z = 6.34$

One of the main goals of modern astronomy is to study the first galaxies that formed in the Universe. Compact, massive, quiescent galaxies have been observed as early as the peak of star-formation, at $z \sim 2$ (Damjanov et al., 2009), which implies that the bulk of their stellar mass must have been formed at a higher redshift. This is interesting from an evolutionary perspective, since the progenitors of the earliest massive galaxies could be among first galaxies that formed. Furthermore, how these massive structures achieved virialization at such an early time will probe and validate underlying assumptions that are used on galaxy formation models.

The discovery of HFLS3 (also known as 1HERMES S350 J170647.8+584623 Riechers et al., 2013) at $z = 6.34$ provides new insight on the current models of galaxy formation. At $z \geq 6$, the Universe was less than a billion years old, so based on previous studies of stellar mass build-up time-scales, mass function evolution, and the cosmic star-formation history we expect there to be few massive galaxies. If this is true, then this implies that there will also be fewer occurrences of gas-rich major mergers, which are commonly viewed as one of the mechanisms that can induce large star-formation rates. However, HFLS3 is a massive ($M_* \sim 10^{10} M_\odot$), star bursting ($SFR \geq 1000 M_\odot \text{ yr}^{-1}$), gas rich ($M_{\text{gas}}/M_{\text{dyn}} \sim 40\%$) galaxy, in contrast to the predictions of galaxy formation models. These unexpected properties of HFLS3 has therefore warranted detailed individual studies (Riechers et al., 2013; Cooray et al., 2014) and will continue to be a subject of future projects that focus on how the first galaxies were formed.

In this thesis, we present an updated study of HFLS3 which presents new high-resolution optical and near-IR (rest-frame UV) imaging using the *HST* Advanced Camera for Surveys (ACS) and Wide-Field Camera 3 (WFC3). The study of Riechers et al. (2013) found the

1mm continuum wave emission of HFLS3 to be $0.5''$ south of a $z = 2.09$ galaxy, which complicated the interpretation of its observed near-IR morphology due to possibility of having blended emission. Prior to the HST observations, the observed near-IR emission showed two components in which the southern component was assumed to be associated with HFLS3, which was closest to the 1.1 mm emission. If this southern component was indeed HFLS3, it would be invisible in wavelengths shorter than the redshifted Lyman limit (912 \AA). In Chapter 4 we show that this assumption is most likely invalid, justified by the detection at high significance of the southern component in the ACS F625W imaging. This new information also introduces the possibility that HFLS3 could be gravitationally lensed by the $z = 2.09$ galaxy, in which the magnification factor could significantly alter the previously derived properties. For this reason, we derive a lens model for HFLS3 using the high-resolution *HST* imaging and the 1 mm continuum wave emission, shown in Section 4.4. Finally, using the magnification factor and the photometry that spans from the rest-frame UV to radio wavelengths, we fit the data to an SED model and update intrinsically physical quantities such as dust mass, stellar mass, and star-formation rates.

Chapter 2

The Far-Infrared Emission from Dust Obscured Galaxies

2.1 Background

The bolometric luminosities of Luminous Infrared Galaxies (LIRGs; $L_{\text{IR}} \geq 10^{11}L_{\odot}$) and Ultra-LIRGs (ULIRGs; $L_{\text{IR}} \geq 10^{12}L_{\odot}$) are dominated by reprocessed thermal dust emission, due to prodigious rates of star-formation activity, black hole accretion, or both. Locally, these sources are rare, although out to $z \sim 1$ they become more numerous and increasingly dominate the infrared luminosity function of galaxies with increasing redshift (Le Flocc'h et al., 2005; Pérez-González et al., 2005; Caputi et al., 2007; Magnelli et al., 2009; Rodighiero et al., 2010; Eales et al., 2010). (U)LIRGs are thought to trace a phase of intense star-formation activity, which is likely followed by, or partially concurrent with, an episode of vigorous black hole accretion. Upon the cessation of these phases each produces an early-type galaxy (Genzel et al., 2001; Farrah et al., 2003; Lonsdale et al., 2006; Veilleux et al., 2009).

Studies using the Multiband Imaging Photometer for *Spitzer* (MIPS; Rieke et al. 2004) instrument onboard the *Spitzer Space Telescope* (Werner et al., 2004) have identified high-redshift ULIRGs from their $24\ \mu\text{m}$ emission (Yan et al., 2004; Houck et al., 2005; Weedman et al., 2006; Fiore et al., 2008; Dey et al., 2008; Farrah et al., 2008; Fiore et al., 2009). Dey et al. (2008) exploited this technique in the Boötes field of the NOAO Deep Wide Field Survey (NDWFS) and presented a sample of dusty ULIRGs selected by the color cut $R - [24] \geq 14$ (Vega magnitudes; $S_{24}/S_R \geq 1000$). This color selection samples the rest-frame $7.7\ \mu\text{m}$ polycyclic aromatic hydrocarbon (PAH) feature found in star-forming galaxies and causes the redshift distribution to have a biased average at $z \sim 2$. Also, at $z \sim 2$, the DOG selection falls within range of the power-law component of AGN emission in the mid-IR, which also identifies a population of active galactic nuclei (AGN). It is proposed that these dust-obscured galaxies (DOGs) are the latter stage of the sub-millimeter galaxy (SMGs; Hughes et al., 1998; Smail et al., 1997; Barger et al., 1998; Blain et al., 1999, among others) phase where an AGN is triggered while star formation is still occurring, causing some dust to be heated to higher temperatures (Dey et al., 2008) than in classic $850\ \mu\text{m}$ selected SMGs. Pope et al. (2008b) found that 30% of the SMGs are also DOGs, and of those SMG-DOGs, 30% are AGN-dominated ($\geq 50\%$ AGN contribution in mid-IR), consistent with this scenario. Using high resolution optical and near-IR (NIR) imaging from the *Hubble Space Telescope* to investigate DOG morphology, the studies of Bussmann et al. (2009a) and Bussmann et al. (2011) found that the morphologies of bump (star-forming) DOGs, power-law (AGN dominated) DOGs, SMGs, and high redshift quiescent distant red galaxies (DRGs) are consistent with the picture that major merger-driven systems eventually all evolve into compact relaxed passive galaxies (Springel et al. 2005 and references therein). Furthermore, Narayanan et al. (2010) used N-body and hydrodynamic simulations to model the temporal evolution of high redshift galaxies and found that at the peak of the merger-driven galaxies' star formation rate, a galaxy can both be identified as an SMG and a DOG. The same study also found that during the stages after final coalescence, merger-driven DOGs transition from being

star-formation dominated to being AGN dominated.

The launch of the *Herschel Space Observatory*¹ (Pilbratt et al., 2010) enables the direct observation of DOGs in the far-IR regime, instead of extrapolating from spectral energy distribution (SED) templates or stacking (e.g. Dey et al. 2008; Pope et al. 2008b). Melbourne et al. (2012) studied *Herschel*-detected DOGs with spectroscopic redshifts and showed that DOGs classified by their mid-IR SEDs as either bump (star-forming) or power-law (AGN-dominated) have $250\ \mu\text{m}/24\ \mu\text{m}$ flux-density ratios that are consistent with local ULIRGs of the respective classes. Penner et al. (2012) used *Herschel* data to show that DOGs' high rest-frame MIR/UV flux density ratios are due to varying amounts of UV dust obscuration, and speculated that it is caused by differing degrees of alignment between dust and stars, or simply by the differences in total dust content.

The focus of this chapter is to extend the study of DOGs in the far-IR to a complete sample in order to extract statistical conclusions about this galaxy population. We generate our DOG catalog using Subaru r^+ band and MIPS $24\ \mu\text{m}$ data from the Cosmological Evolution Survey (COSMOS; Scoville et al. 2007) and combine it with multi-wavelength data in the far-IR from the *Herschel* Multi-tiered Extragalactic Survey² (HerMES; Oliver et al. 2012). We calculate IR luminosities, star formation rate (SFR) and dust temperatures for all DOGs detected at $250\ \mu\text{m}$ and employ a stacking analysis to calculate the average properties of the undetected population and thus to probe fainter luminosities. For DOGs at $z = 1.5 - 2.5$, we generate a luminosity function and calculate the star-formation rate density at $z \sim 2$.

This chapter is organized as follows. Section 2.2 describes the dataset and sample selection.

¹*Herschel* is an ESA space observatory with science instruments provided by European-led Principal Investigator consortia and with important participation from NASA.

²<http://hermes.sussex.ac.uk/>

The results and our analysis are presented in Section 2.3. Unless specifically stated, all magnitudes are reported in the AB system, where $-2.5\log_{10}S_\nu(\mu\text{Jy}) + 23.9 = \text{AB mag}$, and assume a standard ΛCDM cosmology with $H_0 = 70 \text{ km s}^{-1}\text{Mpc}^{-1}$, $\Omega_{\text{M}} = 0.3$, and $\Omega_{\Lambda} = 0.7$.

2.2 Data and Sample Selection

2.2.1 Far-Infrared Data

The 250, 350, and 500 μm far-IR data were obtained using the *Herschel*-Spectral and Photometric Imaging Receiver (SPIRE; Griffin et al. 2010; Swinyard et al. 2010) as part of HerMES, with an area coverage that completely overlaps with the MIPS observations of the 2 deg² COSMOS field. We use the first data release (DR1) of HerMES maps that were processed using the `smap` pipeline (Levenson et al., 2010). The reduced maps reach 3σ point source depths of 8, 10, and 14 mJy, in the 250, 350, and 500 μm channels respectively, where σ is the combined instrumental and confusion noise. For sources with $S_{250} \geq 3\sigma$, we use the listed photometry from the HerMES cross-identification catalog (XID). This catalog uses known positions of 24 μm sources as a prior, and estimates SPIRE fluxes via linear inversion methods. Model selections are used to account for, and prevent overfitting, and to optimize the 24 μm input. The fitting method is outlined in more detail in Roseboom et al. (2010).

2.2.2 Optical and Mid-Infrared Data

We use deep Subaru Suprime-Cam (Komiya et al., 2003) aperture-corrected r^+ photometry supplied by the COSMOS catalog (Capak et al., 2007). The 5σ point-source depth for a $3''$ aperture is 26.8 mag.

The mid-IR data are from *Spitzer* observations carried out by the COSMOS *Spitzer* Survey

(S-COSMOS; Sanders et al. 2007) using the Infrared Array Camera (IRAC; Fazio et al., 2004) and MIPS. The IRAC 5σ depths at 3.6, 4.5, 5.6, and 8.0 μm for an aperture-corrected 1.9'' aperture, are 0.50, 0.6, 3, and 5 μJy , respectively. The MIPS 24.0 μm 5σ point source depth is 55 μJy .

We next generate a MIPS 24 μm -selected catalog that combines the Subaru and *Spitzer* datasets, using a two-step cross-matching process within the 2 deg^2 of the Subaru deep area in order to find optical counterparts for each source (Fu et al., 2010). Firstly, the 24 μm coordinates are matched to the closest IRAC detection within a 2'' search radius, then the nearest optical counterpart is identified within 1'' of the IRAC position. Finally, sources near bright stars that were within the Subaru/optical and *Spitzer*/IRAC 3.6 μm coverage were removed from the catalog to avoid contamination. The final catalog has 48,474 sources and is $\geq 90\%$ complete above $S_{24} = 80 \mu\text{Jy}$.

2.2.3 Sample Selection

DOGs are selected in the standard manner, by identifying sources with $r^+ - [24] \geq 7.5$ (AB mag; $S_{24}/S_{r^+} \geq 1000$) and we require $[24] \leq 18.90$ mag ($S_{24} \geq 100 \mu\text{Jy}$) due to the depth of the 24 μm data. Using these criteria 3077 of the 48474 (6%) COSMOS 24 μm sources are identified as DOGs (Fig. 2.1). The mid-IR SED of each DOG is examined using IRAC photometry ($\geq 5\sigma$) to classify whether a DOG contains a bump-like feature or resembles a power-law. For this study, a ‘‘bump’’ DOG is defined if it satisfies one of the following: $S_{3.6} \leq S_{4.5} \geq S_{8.0}$; $S_{4.5} \leq S_{5.8} \geq S_{8.0}$; or $S_{3.6} \leq S_{4.5} \geq S_{5.8}$. Here $S_{[3.6,4.5,5.8,8.0]}$ represent the flux densities in the 4 IRAC channels. Conversely, we label a DOG as ‘‘power-law’’ if it satisfies $S_{3.6} \leq S_{4.5} \leq S_{5.8} \leq S_{8.0}$. Previous studies have interpreted sources that feature a bump in the mid-IR SED to be the stellar continuum peak at rest-frame 1.6 μm , tracing stellar emission and likely star-formation dominated (e.g. Yan et al., 2005; Sajina et al.,

2007), while a power-law is dominated by AGN continuum emission (e.g. Weedman et al., 2006; Donley et al., 2007). Bump DOGs compose 47% of our sample, while power-law DOGs are rarer, totaling 10%. The remaining 43% are not classified due to one of two possibilities: insufficient or low signal to noise IRAC data; or an SED shape that does not satisfy the above criteria. For the latter case, most of the sources are at $z < 2$ (median of $z = 1.1$), such that the rest-frame $1.6 \mu\text{m}$ stellar continuum peak lies outside the wavelength range of the IRAC channels.

2.2.4 Redshifts

All redshifts used in this paper are from COSMOS. Spectroscopic redshifts are used when available (35 sources, 1%; Lilly et al. 2007, Kartaltepe et al., in prep), although virtually all of our DOG sample (2979 sources, 97%) use photometric redshifts. The photometric redshifts are derived from 30 photometric bands (Ilbert et al., 2009), providing $\sigma_{\Delta z/(1+z)} = 0.02$, for $24 \mu\text{m}$ sources that lie at $z = 1.5 - 3$ and have the same r^+ mag range as DOGs. The 61 DOGs that are X-ray detected use photometric redshifts that also account for AGN flux variability (Salvato et al., 2009). Also, two sources do not have a redshift estimate and are excluded from our sample. We note that the sharp peak in the redshift distribution at $z = 1.95$ is due to rounding from the redshift values associated with the bin size used and no spatial correlation is observed. The redshift distribution of the final sample of 3075 DOGs is shown in Fig. 2.2, with a mean of $\langle z \rangle = 1.9 \pm 0.3$. The sample of 90 DOGs in the Boötes field with spectroscopic redshifts from Bussmann et al. (2012), normalized to have an equal peak with our sample, is also shown. The two samples have a consistent mean z of 1.9 ± 0.02 and 2.1 ± 0.5 , for our sample and the Bussmann et al. (2012) sample, respectively.

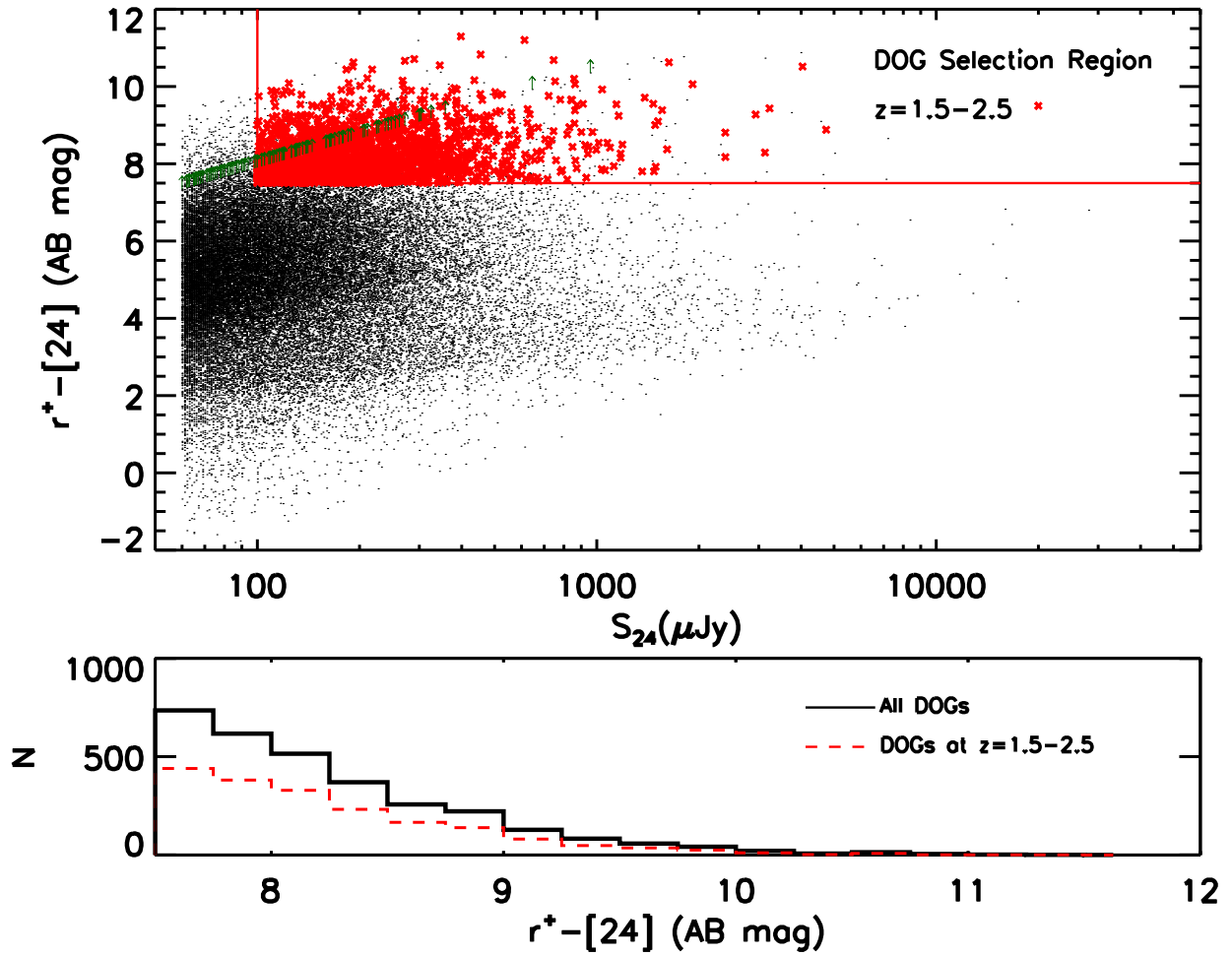


Figure 2.1: $r^+ - [24]$ as a function of $24 \mu\text{m}$ flux. DOGs are selected to have $r^+ - [24] \geq 7.5$ AB mag and $S_{24} \geq 100 \mu\text{Jy}$. DOGs with $z = 1.5 - 2.5$ are highlighted in red, while green arrows are lower limits for sources that were undetected in the r^+ -band. The 1901 DOGs at $z = 1.5 - 2.5$ are not biased in $r^+ - [24]$ when compared to other DOGs.

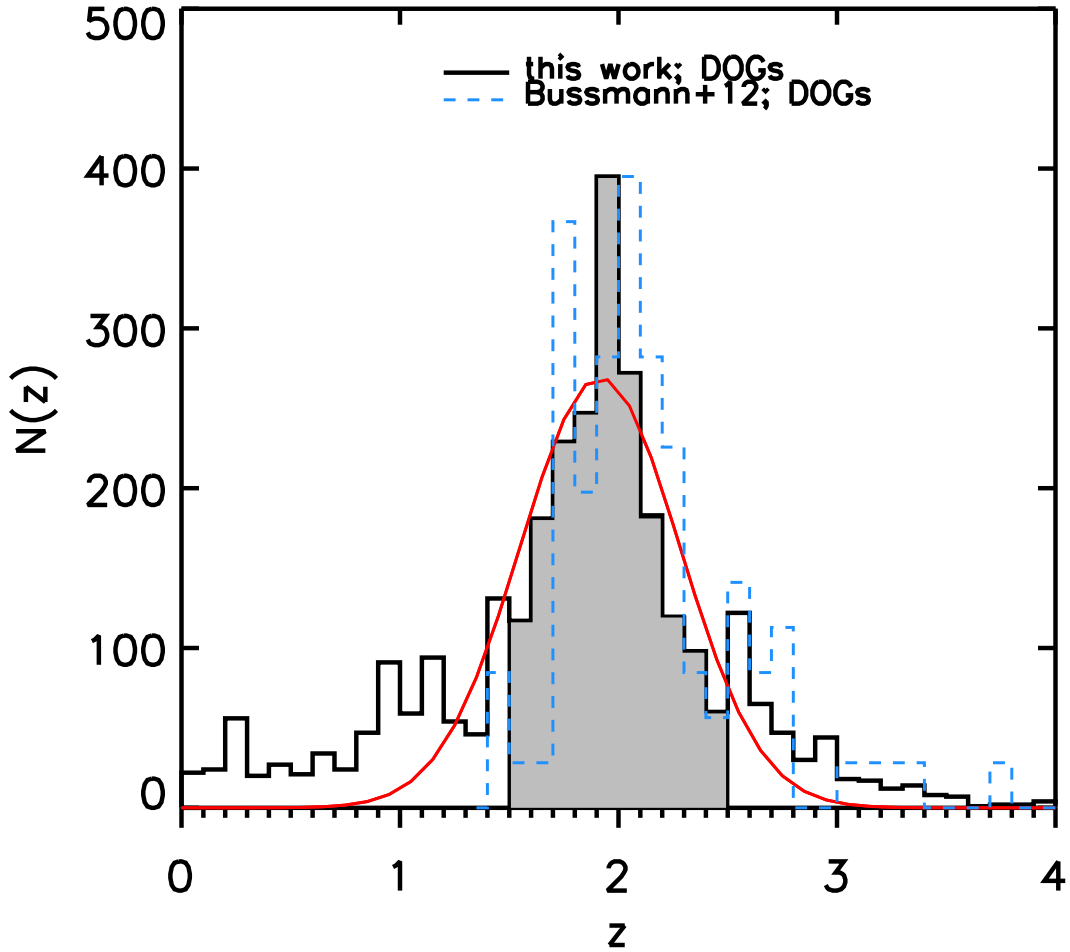


Figure 2.2: Photometric redshift distribution of DOGs in the COSMOS field.

We show the DOG distribution from Bussmann et al. (2012) normalized to have equal peaks for comparison. The filled region highlights the range $z = 1.5 - 2.5$, considered for our analysis. We find $\langle z \rangle = 1.9 \pm 0.3$, assuming a Gaussian distribution, as shown in red.

2.3 Analyses and Results

2.3.1 Far-Infrared Spectral Energy Distributions

Using the COSMOS redshifts and *Herschel* 250, 350 and 500 μm photometry, we fit the far-IR SED and calculate the rest-frame IR luminosity (8 – 1000 μm) and characteristic dust temperature. We divide the DOGs into two subsamples based on 250 μm detections: a DOG is considered *Herschel*-detected if it satisfies $S_{250} \geq 3\sigma_{250}$ (where σ_{250} is the total uncertainty due to the instrumental and confusion noise), and undetected otherwise. Of our DOG sample, 51% are thus *Herschel*-detected. To calculate the characteristic dust temperature, for each of these we use the available SPIRE flux densities to fit a modified blackbody of the form

$$S_\nu \propto B_\nu(T_{\text{dust}})\nu^\beta, \quad (2.1)$$

where ν is frequency, β is the dust emissivity, fixed to the typical value of 1.5 (Draine, 2003b), T_{dust} is the dust temperature and B_ν is the Planck function, defined as

$$B_\nu = \frac{2h\nu^3}{c^2} \frac{1}{e^{h\nu/k_{\text{B}}T_{\text{dust}}} - 1}. \quad (2.2)$$

Here h is Planck's constant, c is speed of light, and k_{B} is Boltzmann's constant. The temperature we calculate is insensitive to and consistent with the reported error bars from varying β slightly. All 250 μm -detected DOGs are also detected in one other band can be fitted with this function.

We derive estimates of the IR luminosity by fitting the available SPIRE data to the SED template library of Chary & Elbaz (2001) (hereafter CE01). The template with the minimum χ^2 is chosen for the best fit. The uncertainty in IR luminosity is derived by first producing 1000 mock catalogs for each source that assume a Gaussian distribution centered around the

listed SPIRE flux density, with a dispersion equal to the average SPIRE flux density error. The IR luminosity per source is recalculated 1000 times and the standard deviation of the IR luminosity distribution is the error in our calculation. Examples of the SED template and modified blackbody fitting are shown in Fig. 2.3.

The IR luminosity ($8 - 1000 \mu\text{m}$) is converted to star formation rate using (Kennicutt, 1998)

$$\text{SFR}(\text{M}_{\odot}\text{yr}^{-1}) = 1.72 \times 10^{-10} L_{\text{IR}}(L_{\odot}), \quad (2.3)$$

which assumes a Salpeter initial mass function (IMF). We note that in our study we assume that UV emission will provide negligible contribution to the total star-formation rate, as validated by Penner et al. (2012).

To measure the average flux density of the undetected DOGs, we bin the sources in redshift and for each bin stack on the SPIRE residual maps. These maps are generated by performing a blind extraction and PSF-subtraction to prevent contamination of individually detected sources. We use the publicly available IDL stacking library from Béthermin et al. (2010) to perform the stacking³. Each stacked image was converted from the native Jy beam^{-1} to Jy pixel^{-1} and aperture photometry with an aperture size equal to $22''$, $30''$, and $42''$ for 250, 350 and 500 μm respectively, is performed to calculate the flux of the stacked images. These aperture flux densities are consistent with those measured in the central pixel when the stacked map is in units of Jy beam^{-1} .

The observed stacked flux densities are corrected for the boosting from clustering bias by dividing by factors of 1.07, 1.10 and 1.20 at 250, 350 and 500 μm , respectively. The appropriate correction factors vary with clustering strength and are thus population dependent. These values were calculated by Béthermin et al. (2012) for 24 μm sources and are valid for DOGs because the observed correlation lengths, r_0 (a proxy for clustering amplitude), for DOGs

³The IDL library from Béthermin et al. (2010) is available at <http://www.ias.u-psud.fr/irgalaxies/downloads.php>

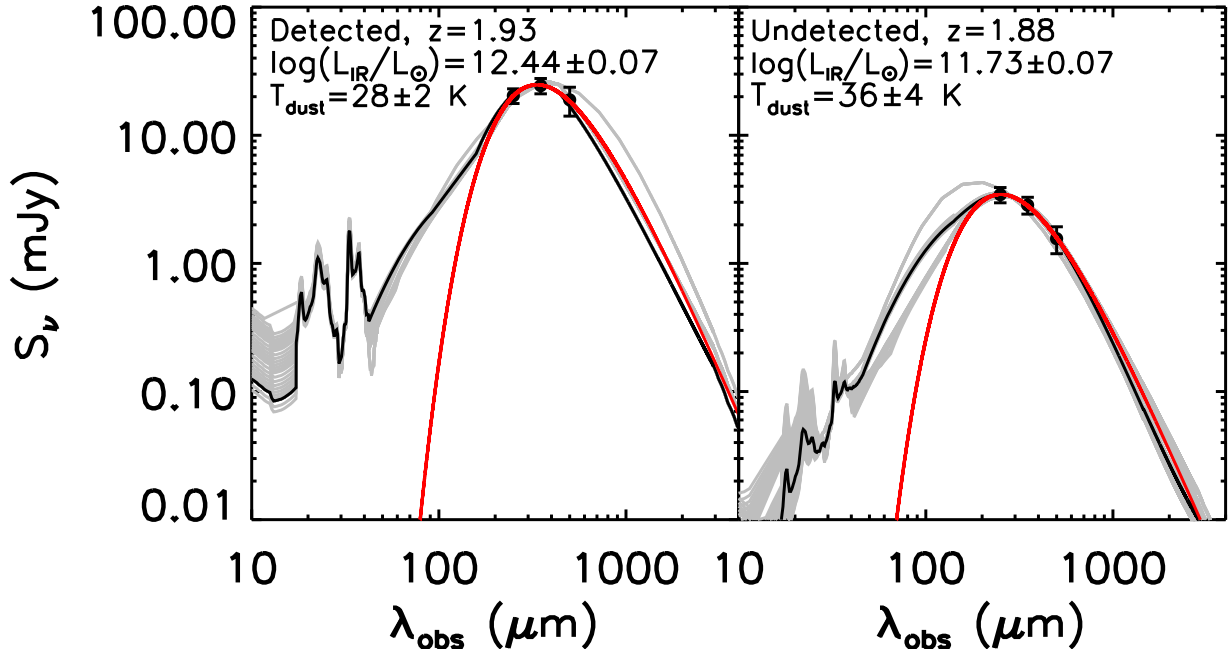


Figure 2.3: Sample FIR SED fits for DOGs.

The left and right panel shows a detected and an undetected DOG in *Herschel*, respectively. The black curve shows the best fitting template to the SPIRE data points (black circles) and the gray curves show CE01 templates that provide acceptable fits consistent with the error bars. The red curve shows the best fit modified blackbody, which we use to calculate the dust temperature.

(Brodwin et al., 2008) and the parent population of $24\mu\text{m}$ sources (Magliocchetti et al., 2008; Starikova et al., 2012) are consistent. Errors in the photometry are calculated from bootstrapping the sources to be stacked. For each redshift bin, the clustering-corrected SPIRE flux densities of undetected DOGs are set to equal the median stacked flux densities and the IR luminosity and dust temperature are calculated using the same method as for the *Herschel*-detected DOGs. The (clustering-corrected) stacked fluxes and errors, and the resulting average infrared luminosities and dust temperatures are shown in Table 2.1.

We note that the stacks of $250\mu\text{m}$ images are on average a factor of 2 deeper than our 3σ detection limit. In Fig. 2.4 we show an example of the median stacked images for 250, 350 and $500\mu\text{m}$ from left to right at $z = 1.75 - 2.00$ and an example SED using stacked SPIRE flux densities for an undetected DOG at $z = 1.88$ is shown in the right panel of Fig. 2.3. Each image stack is large enough to provide a good estimate for the background noise.

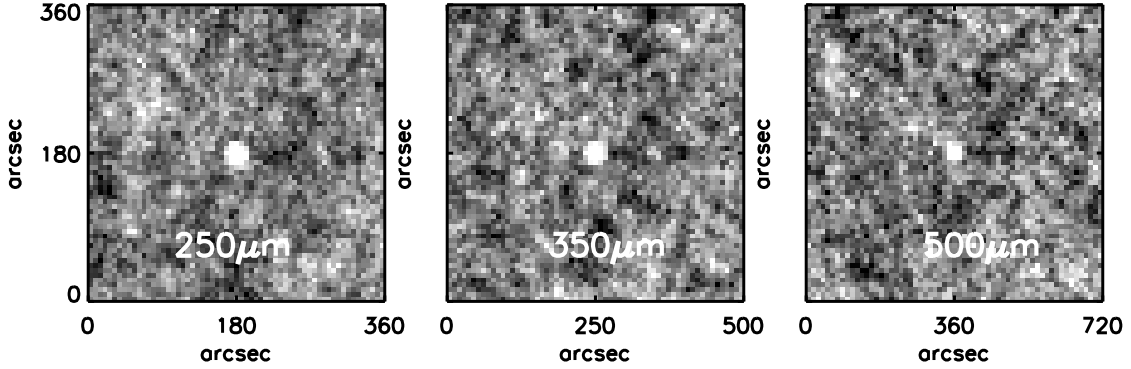


Figure 2.4: Sample FIR stacking results of DOGs observed by *Herschel*. From left to right, the panel shows the median stack for *Herschel*-undetected DOGs at 250, 350, and 500 μm in the redshift bin $z = 1.75$ to 2.00.

Table 2.1: SPIRE Stacking Results

z	S_{250}^a (mJy)	S_{350}^a (mJy)	S_{500}^a (mJy)	N^b	L_{IR}^c ($\times 10^{12} L_{\odot}$)	T_{dust}^c (K)
< 1.50	4.2 ± 0.5	3.0 ± 0.4	2.1 ± 0.4	354	0.16 ± 0.13	25.1 ± 5.5
$1.50 - 1.75$	3.5 ± 0.5	2.6 ± 0.5	1.7 ± 0.4	218	0.37 ± 0.02	34.6 ± 0.9
$1.75 - 2.00$	3.4 ± 0.5	2.9 ± 0.4	1.6 ± 0.4	406	0.52 ± 0.07	37.2 ± 0.9
$2.00 - 2.25$	4.3 ± 0.6	3.9 ± 0.6	1.7 ± 0.5	237	0.68 ± 0.06	40.0 ± 1.0
$2.25 - 2.50$	4.3 ± 1.1	3.7 ± 0.9	2.7 ± 0.7	82	1.00 ± 0.21	37.8 ± 0.8
> 2.5	4.9 ± 0.7	4.0 ± 0.6	2.9 ± 0.6	185	1.71 ± 2.8	44.3 ± 6.3

Fig. 2.5 shows IR luminosities of the *Herschel*-detected DOGs as a function of redshift. The average IR luminosity for detected and undetected DOGs is $(2.8 \pm 0.3) \times 10^{12} L_{\odot}$ and $(6.0 \pm 1.0) \times 10^{11} L_{\odot}$, respectively. LIRGs ($10^{11} \leq L_{\text{IR}} (L_{\odot}) \leq 10^{12}$) comprise 15% of *Herschel*-detected DOGs and 75% for *Herschel*-undetected DOGs. ULIRGs ($10^{12} \leq L_{\text{IR}} (L_{\odot}) \leq 10^{13}$) make up 78% of the *Herschel*-detected and 15% for *Herschel*-undetected DOGs. Hyperluminous infrared galaxies (HLIRGs ($\geq 10^{13} L_{\odot}$)) are the rarest, totaling 2% for *Herschel*-detected DOGs and none for *Herschel*-undetected DOGs. Although we note that there is additional uncertainty in the fractional contributions of the undetected sources, due to the use of stacked average fluxes, which minimizes the contribution from extreme sources. *Herschel*-detected power-law, or AGN-dominated DOGs, have on average $L_{\text{IR}} = (4.5 \pm$

$0.5) \times 10^{12} L_{\odot}$, making them more IR-luminous than *Herschel*-detected bump, star-forming DOGs, which have $L_{\text{IR}} = (3.1 \pm 0.4) \times 10^{12} L_{\odot}$, which is consistent with the findings of Melbourne et al. (2012). Selection effects are investigated by calculating the IR luminosity of a representative CE01 template, scaled such that $S_{24} = 100 \mu\text{Jy}$ or $S_{250} = 8 \text{ mJy}$, as shown in Fig. 2.5. The local maxima in IR luminosity at $z \sim 1.5$ in the $24 \mu\text{m}$ curve is due to the rest-frame $9.7 \mu\text{m}$ silicate absorption feature. The lack of DOGs below the $24 \mu\text{m}$ and $250 \mu\text{m}$ limit at a given redshift leads us to conclude that the apparent trend in Fig. 2.5 that IR luminosity is increasing with redshift is a selection effect.

Figure 2.6 shows dust temperatures as a function of IR luminosities for DOGs, color-coded by redshift. The average characteristic dust temperature is $T_{\text{dust}} = (34 \pm 7) \text{ K}$ and $(37 \pm 5) \text{ K}$ for *Herschel*-detected and undetected DOGs, respectively. *Herschel*-detected power-law DOGs and bump DOGs have average $T_{\text{dust}} = (37 \pm 6) \text{ K}$ and $(35 \pm 7) \text{ K}$, respectively, and is consistent with each other. We consider sample selection effects in the $T_{\text{dust}} - L_{\text{IR}}$ plane by calculating IR luminosities and dust temperatures of the CE01 templates with $S_{250} = 8 \text{ mJy}$ and $S_{24} = 100 \mu\text{Jy}$. The $250 \mu\text{m}$ flux limit causes two selection effects: the first biases against hot sources, and the second is a lower luminosity limit that is redshift dependent (Fig. 2.6). This second effect causes an apparent trend that the warmest and IR luminous sources lie at high redshifts. The $24 \mu\text{m}$ flux limit produces a similar effect. We observe that the dearth of sources at high luminosities and low dust temperatures is not caused by selection bias and is a real effect. This is consistent with Symeonidis et al. (2013), who found that cold cirrus-dominated SEDs (Rowan-Robinson et al., 2010) are rare in the most IR luminous galaxies.

The results shown in Fig. 2.6 suggest that DOGs span a wider range of dust temperatures than $z \sim 2$ galaxy populations selected at longer wavelengths. While this may be true, it is more likely due to the different selection effects associated with each galaxy population. For example, SMGs (by which we mean $850 \mu\text{m}$ or 1 mm selected sources) are biased towards

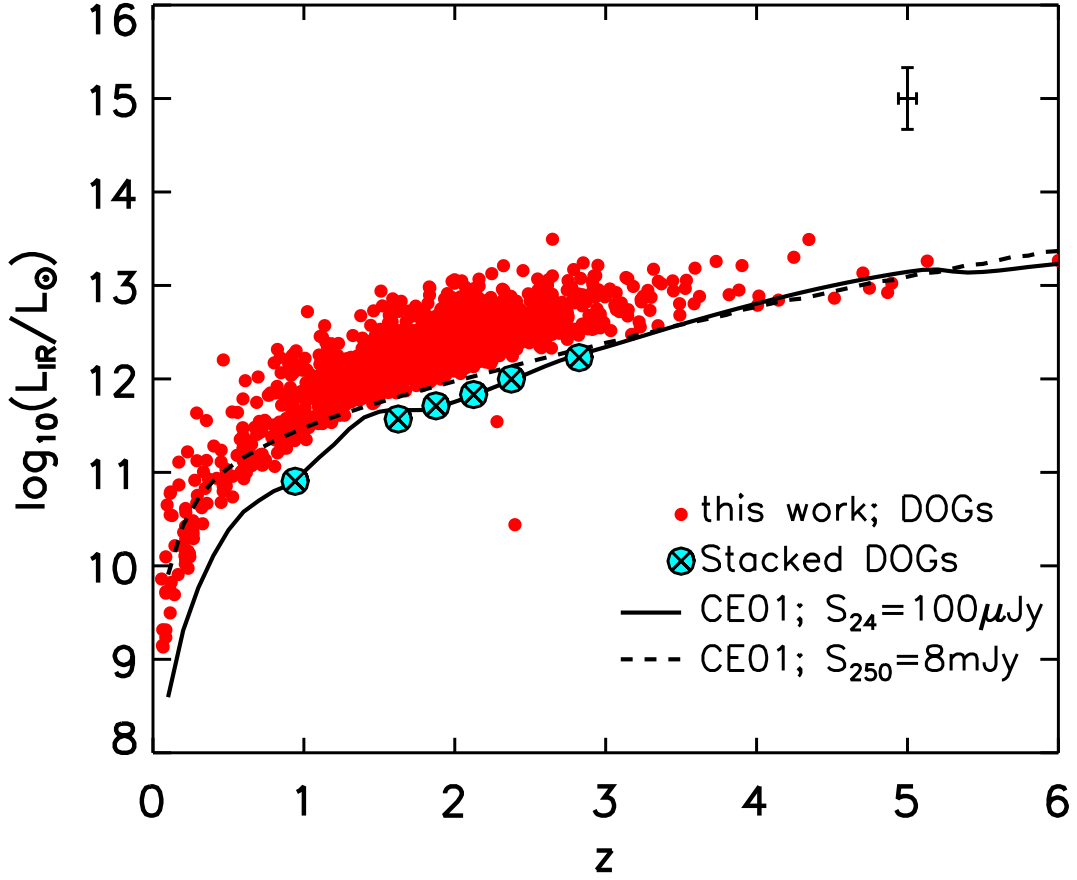


Figure 2.5: IR luminosity as a function of redshift for DOGs. *Herschel*-detected DOGs are shown as red circles and the median IR luminosity for stacked DOGs at each redshift bin are shown as cyan circles with x's. A representative template from Chary & Elbaz (2001) scaled to the DOG 24 μm (solid curve) and 250 μm detection limit (dashed curve) are also shown. A typical error bar is shown at the top right. The apparent trend that IR luminosity increases with redshift is a selection effect.

Table 2.2: Average DOG IR Luminosities and Dust Temperatures

Type	L_{IR} ($\times 10^{12} L_{\odot}$)	T_{dust} (K)
Detected ^{α}	2.8 ± 0.3	33 ± 7
Undetected ^{α}	0.6 ± 0.1	37 ± 5
Bump [*]	4.5 ± 0.4	34 ± 7
Power-law [*]	3.1 ± 0.4	37 ± 6

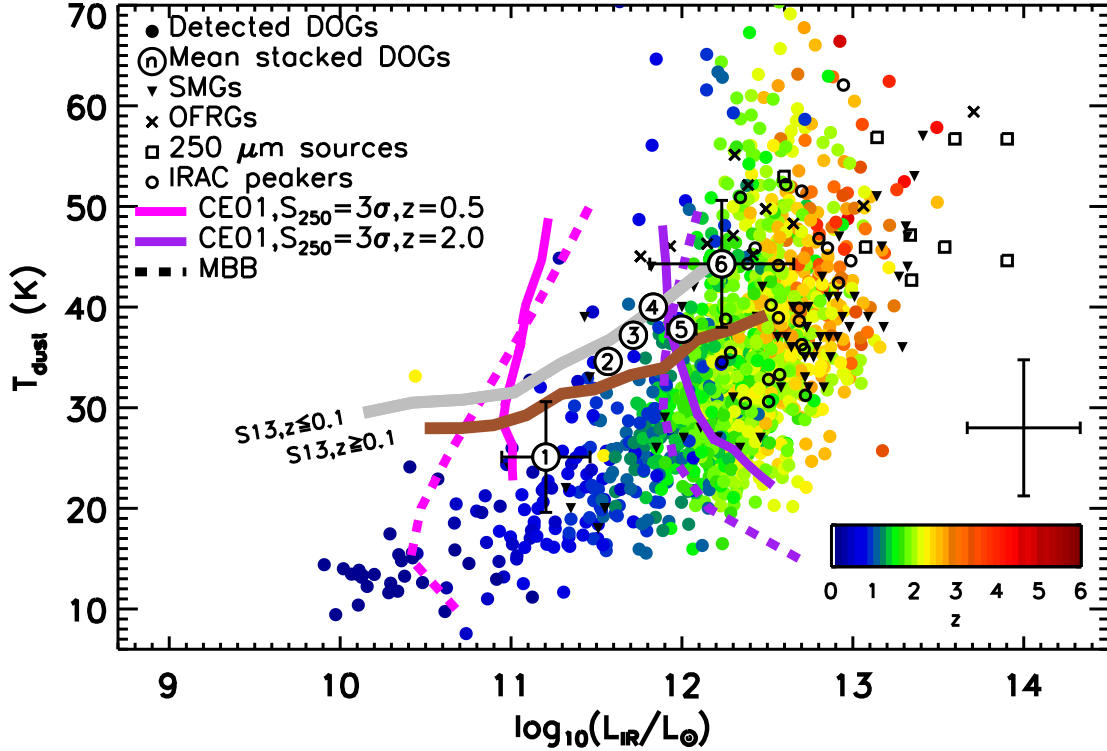


Figure 2.6: Dust temperatures and IR luminosities for DOGs.

For comparison, we also show other $z \sim 2$ galaxy populations (SMGs: Magnelli et al. 2012, OFRGs: Casey et al. 2009; Magnelli et al. 2010, $250 \mu\text{m}$ sources: Casey et al. 2011, IRAC peakers: Magdis et al. 2010). We show *Herschel*-detected DOGs, colored by redshift. The average IR luminosity and dust temperature of *Herschel*-undetected DOGs at $z = 2$ is represented by the solid cyan circle. The black curves represent the selection effects from estimating the dust temperature and IR luminosity by considering templates from Chary & Elbaz (2001) at $z = 1.5, 2.0,$ and 2.5 , with $S_{250} = 8 \text{ mJy}$, our 3σ detection limit. The red curve is for $S_{24} = 100 \mu\text{Jy}$ at $z = 1.5$. We conclude that the apparent trend that hotter sources are at higher redshifts may be a selection effect and that the absence of sources with high luminosities and colder temperatures is not a selection effect.

detecting cold-dust dominated sources because hot sources are missed by sub-mm surveys (Casey et al., 2009; Chapin et al., 2009). Optically-faint radio galaxies (OFRGs; Casey et al. 2009; Magnelli et al. 2010), which share similar stellar masses, radio luminosities, and UV spectra as SMGs demonstrate this, while we also note that the radio-detection limit is biased against the coldest sources (e.g. Wardlow et al. 2011). DOGs are more insensitive to these selection biases and thus show a wider range of temperatures. Magdis et al. (2010) found similar results when investigating the characteristic dust temperatures for IRAC peakers at $z \sim 2$ and showed that mid-IR selected sources bridge the gap in temperature ranges between OFRGs and SMGs. We note that the $250 \mu\text{m}$ selected sources suffer from the same selection biases as our *Herschel*-detected DOGs but shifted to higher luminosities due to their shallower $250 \mu\text{m}$ detection limit.

2.3.2 Infrared Luminosity Function at $z \sim 2$

We compute the IR luminosity function of DOGs using the $1/V_{\text{max}}$ method (Schmidt, 1978), defined as:

$$\Phi(L)\Delta L = \sum_i \frac{1}{V_{\text{max},i}}, \quad (2.4)$$

where V_{max} is the maximum comoving volume of the i th source such that it would be detected and included in the sample. We consider the peak of the redshift distribution using only DOGs at $z = 1.5 - 2.5$. For the *Herschel*-detected DOGs we use two flux limits to determine V_{max} : $S_{24} = 100 \mu\text{Jy}$; and $S_{250} = 8 \text{ mJy}$. These are the two detection limits of the survey. For the *Herschel*-undetected sample, the $24 \mu\text{m}$ flux limit alone was used to calculate V_{max} . The uncertainties are from Poisson statistics and binning errors, where the binning errors are calculated by generating the IR luminosity function 1000 times from IR luminosities calculated from artificial SPIRE flux densities described in Section 2.3.1 and taking the

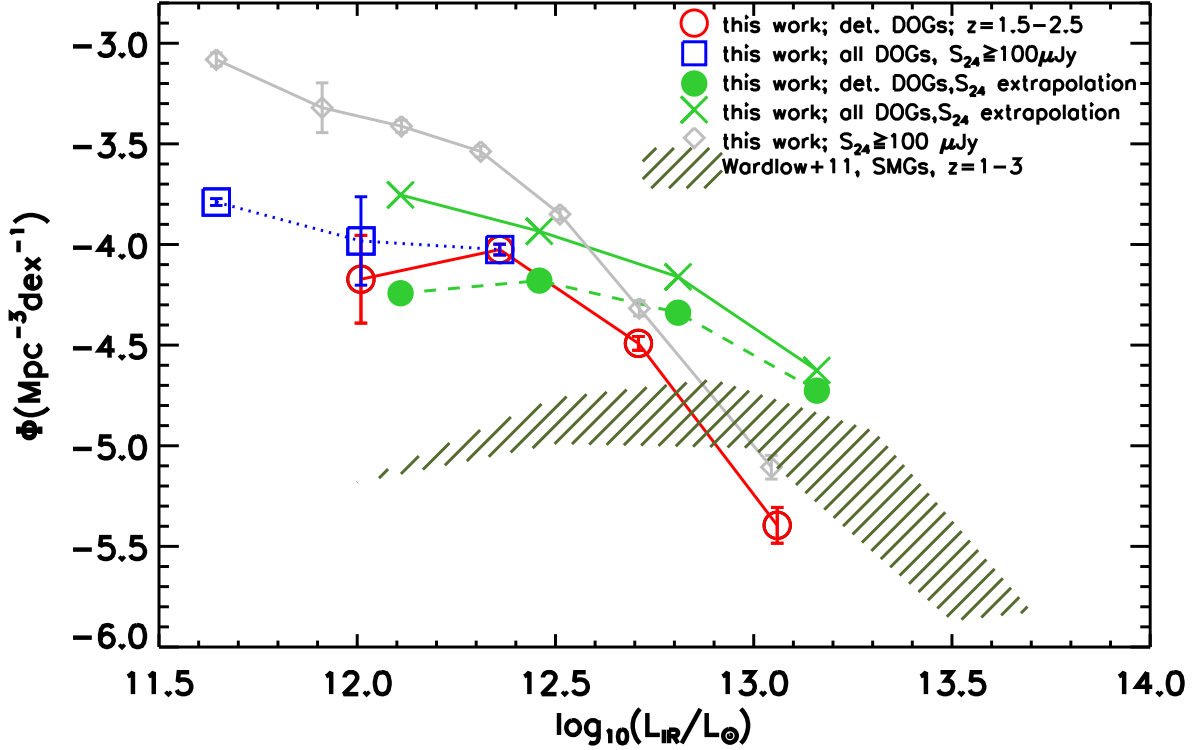


Figure 2.7: IR luminosity function of DOGs at $z \sim 2$.

Individually *Herschel*-detected DOGs and the results from stacking undetected DOGs are shown. We compare this to an IR luminosity function for *Herschel*-detected DOGs and all DOGs generated from $24\ \mu\text{m}$ extrapolation using templates from Chary & Elbaz (2001), classical SMGs (Wardlow et al., 2011), and $24\ \mu\text{m}$ selected galaxies with $S_{24} \geq 100\ \mu\text{Jy}$. The results of stacking allow us to estimate the faint end of the LF and we note that using $24\ \mu\text{m}$ flux density to calculate IR luminosity results in overestimation. DOGs have a higher normalization, Φ^* , but a lower luminosity turnover, L^* , than SMGs.

standard deviation per IR luminosity bin. The DOG IR luminosity function at $z \sim 2$ is presented in Fig. 2.7 and Table 2.3. The faint end of the IR luminosity function for *Herschel*-undetected and detected DOGs are coadded, which affects the lowest luminosity bin for *Herschel*-detected DOGs the most, showing a 0.20 dex increase.

For comparison, the DOG IR luminosity function for *Herschel*-detected DOGs and all DOGs, calculated by extrapolating the infrared luminosity from S_{24} using CE01 templates, is also shown in Fig. 2.7. The contribution to the number density of *Herschel*-detected DOGs relative to the whole DOG population is never 100% at each IR luminosity bin, which means that some IR luminosities of the undetected population are severely being overestimated. We find that the IR luminosities using this method are overestimated by a median factor of 1.8. This is consistent with the previous studies of $24\ \mu\text{m}$ -selected galaxies at $z \sim 2$ (Houck et al., 2005; Yan et al., 2007; Daddi et al., 2007; Papovich et al., 2007; Pope et al., 2008b; Elbaz et al., 2011) and stresses the importance of far-IR observations, further highlighting that the use of $24\ \mu\text{m}$ flux density to estimate IR luminosity is problematic at $z > 1$, due to features from PAH emission, silicate absorption, and a power-law component from AGN.

We compare the number densities of DOGs to the parent population of sources with $S_{24} \geq 100\ \mu\text{Jy}$ (Fig. 2.7). The luminosity function of $24\ \mu\text{m}$ sources is calculated self-consistently using SPIRE data. There are 5932 sources in COSMOS with $S_{24} \geq 100\ \mu\text{Jy}$ at $z = 1.5 - 2.5$, of which 32% are DOGs. Fig. 2.7 shows that DOGs have a smaller overall normalization in their luminosity function (since they are fewer in number) and their relative contribution to the $24\ \mu\text{m}$ number density is roughly constant with increasing luminosity. Our results agree with the findings of Penner et al. (2012), where it was found that the distribution of IR luminosities for DOGs and the parent population of $24\ \mu\text{m}$ sources are statistically indistinguishable.

Figure 2.7 also shows the $z = 1 - 3$ SMG luminosity function from Wardlow et al. (2011) from

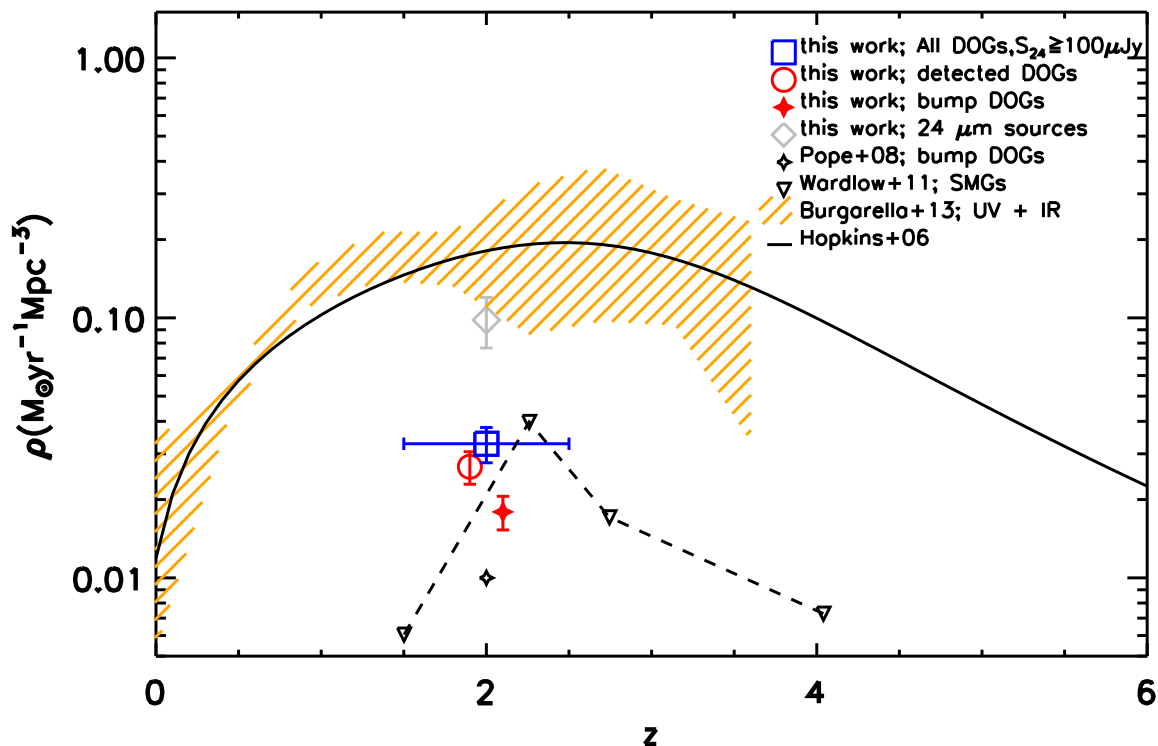


Figure 2.8: Star formation rate density (ρ_{SFR}) of all DOGs.

Herschel-detected DOGs are offset by $z = -0.1$ and bump DOGs are offset by $z = +0.1$, for clarity. The ρ_{SFR} of the parent population, $S_{24} \geq 100 \mu\text{Jy}$ sources at $z = 1.5 - 2.5$, is shown for comparison. We also show ρ_{SFR} for bump DOGs ($S_{24} \geq 100 \mu\text{Jy}$) at $z = 2$ in the GOODS field from Pope et al. (2008b) and SMGs from Wardlow et al. (2011) The evolution of ρ_{SFR} as a function of redshift from Hopkins & Beacom (2006) and Burgarella et al. (2013) are also shown. Based on these models, DOGs contribute 12 – 29% to the total ρ_{SFR} of the Universe at $z \sim 2$.

Table 2.3: The IR Luminosity Function for DOGs at $z = 1.5 - 2.5$

$\log_{10}(L_{\text{IR}}/L_{\odot})$	Φ ($\text{Mpc}^{-3}\text{dex}^{-1}$)	N^a
11.40 – 11.80	$(-3.79 \pm 0.02)^b$	$(660)^b$
11.80 – 12.15	-4.17 ± 0.21 (-3.98 ± 0.22) ^b	150 (433) ^b
12.15 – 12.50	-4.03 ± 0.03 (-4.02 ± 0.09) ^b	522 (522) ^b
12.50 – 12.85	-4.49 ± 0.03	252
12.85 – 13.20	-5.40 ± 0.09	31

two redshift bins. DOGs are more common than SMGs at $z \sim 2$, which is reflected in the higher normalization in the luminosity function, although in the HLIRG regime, SMGs dominate. This is consistent with the picture that in order for DOGs to represent an evolutionary stage after the peak of star-formation rate in the SMG phase (Narayanan et al., 2010), they must have lower IR luminosities and star-formation rates. As is shown in fig. 2.8, the total star-formation rate density (ρ_{SFR}) provided by the two populations are approximately even despite the number and intensity of sources.

To calculate the contribution of DOGs to the ρ_{SFR} of the Universe at $z \sim 2$, we integrate the IR luminosity function and use equation 2.3. Figure 2.8 shows DOGs compared to other $z \sim 2$ galaxy populations. The total uncertainty in ρ_{SFR} is calculated from the quadrature sum of individual star-formation rate uncertainties and the standard deviation of ρ_{SFR} from the mock catalogs discussed in Section 2.3.1. Horizontal error bars represent the considered redshift interval. The value of ρ_{SFR} for DOGs at $z = 1.5-2.5$ is $(3.2 \pm 0.5) \times 10^{-2} \text{ M}_{\odot}\text{yr}^{-1}\text{Mpc}^{-3}$ which contributes to 12–29% of the overall ρ_{SFR} at $z = 2$ based on the models of Hopkins & Beacom (2006) and Burgarella et al. (2013). While 32% of the $24 \mu\text{m}$ population at $z = 1.5 - 2.5$ are DOGs, their fractional contribution to the star-formation rate density is slightly larger because of their typically higher IR luminosities. When comparing against all $z = 1.5 - 2.5$ sources with $S_{24} \geq 100 \mu\text{Jy}$, DOGs contribute 37% to the $24 \mu\text{m}$ ρ_{SFR} . This is consistent with the relative distribution of DOGs’ infrared luminosities compared against the $24 \mu\text{m}$ population observed in the IR luminosity function.

The undetected and power-law sources provide non-dominant contributions to the total ρ_{SFR} of DOGs. The *Herschel*-undetected DOGs contribute 18% and power-law DOGs contribute just 9%. We note that even though power-law DOGs are thought to be dominated by AGN emission in the IRAC bands, their far-IR emission is still likely dominated by star-formation (Elbaz et al., 2010). Indeed, even studies of the most active AGN have revealed that SED fits for *Herschel*-detected AGNs always required a starburst component in order to appear bright in the far-IR (Hatziminaoglou et al., 2010). As an attempt to quantify this claim, we use a simplified method to calculate an upper limit on the AGN contribution to the IR luminosity and star-formation rate in power-law DOGs and hence the contamination of ρ_{SFR} by AGN. We begin by scaling the AGN SEDs from Kirkpatrick et al. (2012) to the $24\ \mu\text{m}$ flux density of each power-law DOG and calculate the luminosity from the warm dust component. Then, by assuming that the warm dust component is entirely AGN-dominated and the cold dust component is entirely star-formation dominated, we can subtract the warm IR luminosity from the CE01 IR luminosity to calculate the residual contribution from star-formation. We find that power-law DOGs each have a maximum average contribution of 70% to the IR luminosity, which could contaminate ρ_{SFR} by $\sim 0.2 \times 10^{-2}\ \text{M}_{\odot}\text{yr}^{-1}\text{Mpc}^{-3}$, which is only 6% of the total DOG ρ_{SFR} . In addition, we also estimate the dispersion of AGN contribution by normalizing quasar SED templates from Elvis et al. (1994), Richards et al. (2006), Polletta et al. (2007) and Dai et al. (2012) to the average power-law DOG $24\ \mu\text{m}$ flux density at $z = 1.5 - 2.5$ and assume that the SEDs have no emission associated with star-formation. Under this assumption, the average AGN contributions to the individual galaxies' IR luminosities range from 5% to 65%, depending on the SED, which corresponds to 0.005% to 6% contribution to the total DOG ρ_{SFR} .

We note that Pope et al. (2008b) also examined bump (star-forming) DOGs at $z \sim 2$ and they calculated $\rho_{\text{SFR}} \sim 1 \times 10^{-2}\ \text{M}_{\odot}\text{yr}^{-1}\text{Mpc}^{-3}$. This value is lower than the bump $\rho_{\text{SFR}} = 1.9 \pm 0.3 \times 10^{-2}\ \text{M}_{\odot}\text{yr}^{-1}\text{Mpc}^{-3}$ that we measure. However, it is difficult to determine whether these two values are significantly different because Pope et al. (2008b) do not

provide an error on their measurement. We use their reported fractional error on the average IR luminosity ($1.1 \pm 0.7 \times 10^{12}$) to estimate that the minimum error on their ρ_{SFR} is $\sim 0.6 \times 10^{-2} \text{ M}_{\odot}\text{yr}^{-1}\text{Mpc}^{-3}$, in addition to the contribution from the counting error from their 62 sources (compared to our 1137 bump sources at $z = 1.5 - 2.5$). We also note that the selection criteria for the two studies are slightly different and if we were to use the Pope et al. (2008b), we would identify 100 fewer bump DOGs (9% of bump DOGs are at $z = 1.5 - 2.5$). Therefore, we conclude that the two results are consistent, with our measurement providing a more accurate determination.

2.3.3 Stellar Mass Build-up

Using the stellar masses derived in Ilbert et al. (2010) (corrected to assume a Salpeter IMF by adding +0.24 dex), and our derived star-formation rates using *Herschel* data, we investigate where DOGs lie in the star-formation rate – stellar mass (SFR – M_*) plane. Disk galaxies with a steady star-formation mode are observed to form a tight correlation in their star-formation rates as a function of stellar mass, defining a “main sequence” (Daddi et al., 2007; Elbaz et al., 2011). Outliers in this relation are thought to be merger-driven starburst galaxies (Rodighiero et al. 2011 and references therein). In the top panel of Fig. 2.9 we show the star-formation rates and stellar masses for *Herschel*-detected DOGs, considering only those at $z = 1.5 - 2.5$ to minimize the effects of redshift evolution. Average error bars are plotted for star-formation rates and the uncertainties in stellar mass are fixed to 0.5 dex, which covers the systematic offset range due to the choice of extinction laws and stellar population synthesis models.

Fig. 2.9 shows that power-law DOGs and bump DOGs cover the same ranges in stellar mass and star-formation rate in the SFR – M_* plane, as expected if the far-IR is star-formation dominated. Our findings are also consistent with previous studies that investigated the

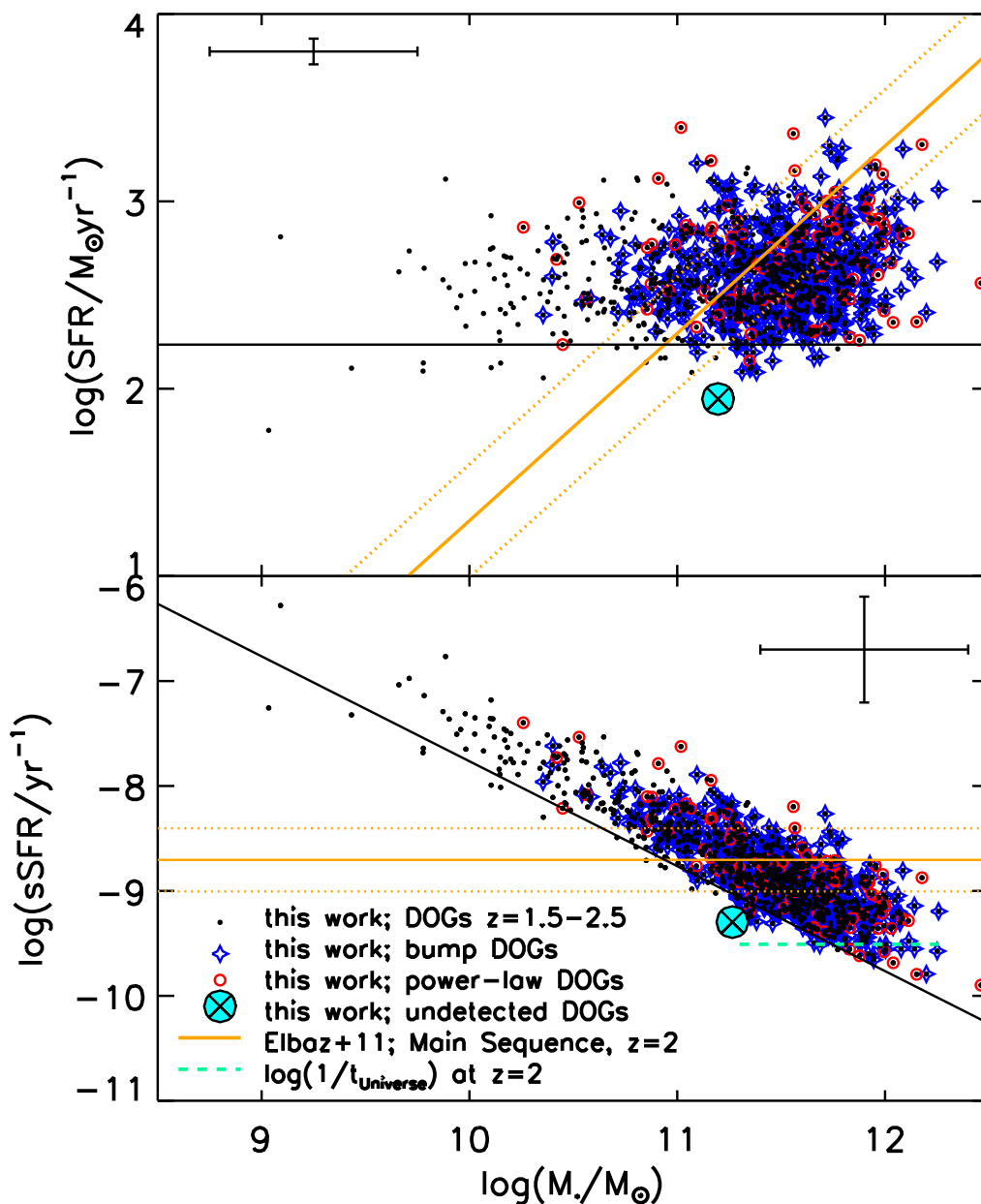


Figure 2.9: Star formation rates and specific star-formation rates for DOGs at $z \sim 2$. Power-law DOGs and bump DOGs are statistically indistinguishable in the $\text{SFR} - M_*$ plane. The sSFR at $z = 2$ using the relation for star-forming galaxies from Elbaz et al. (2011) and its conversion to SFR for the displayed range of masses is shown as the thick solid orange line in both panels. The orange dotted lines represent a factor of two dispersion from the derived SFR and sSFR . DOGs have a large scatter about the main sequence relation, having sources in the starburst, main sequence, and passive galaxy regimes. The thin horizontal black line in the top panel represents a minimum detectable star-formation rate at $z \sim 2$, caused by the $24 \mu\text{m}$ flux density limit. Converting this to an sSFR value results in the diagonal line in the bottom panel, leading us to conclude that the apparent negative correlation between sSFR and stellar mass is a selection effect.

similarities in properties of far-IR SEDs of *Herschel*-selected star-forming galaxies and AGN (Mullaney et al., 2012).

The infrared main sequence from Elbaz et al. (2011) for *Herschel*-selected star-forming galaxies at $z = 2$ is also shown in Fig. 2.9. DOGs have a significant amount of scatter about this relation, with 46% within a factor of 2 of the main-sequence, 24% above it and consistent with starbursts, and 31% below it in the more quiescent regime.

The bottom panel of Fig. 2.9 shows the specific star-formation rate ($\text{sSFR} = \frac{\text{SFR}}{M_*}$) as a function of stellar mass. The sSFR quantity measures the efficiency of star-formation, with its inverse giving a characteristic time-scale for the current burst length of star-formation activity. An apparent negative correlation in which lower mass DOGs exhibit higher sSFRs than their higher mass counterparts is observed for DOGs at $z = 2$, however this is largely a selection effect due to the flux limit of our sample. On the top panel of Fig. 2.9 we use the minimum IR luminosity at $z = 2$ from our sample to represent a minimum detectable star-formation rate limit, shown as the horizontal line. We convert this to an sSFR value for a range of masses and this is shown as the diagonal line in the bottom panel. The logarithmic inverse age of the Universe in Gyr at $z = 2$ is ≈ -9.5 (dashed line in Fig. 2.9) and most DOGs have sSFRs larger than this, indicating that the observed phase of star-formation could be responsible for their observed stellar mass.

Finally, we use the known redshift distribution and the sSFRs of DOGs to compare their volume densities to their likely progenitors, SMGs. We estimate that the volume density of observed DOGs at $z = 1.5 - 2.5$ is $8 \times 10^{-5} \text{ Mpc}^{-3}$. Using the median DOG sSFR to assume a characteristic lifetime of the DOG phase to be ~ 1 Gyr, we can correct this density for the burst duty cycle to derive a volume density for the progenitors to be $\sim 1 \times 10^{-4} \text{ Mpc}^{-3}$. This is consistent to the SMG volume density derived from Wardlow et al. (2011) at $z = 1.5 - 3$, which assumes the lifetime of the SMG phase to be 100 Myr, 10 times shorter than for DOGs. In this scenario, DOGs would have the same descendants as $z \sim 2$ SMGs, which, as

discussed in Wardlow et al. (2011) and Hickox et al. (2012), are likely to be $2-3L^*$ early-type galaxies.

Chapter 3

Gravitationally Lensed *Herschel*-selected Galaxies

3.1 Background

Dusty star-forming galaxies (DSFGs; For a recent review, see Casey et al., 2014), selected for being bright in the infrared or sub-mm regimes, are responsible for the bulk of cosmic star-formation in the early Universe (e.g. Le Floch et al., 2005; Takeuchi et al., 2005). Submillimeter galaxies (SMGs, Smail et al. 1997; Hughes et al. 1998; Barger et al. 1998 and see Blain et al. 2002 for a review), an 850 – 880 μm -bright subset of the DSFG population, present an appealing opportunity to study an important phase in galaxy evolution at the peak of cosmic star-formation. The negative K -correction in the Rayleigh-Jeans tail of thermal dust emission at the (sub-)mm regime forms an approximately constant infrared (IR) luminosity limit across a wide range in redshift ($z = 1 - 8$). This effectively allows SMGs to be readily detected in sub-mm surveys. Since their discovery 17 years ago, we have learned that SMGs are massive ($M_* \sim 10^{11} M_\odot$; Michałowski et al. 2010; Hainline et al.

2011; Bussmann et al. 2012; Targett et al. 2013), gas-rich ($M_{\text{gas}} \sim 10^{10-11} M_{\odot}$; Greve et al. 2005; Tacconi et al. 2008; Ivison et al. 2011; Bothwell et al. 2013), and metal-rich ($Z \sim Z_{\odot}$; Swinbank et al. 2004) galaxies at a median redshift of $z \sim 2.5$ (Chapman et al., 2005) that could be undergoing a short burst of star-formation ($t \sim 50 - 100$ Myr; Tacconi et al. 2008; Narayanan et al. 2010; Lapi et al. 2011; Hickox et al. 2012; Simpson et al. 2013). They have the most extreme star-formation rates, which can be as high as $10^3 M_{\odot} \text{ yr}^{-1}$ and compose 20–30% of the total comoving star-formation rate density (ρ_{SFR}) at $z \sim 2.5$ (Chapman et al., 2005; Wardlow et al., 2011; Casey et al., 2013). This is comparable to the total contribution of mid-IR selected galaxies at the same epoch, although SMGs are fewer in number but have larger IR luminosities (e.g. Farrah et al., 2008; Hernán-Caballero et al., 2009; Calanog et al., 2013).

From an evolutionary standpoint, it has long been proposed that ultra-luminous infrared galaxies (ULIRGs, $L_{\text{IR}} \geq 10^{12} L_{\odot}$), which include SMGs, is an intense star-forming phase that precedes the growth of the AGN hosted by massive elliptical galaxies (Sanders et al., 1988). Multiple lines of evidence suggest that SMGs are the likely progenitors of massive elliptical galaxies (Lilly et al., 1999; Swinbank et al., 2006; Tacconi et al., 2008; Michałowski et al., 2010; Lapi et al., 2011; Hickox et al., 2012; Toft et al., 2014). For instance, $\leq 30\%$ of SMGs are known to harbor AGN, supporting formation scenarios in which massive elliptical galaxies evolve from a quasar-dominated phase (Alexander et al., 2003; Pope et al., 2008b; Coppin et al., 2010). Furthermore, clustering analyses indicate that SMGs are hosted by $10^{13} M_{\odot}$ dark matter halos and have space densities of $\sim 10^{-5} \text{ Mpc}^{-3}$, consistent with optically-selected quasars at $z \sim 2$ and $2 - 3 L^*$ elliptical galaxies at $z \sim 0$ (e.g. Blain et al., 2004b; Farrah et al., 2006; Hickox et al., 2012).

While our knowledge of SMGs have definitely advanced, their dominant formation mechanism is still unclear. One picture proposes that SMGs are a result of gas-rich major-mergers (Tacconi et al., 2006; Schinnerer et al., 2008; Tacconi et al., 2008; Engel et al., 2010)

while another favors them as being extreme analogues of normal star-forming galaxies, fed with gas through minor mergers and smooth infall (Finlator et al., 2006; Dekel et al., 2009; Davé et al., 2010). Observational studies that focus on SMG morphologies can help clarify this issue, and would require analysis in wavelength regimes that trace the constituent gas, dust, and stars. However, SMG morphologies are difficult to study with current instruments because of poor spatial resolution, insufficient sensitivity, or both. Here, we circumvent these difficulties by studying SMGs that are strongly gravitationally lensed. The lensed background source receives a boost in apparent flux by a factor of μ , where μ is the magnification factor, enabling the study of emission that would otherwise be too faint to detect. In addition, the apparent size of the background source is increased by a factor of $\sim \sqrt{\mu}$ (Schneider 1992) – allowing high-spatial resolution studies of the lensed galaxies, even if they are at high redshift.

The obvious benefits of studying SMGs via gravitational lensing sparked interest in producing an efficient and straight-forward method to identify strong-lensing events. Efficient strong lensing event identification through bright source selection in wide-area extragalactic sub-mm/mm surveys has been long proposed (Blain, 1996; Perrotta et al., 2002; Negrello et al., 2007; Paciga et al., 2009). The idea behind this selection method exploits the fact that sources that are intrinsically sub-mm bright are also very rare (e.g. see Weiß et al., 2009). This implies that a significant fraction of the sub-mm bright population could be lensed and flatten the observed declining number counts at large flux densities. This flattening however, could also be caused by contaminants such as local late-type spiral galaxies and flat spectrum radio quasars (Negrello et al., 2007) which can be removed trivially through optical and radio surveys (e.g. SDSS, Abazajian et al. 2003; NVSS, Condon et al. 1998). Thus, after removing such contaminants, a large fraction of the brightest sub-mm sources are expected to be strongly lensed and lie at $z \geq 1$.

The launch of the *Herschel Space Observatory*¹ (Pilbratt et al., 2010) ushered in the possibility of confirming these theoretical predictions. Indeed, the two largest wide-area sub-mm surveys, the *Herschel* Multi-Tiered Extragalactic Survey (HerMES, Oliver et al. 2012) and the *Herschel* Astrophysical Terahertz Large Area Survey (H-ATLAS, Eales et al. 2010) have provided the first samples of candidate lensing systems by selecting 500 μm -bright sources. Since then, high-resolution, spatially-resolved multi-wavelength follow-up observations have confirmed that a large fraction (70 – 100%) of these candidates are undoubtedly lensed (Negrello et al., 2010; Gavazzi et al., 2011; Bussmann et al., 2012; Wardlow et al., 2013; Bussmann et al., 2013).

This chapter focuses on studying the background lensed galaxies with new high-resolution near-IR data for 87 500 μm -bright candidate lensing systems discovered by H-ATLAS and HerMES. A comprehensive analysis of the properties of the foreground lenses is deferred to a future publication (Amber et al., in prep.). Near-IR observations of *Herschel*-selected 500 μm -bright lensed SMGs allow one to characterize the stellar distribution at spatial resolutions that are unachievable with the current facilities. Furthermore, since classically-selected SMGs are 850 – 880 μm -bright, we can directly compare their rest-frame optical properties, such as their luminosities, against the 500 μm -bright population. This comparison can help clarify any differences between these two SMG populations, which can potentially arise from their sub-mm selections. Aside from their rest-frame optical luminosities, the morphological information recovered from reconstructing the background galaxy can also be used to compare against previous studies of unlensed SMGs (Swinbank et al., 2010; Targett et al., 2011, 2013; Aguirre et al., 2013). In this context, the morphological study of lensed SMGs at an unprecedented spatial resolution can provide observational evidence to determine the formation mechanisms that are present. Finally, these high-resolution near-IR observations compliments previous studies done on lensed SMGs using high-resolution sub-mm facilities

¹Herschel is an ESA space observatory with science instruments provided by European-led Principal Investigator consortia and with important participation from NASA.

(Bussmann et al., 2013; Weiß et al., 2013; Hezaveh et al., 2013; Vieira et al., 2013). Any sources that overlap between the near-IR and the sub-mm can be used to study the morphologies, spatial distribution, and the effects of differential magnification between the older stellar population and the dust-emitting star-forming regions of the same galaxy.

All of the candidate lensing systems in this study have been observed using either the *Hubble Space Telescope's* (HST) Wide Field Camera 3 (WFC3) in the *J* band (F110W, $\lambda=1.15\ \mu\text{m}$) or Keck II Near-Infrared Camera 2 (NIRC2) with laser guide star adaptive optics system (LGS-AO, Wizinowich et al. 2006) in the *K* ($\lambda=2.2\ \mu\text{m}$) band. We model the lensing in 12 galaxy-scale lensing systems with new near-IR data that have high-significance lensing morphology detections and sufficiently constrained configurations. From our lens models, we determine the magnification in the near-IR and the source-plane emission regions. Of these 12, six of the systems were also studied in the sub-mm by Bussmann et al. (2013). By comparing the lensing in the sub-mm and near-IR, we quantify the effects of differential lensing and measure the size difference of stellar and dust components. Using our near-IR data and lens models, we measure the intrinsic photometry for lensed SMGs and estimate their rest-frame absolute *B*-band magnitudes.

This chapter is organized as follows. In Section 3.2, we summarize the sub-mm lensed candidate selection and describe our high-resolution near-IR observations and data reduction process. Our classification of candidate lensing systems is presented in Section 3.3. Section 3.4 describes our lens modeling methodology and individual notes on each strong lensing system. We then discuss our results and compare them with previous studies of both lensed and unlensed SMGs in Section 3.5.

3.2 Lensed Candidate Selection and near-IR Observations

In this section we summarize the selection criteria used to define our sample and describe the data acquisition and reduction of our high-resolution near-IR imaging of the galaxies. A summary of all the targets observed, along with their integration times and observation dates are found on Table A.1. Of the 87 near-IR targets, 49 (56%) HerMES/H-ATLAS sources are observed with Keck/NIRC2-LGS-AO, 42 (48%) HerMES sources with *HST*/WFC3 F110W (with 15 (17%) HerMES sources observed using both instruments).

3.2.1 Selection of Lensed Candidates

The targets of this study are selected from the Spectral and Photometric Imaging REceiver (SPIRE, Griffin et al. 2010) maps in the HerMES (Oliver et al., 2012) and H-ATLAS (Eales et al., 2010) fields. Targets are identified in the same way in both surveys, using the SPIRE 500 μm channel to minimize the number of contaminants (Negrello et al., 2007, 2010). The *Herschel*-SPIRE data reduction and photometry procedures differ slightly for each survey, with the main difference being that HerMES accounts for blending from positional priors that can result in detecting fainter objects while H-ATLAS only retains sources above 5σ . Even with this difference, the 500 μm number counts appear consistent (Oliver et al., 2010; Clements et al., 2010). Full details of the H-ATLAS map-making data reduction and source extraction are presented in Pascale et al. (2011) and Rigby et al. (2011). For HerMES, see Levenson et al. (2010), Roseboom et al. (2010), and Smith et al. (2012), with updates in Viero et al. (2013) and Wang et al. (2013). Both procedures are summarized below.

For HerMES, SPIRE maps were generated using the SPIRE-HerMES Iterative Mapper (SHIM) algorithm (Levenson et al., 2010). The most updated point-source catalogues use

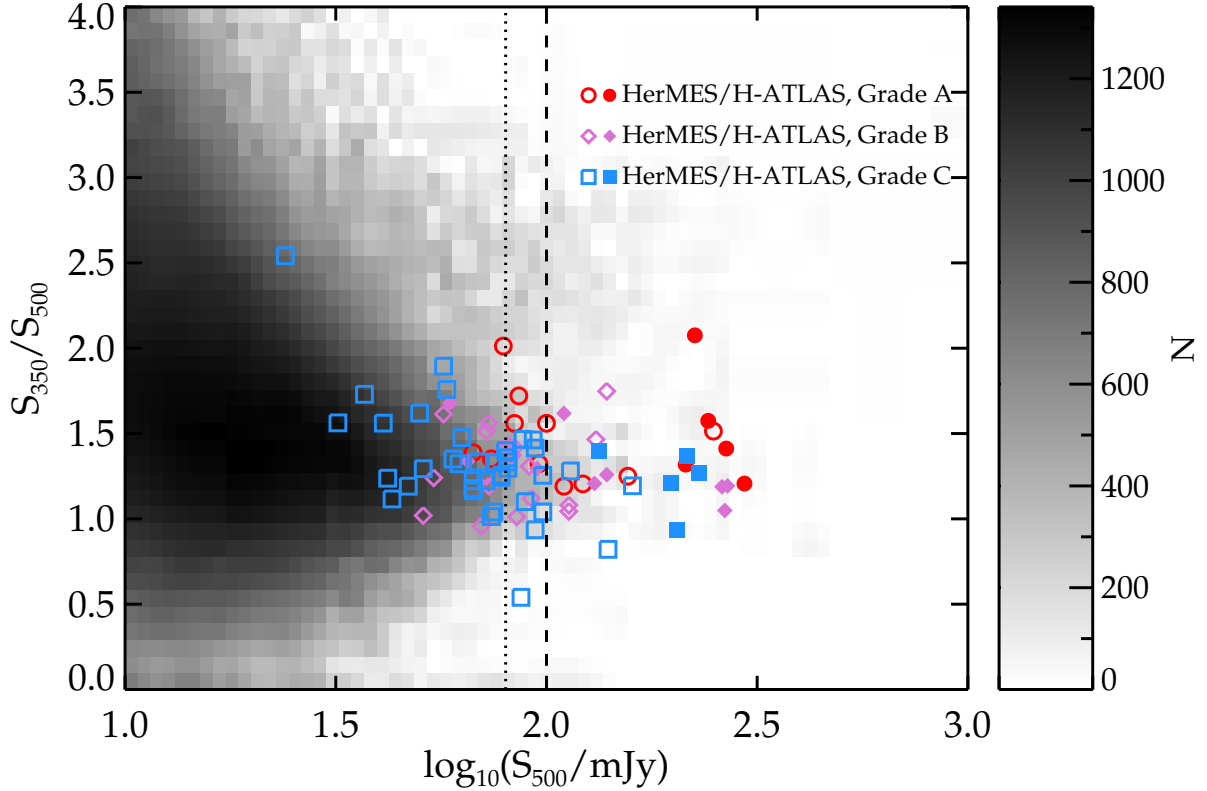


Figure 3.1: S_{350}/S_{500} and S_{500} for SPIRE galaxies in HerMES and H-ATLAS.

Open and filled symbols correspond to HerMES and H-ATLAS lensed candidates with high-resolution near-IR imaging, respectively. Red circles, violet diamonds and blue squares are assigned the Grade 1, 2, and 3, respectively, on the basis of their near-IR lensing morphologies, discussed in Section 3.3. The vertical dotted and dashed lines correspond to $S_{500} = 80$ and 100 mJy. The majority of the targeted lensed candidates are biased towards larger $500\ \mu\text{m}$ flux densities but have similar S_{350}/S_{500} ratios with the fainter population.

an iterative source-detection scheme of **STARFINDER** (Diolaiti et al., 2000) and De-blend SPIRE Photometry (**DESPHOT**) algorithm (Roseboom et al., 2010, 2012; Wang et al., 2013). **STARFINDER** is used to detect and find the optimal positions of point sources in SPIRE maps by assuming that the observed images can be modeled as a superposition of point-response functions (PRF). These source positions are then used as inputs for **DESPHOT** to perform map segmentation (de-blending), source photometry, background estimation and noise (instrumental and confusion) estimation.

For sources identified by H-ATLAS fields, source extraction is performed using the Multi-band Algorithm for Source eXtraction (**MADX**; Maddox et al. in prep) on *Herschel* Interactive Processing Environment (HIPE) generated SPIRE maps (Pascale et al., 2011). **MADX** iteratively performs PSF fitting and subtraction to measure flux densities and positions for each band. Sources that are detected at $\geq 5\sigma$ (including confusion noise of ≈ 6 mJy at all bands, Nguyen et al. 2010) in any of the bands are retained in the final catalogues.

In both surveys lensing candidates are selected by applying a high flux cut at $500\ \mu\text{m}$, which for H-ATLAS is $S_{500} \geq 100$ mJy (Negrello et al., 2010), where S_{500} is the $500\ \mu\text{m}$ flux density, and for HerMES is $S_{500} \geq 80$ mJy (Wardlow et al., 2013). Sources that are not associated with local late-type galaxies or flat-spectrum radio galaxies are retained as lensing candidates. The targeted sources are presented in Table A.2, along with their SPIRE 250, 350 and $500\ \mu\text{m}$ flux densities and redshifts.

We should also clarify that our selection in HerMES at $S_{500} \geq 80$ mJy was applied on an initial source catalog, extracted from blind detections using **SUSSEXtractor** (Savage & Oliver, 2007; Smith et al., 2012), but subsequent iterations of HerMES data products resulted in better deblending of $500\ \mu\text{m}$ flux densities with $250\ \mu\text{m}$ positions as a prior (Wang et al., 2013). This results in some of the sources initially categorized as candidate lensing systems (having $S_{500} \geq 80$ mJy), with a final lower probability of being lensed at $\leq 40\%$, based on the statistical models of Wardlow et al. (2013) that uses the foreground lensing matter

distribution, unlensed SMG number counts, and an assumed SMG redshift distribution. As a result, some are confirmed as bonafide lenses and we keep them in our sample, as they have been followed-up but we exclude them for statistics involving lensed SMGs at the bright $500\ \mu\text{m}$ flux densities.

Figure 3.1 shows S_{500} as a function of the flux density ratio S_{350}/S_{500} for the targeted candidate lensing systems with high-resolution near-IR imaging. By design, our targeted sources are biased towards those that are brightest at $500\ \mu\text{m}$, although they have similar $350/500\ \mu\text{m}$ colors (with $S_{350}/S_{500} \geq 1$ for most systems) to the bulk of the SPIRE population. This indicates that *Herschel*-selected lensed galaxies and the SPIRE population have similar far-IR SED shapes, dust temperatures, and redshift distribution but will have larger apparent IR luminosities due to flux boosting effects from lensing (Wardlow et al., 2013; Busmann et al., 2013).

3.2.2 Keck NIRC2/LGS-AO

We have obtained Keck/NIRC2 LGS-AO imaging for *Herschel*-candidate lensing systems. Conditions were typically good, characterized by clear skies and seeing values of $\sim 0.8''$ from our successful observing runs from 2011 to 2013. We observe our targets primarily using the K_s filter ($\lambda_c = 2.2\ \mu\text{m}$), mainly because Keck-AO performs the best at longer wavelengths and K_s gives the optimal sensitivity because the background is minimal at this wavelength (Simons & Tokunaga, 2002). Typical integration times for each source are ~ 45 minutes to acquire a 5σ point source depth of 25.7 AB using a $0.1''$ aperture radius. We use the wide camera that has a $40'' \times 40''$ field of view and sub-arcsecond dithering steps. The spatial resolution with AO correction reaches $0.1''$ in the best conditions and the estimated Strehl ratios were $\sim 15 - 25\%$. Some of the targets showing clear signs of lensing, are also observed in the H ($\lambda_c = 1.6\ \mu\text{m}$) band. However, we do our lens modeling (Section 3.4)

only in the K band where the signal to noise is at its highest. We used custom IDL scripts to reduce the images, following standard procedures (Fu et al., 2012, 2013). Briefly, after bad pixel masking, background subtraction, and flat-fielding, sky background and object masks were updated iteratively. For each frame, after subtracting a scaled median sky, the residual background was removed with 2-dimensional B-spline models. In the last iteration, we discard frames of the poorest image quality and correct the camera distortion using the on-sky distortion solution from observations of the globular cluster M92². Since image distortion has been removed in previous steps, astrometry is calibrated against four to five non-saturated SDSS sources in the final mosaicked field of view with a linear offset. The mean offset is weighted by the S/N of the sources, so that offsets computed from brighter sources carry more weight.

The NIRC2 images are flux calibrated against UKIDSS K_s -band photometry, when available. Each frame is PSF matched and corrected for airmass and we use the UKIDSS aperture radius of $1''$ to perform our calibration. Photometric zero points are derived by calculating the magnitude difference for overlapping sources. For NIRC2 frames that do not overlap with UKIDSS footprints, we use the night-averaged zero point and its standard deviation to account for the associated systematic error.

For the PSF used in our lens modeling analysis (Section 3.4), we use a nearby unsaturated point source, whenever available. Otherwise, point sources from other images observed on the same day are used, while keeping the airmass difference within 0.2 and applying the appropriate rotation.

3.2.3 HST/WFC3

Herschel-lensing candidates in the HerMES fields have also been observed as part of the *HST*

²<http://www2.keck.hawaii.edu/inst/nirc2/dewarp.html>

WFC3 Cycle 19 snapshot program (P.I. M. Negrello). All are observed with the F110W filter ($\lambda_c = 1.15 \mu\text{m}$), using a 4-point parallelogram dither pattern with point and line spacings of $0.57''$ and $0.36''$, respectively. Most of the images have a total integration time of 4 minutes per target, while a few sources that have red SPIRE colors ($S_{500} \geq S_{350}$) have doubled integration times, because these sources could be at higher redshifts and thus likely fainter than in near-IR (Dowell et al., 2014).

The `calwfc3` processed flat-fielded data from the *HST*/WFC3 pipeline are used as inputs for `multidrizzle` (Koekemoer et al., 2003), producing an output image with a pixel scale of $0.04''$ to allow adequate sampling of the PSF and to match the pixel scale of the Keck images. Due to some fields being crowded by bright sources, we turn off sky subtraction on all WFC3 frames and set the drop size parameter, “pixfrac” = 1, in order to minimize additional noise due to sky variations. We set the “bits” parameter to the value of 4608 to include pipeline-rejected pixels and dust motes, since our dithering pattern is not large enough to fill in these regions with good data. To account for the uncertainty in each pixel value, an error map is generated to account for the RMS value of the sky and the Poisson error each pixel. The resulting output images have a spatial resolution of $\sim 0.2''$ and an average 5σ point source depth of 25.4 and 26.2 AB mag for integration times of 4 and 8 minutes, using a $0.2''$ aperture radius.

We use a different PSF extraction method for *HST*/WFC3 images. Since *HST*/WFC3 covers a field of view of $2' \times 2'$, we use `starfinder` to stack on unsaturated point sources within the image to generate the PSF used for our lens modeling analysis.

3.3 Classification of Lensing Candidates

For our 87 lensing candidates with high-resolution near-IR data, we implement a two-step grading rubric to identify sources for which we could perform our lens modeling analysis to derive magnification factors and recover the intrinsic properties of the SMG. In this section, we describe our rubric that prioritizes bonafide lensing morphologies and available redshifts for the background source. The resulting grade for each candidate lensing system is listed in Table A.2 and our grading rubric is summarized in Table 3.1.

3.3.1 Visual Identification of Lensing Morphologies

For each target we assign a letter grade based on the existence and quality of any lensing features that are present in the near-IR data. Candidates that are classified as Grade A are of high-priority and are what we assume to be confirmed lensing systems. To the zeroth order, these are typically sources that show obvious lensing morphology such as rings, arcs, and counter-images, detected at high-significance. Some candidates that are more ambiguous (e.g. HLock12, HFLS08, and HECDFS05) are also classified as Grade A when a possible counter-image after subtracting the foreground galaxy is revealed and the observed lensing configuration can be successfully modeled. As an additional check to boost our confidence, we also confirm if the suspected near-IR lensing morphologies trace the observed configuration from existing high-resolution sub-mm data (Bussmann et al., 2013) or be located within the beam ($3 - 4''$) of radio observations for blind spectroscopy (Riechers et al., in prep.). Grade B sources can usually be described as systems with ambiguous low signal-to-noise features surrounding a relatively brighter galaxy which could either be due to lensing or be part of the galaxy itself. Deeper high-resolution data or observations in different wavelength regimes are needed to confirm the lensing status of these systems. These sources may also be intrinsically unlensed (Dowell et al., 2014) or only moderately lensed, such is the case with

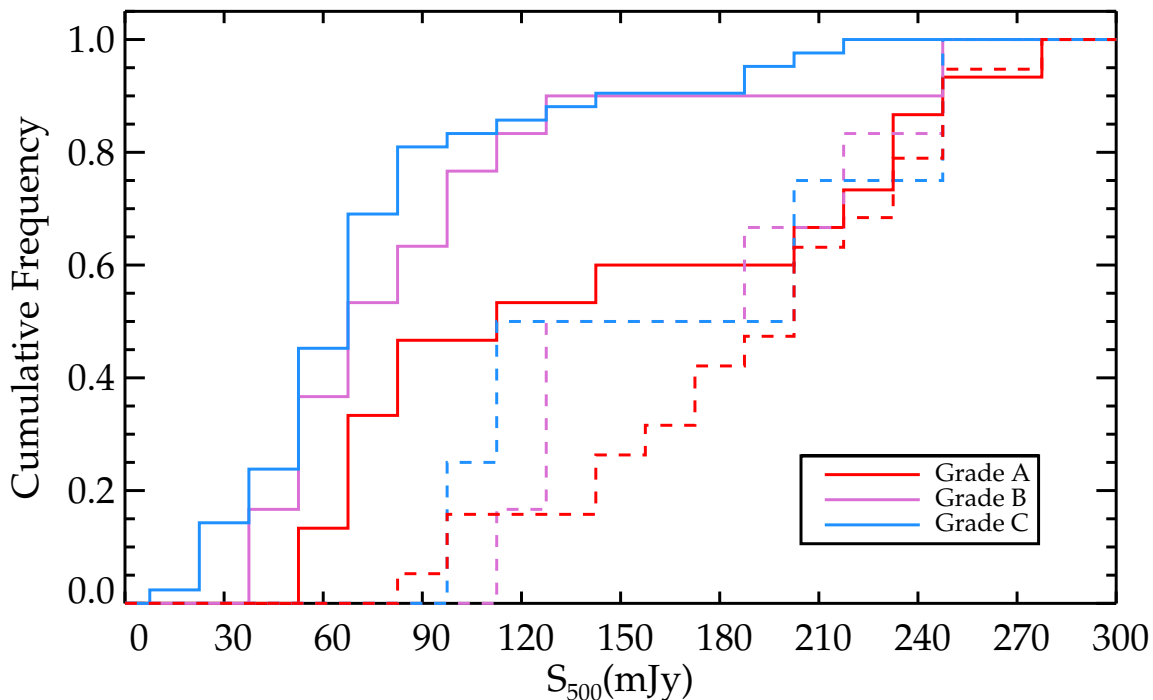


Figure 3.2: Cumulative frequency distribution of S_{500}

Red solid, blue dashed, and green dashed-dotted lines represent Grade 1, 2, and 3 sources respectively. The solid red, purple, and blue lines represent Grade A, B, and C sources respectively. For comparison, the dashed lines are from the sub-mm sample from Bussmann et al. (2013), converted to the same near-IR grading scheme. Grade A sources tend to have smaller cumulative fractions than Grade B and C sources with increasing values of S_{500} , which supports the idea that $500 \mu\text{m}$ -bright sources have a higher probability of being lensed.

HXMM01 (Fu et al., 2013). Grade C sources are assigned to candidates of lowest priority for our study. The near-IR images for these targets typically show no detections within $15''$ of the measured $250 \mu\text{m}$ SPIRE position or sources with compact irregular morphologies that do not resemble any lensing morphologies. Like Grade B systems, we also interpret that our sample of Grade C sources could also include sources that are intrinsically bright in the far-IR. The near-IR lens models presented in this paper focuses on Grade A sources, which are shown in Fig. 3.3.

3.3.2 Redshift Availability

Redshifts are needed to convert observed parameters into physical quantities. Spectroscopic followup programs at (sub)mm and optical/near-IR wavelengths are still ongoing (e.g., Harris et al., 2012; Bussmann et al., 2013, Riechers et al in prep.). The existing redshifts are presented in Table A.2, and we use these data to assign a secondary letter grade from 1 through 4: 1 – redshifts available for both foreground lens and background SMG; 2 – redshift only available for the background SMG; 3 – redshift only available for foreground lens; 4 – no foreground lens or background SMG redshift. Note that our focus is to study the lensed SMG, we assign a higher grade for systems with background source redshifts.

For Grade A3 and A4 systems, we estimate the lensed SMG redshifts by fitting a modified blackbody using fixed parameters of $T = 35\text{K}$ and dust-emissivity parameter $\beta = 1.5$ to the *Herschel*-SPIRE photometry, which is the typical average dust temperature for SMGs and dust emissivity parameter used for dusty galaxies at high-redshift (e.g. Chapman et al., 2003; Kovács et al., 2006; Wardlow et al., 2011). These far-IR photometric redshifts have a large systematic uncertainty because of redshift-temperature degeneracy effects in the far-IR SED (Blain et al., 2004a) and should therefore be used with caution. This results to a minimum uncertainty of approximately $\Delta z \pm \sim 0.5$ for dust temperature variation of $\pm 10\text{K}$. Due to the inherent uncertainties associated with far-IR derived photometric redshifts, we do not use them in our analysis of the intrinsic properties of lensed SMGs (Section 3.5.3).

Table 3.1: Grading Rubric Summary for Lensed SMGs

NIR Lens Morphology	SMG/Lens Redshift	SMG only Redshift	Lens Only Redshift	Neither
Obvious	A1	A2	A3	A4
Marginal	B1	B2	B3	B4
None	C1	C2	C3	C4

3.3.3 Near-IR Strong Lensing Identification Efficiency

Negrello et al. (2007) predicted that, in the regime where $S_{500} \geq 100$ mJy, the surface density of unlensed SMGs is extremely low, defining a flux density cut in which a large fraction of the observed source counts are strongly lensed. Out of our 87 targets, 28 satisfy $S_{500} \geq 100$ mJy and 9 of these are confirmed strong lensing events (Grade A). This yields an efficiency of $\geq 32\%$ at the average depth of our near-IR data (Sec. 3.2). The remaining 72% could be unlensed or have faint lensing morphologies that fall below our near-IR detection limits. In addition, our near-IR sample of candidate lensing systems with $S_{500} \geq 100$ mJy is incomplete and does not include SMGs from other studies observed at different depths and wavelengths (e.g., Lensed SMGs from the H-ATLAS SDP sample, Negrello et al. 2014; Dye et al. 2014). For these reasons, we conclude that 32% is a lower limit for the near-IR lensing efficiency rate. If we also treat the 11 Grade B candidates with $S_{500} \geq 100$ mJy as confirmed lensing events to determine an upper limit, the near-IR lensing efficiency rate increases to 71%. These limits are consistent with the predicted 32 – 74% strong lensed fraction at $S_{500} \geq 100$ mJy from the statistical models of Wardlow et al. (2013). To get an idea how this efficiency can improve as a function of near-IR depth, the H-ATLAS SDP sample (Negrello et al., 2014; Dye et al., 2014), also observed using *HST*/WFC3 F160W with 5σ point source depths of >26.8 mag using > 60 min. integration times, confirmed lensing to be present for all 5 candidate lensing systems with $S_{500} \geq 100$ mJy. For comparison, the Bussmann et al. (2013)’s sample of lensed SMGs with $S_{500} \geq 100$ mJy observed with the Sub-Millimeter Array (SMA), 25 out of 30 candidates (83%) with a depth of $5\sigma \sim 15$ mJy showing evidence of moderate to strong lensing in the sub-mm maps. Of the 12 sources with high-resolution near-IR data that are confirmed to be lensed ($\mu_{880} \geq 2$) in Bussmann et al. (2013), six are Grade A (NB.v1.78, HBoötes02, NB.v1.43, G09v1.40, HLock01, HLock04), four are Grade B (HXMM02, G09v1.97, NA.v1.195, HBoötes03), and the two remaining are Grade C (G09v1.124, G15v2.779).

The lower near-IR efficiency for identifying strong-lensing events relative to sub-mm confirmations is not surprising. If a source is detected in both the sub-mm and the near-IR has two different spectroscopic redshifts, one can use small but significant offsets between the two images as evidence for lensing. This is useful in cases for which the observed sub-mm emission does not resemble convincing lensing morphologies (e.g. HXMM02, HBoötes03). There are also different possibilities to explain the lower efficiency associated with near-IR lensing identifications, which include the background SMGs suffering from heavy dust-obscuration, being intrinsically faint in the rest-frame optical, or lying at a high redshift. A geometric argument could also be made for the cause of non-detections, in which the near-IR emission is significantly offset from the sub-mm emission and the central caustic, thus lying in regions of low magnifications on the source-plane. In all alternative cases, this could lead to the observed near-IR emission from the background SMG to fall below our detection limits despite showing a bonafide lensing morphology in the sub-mm (e.g., G15v2.779, Bussmann et al. 2012).

Figure 3.2 shows the cumulative frequency distribution of S_{500} for all the targeted sources with high-resolution near-IR data labeled with their associated grades. For comparison, we also show the SMA sample from Bussmann et al. (2013), where we convert the sub-mm grade to an equivalent near-IR grade ³. In both studies, Grade A sources tend to have smaller cumulative fractions than Grade B and C sources with increasing S_{500} . Despite the lower efficiency of identifying lenses relative to the sub-mm, our near-IR candidate lensing system classification is consistent with the prediction that confirmed strong lensing events tend to be the brightest in S_{500} , having a median $S_{500} \sim 122$ mJy and 9 out of the 16 (56%) Grade A sources have $S_{500} \geq 100$ mJy. Grade B sources have a median $S_{500} \sim 85$ mJy (11/30 with $S_{500} \geq 100$ mJy, 37%) while Grade C sources have a median $S_{500} \sim 78$ mJy (8/42 with $S_{500} \geq 100$ mJy, 19%). The sub-mm sample from Bussmann et al. (2013) shows a

³The following describes the grading scheme conversion from this paper to Bussmann et al. (2013): A1 = A, A2 + A3 = B, B1 = C, A4 + B2 + B3 + B4 + C1 + C2 + C3 + C4 = X.

contrasting result and have median S_{500} values of 214, 200, and 216 mJy for Grade A, B, and C sources (using the near-IR scheme), respectively. However, we note that this could be due to the smaller sample size (30 sources total, 20 Grade A, 6 Grade B, and 4 Grade C), and the larger applied flux cut ($S_{500} \geq 80$ mJy) to select the sub-mm candidate lensing systems.

3.4 Lens Models

3.4.1 General Methodology

For each lensing system we use `galfit` (Peng et al., 2002) to model the surface brightness profile of the foreground lens and subtract it from the image. We use Sérsic profiles on foreground galaxies that resemble an elliptical morphology and edge-disk profiles for edge-on disks (G15v2.19 and HBoötes02). Foreground lens subtraction can also reveal close counter-images required to constrain the lens model (Cooray et al., 2011; Hopwood et al., 2011; Negrello et al., 2014; Dye et al., 2014). Any observed lensing features and nearby sources that are not associated with the lensing galaxy are masked out. The foreground lens subtracted image is then used as the input image for our lens modeling.

In cases where the emission from the foreground lens and background source are blended, we implement an iterative process in order to obtain an optimal lens model (Cooray et al., 2011). Using the `galfit` residual as the initial input, we derive a preliminary lens model. After achieving an acceptable fit (χ^2_ν on the order of unity), we then subtract this lens model from the original image. For the second iteration, we then use `galfit` on this “lensing morphology-subtracted” image, effectively isolating the surface brightness profile of the foreground lens and eliminating the need to mask out the lensing morphology. The updated foreground-lens surface brightness profile from `galfit` is subtracted from the original data, which will then

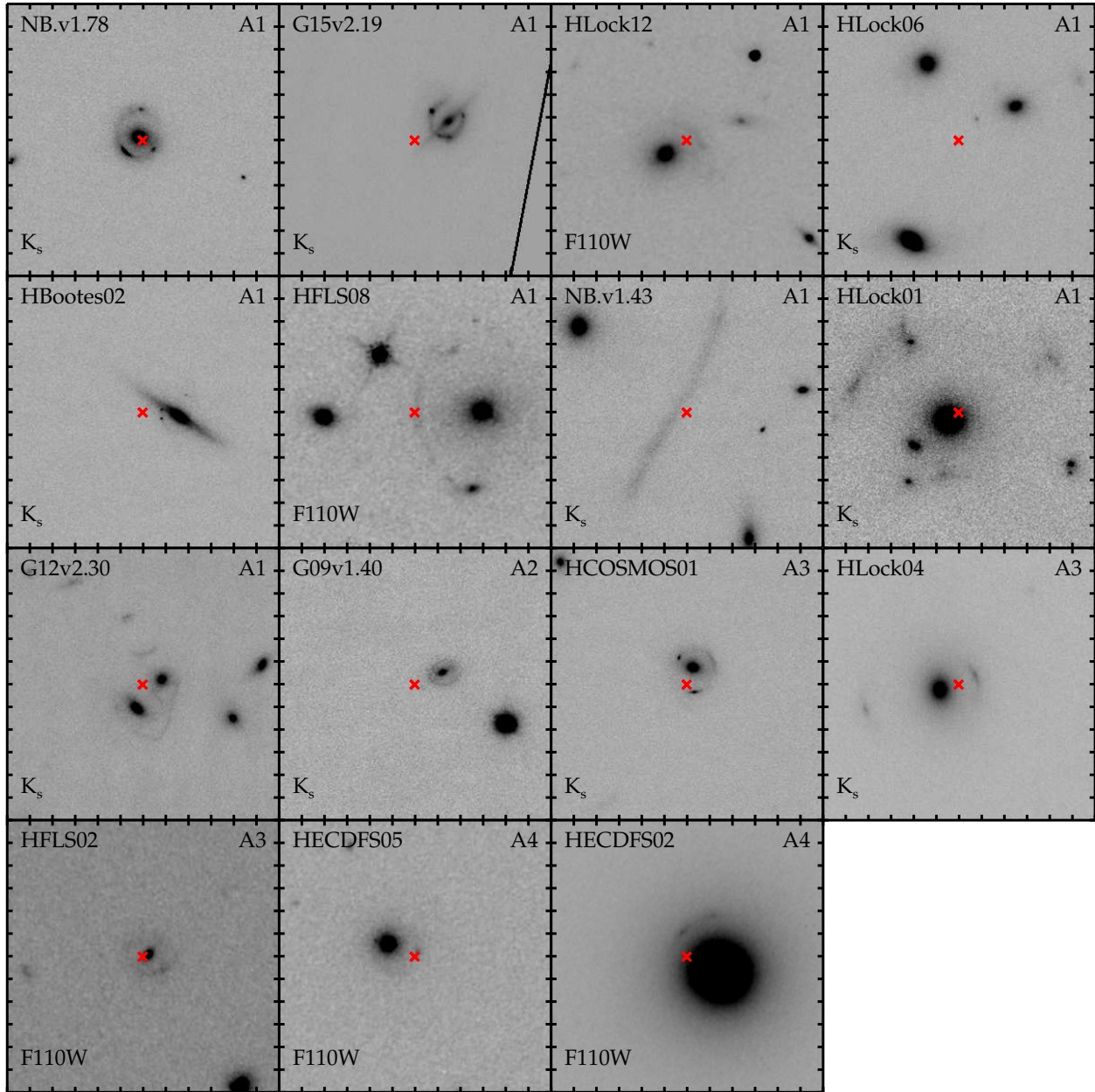


Figure 3.3: Grade 1 lensed candidates

$12''$ cutouts of all lens Grade A lensed SMGs, with each tick mark corresponding to $1''$ and oriented with north is up and east is left. All have either been observed using Keck NIRC2-LGS-AO K_s or *HST*/WFC3 F110W. The red cross marks the measured *Herschel* position. Contrast levels are varied in each image to highlight the observed lensing morphology.

serve as the new input for our lens modeling. This iterative method to obtain an optimal foreground lens subtracted image yields a $\Delta\chi^2_\nu \sim 0.2 - 0.3$ difference from the preliminary lens model, which corresponds to a $3 - 5\sigma$ improvement. The best-fit model for these blended lensing systems typically converges after 1 or 2 iterations.

For gravitational lensing, multiple images from the background source occur when the normalized surface mass density of the foreground lens, κ is greater than unity. In this paper, we assume a singular isothermal ellipsoid (SIE; Kormann et al., 1994) for κ , with the convergence at a point (x, y) in the image plane defined as:

$$\kappa(x, y) = \frac{\Sigma}{\Sigma_{\text{crit}}} = \frac{\sqrt{1+q^2}}{2} \frac{b}{2q\sqrt{x^2 + y^2/q^2}} \quad (3.1)$$

where Σ is the surface mass density, Σ_{crit} is the critical surface mass density, b is the critical or Einstein radius and q is the axis ratio. The SIE profile has been found to reproduce observed configurations of galaxy-galaxy strong lensing events (see Treu 2010 for a recent review) and has been successfully used in modeling lensed SMGs (Fu et al., 2012; Busmann et al., 2012, 2013; Hezaveh et al., 2013). The fitting parameters we use to describe the foreground SIE profile are the Einstein radius (b), distance from the measured `galfit` centroid $(\delta x, \delta y)$ in RA and DEC, ellipticity ($\epsilon_{\text{lens}} = 1 - q$), and the position angle (θ_{lens} , east of north). The components of the background galaxy in the source plane are assumed to have Sérsic profiles (Sersic, 1968). While the use of Sérsic profiles may oversimplify the morphology of the high redshift star-forming population, previous studies have shown that this approach provide useful information about their morphologies, such as intrinsic size, shapes and orientations for both lensed and unlensed SMGs (Swinbank et al., 2010; Gavazzi et al., 2011; Targett et al., 2011, 2013; Aguirre et al., 2013). The fitting parameters of the background Sérsic profile are the flux (F), position $(\delta u, \delta v)$ from the measured foreground lens center of mass, ellipticity (ϵ_{source}), position angle (θ_{source} , defined east of north), effective semi-major axis (a_{eff}), and the Sérsic index (n). For all systems, we start with the simplest model for the background

galaxy (1 source) and increase the components to check if this provides a significantly better fit ($\Delta\chi^2_{\nu} \geq 0.3$).

These model parameters are all varied consistently for each lensing system. The Einstein radius is typically allowed to vary within $\pm 0.5''$ from a circular radius that encloses the observed lensing morphology. The lensing mass is centered on the measured `galfit` position of the foreground lens, which is varied within an area defined by the FWHM of the PSF. The ellipticities are allowed to vary from 0.0 to 0.8, and the position angles from -90° to 90° , with the initial values of both set to the midpoints of these ranges. The background galaxies are initially placed in perfect alignment with the foreground lens and are allowed to explore the position space within ± 0.75 times the Einstein radius, which is a valid assumption, since the detection of multiple counter-images is an indication that these sources are within the vicinity of the source-plane caustics. Indeed, the maximum observed offset from direct alignment between the foreground and background galaxy is 40% of the Einstein radius (HECDFS02). The effective semi-major axis length has an initial value of $0.3''$ with a minimum value of $0.01''$ and a maximum value of $1.00''$, based on half-light radii measurements of unlensed SMGs at $z \sim 2.5$ (Chapman et al., 2003; Swinbank et al., 2010; Targett et al., 2011, 2013; Aguirre et al., 2013). Sérsic indices are allowed to vary from 0.10 to 4.00. The integrated flux in the lens model and the input image are normalized consistently before being compared and where there are multiple background components flux ratios are computed. For each lensing system, the total number of parameters is equal to $5 \times N_L + 7 \times N_S - 1$, where N_L and N_S represent the number of lens and source components, respectively.

With a given set of initial parameters for the image and source plane, we use `gravlens` (Keeton, 2001) to generate a model of the lensed image. The model is convolved with the PSF to generate the expected observed image for each parameter set.

This PSF-convolved model is then compared with the foreground lens subtracted image within the fitting region, shown as the green contours on Fig. 3.4. These fitting regions are

initially hand-drawn to enclose all the suspected lensing morphologies in the data. After a preliminary lens model is derived, the fitting region is regenerated to enclose all pixels with values $\geq 1\sigma$, measured from the data (no noise is present from the model). Defining the fitting region through this process serves three main purposes: Firstly, it helps prevent the lens model from including pixels from the background which can make the fit insensitive and degenerate from varying the input parameters. This effectively makes the model fit for shot-noise dominated pixels. Secondly, it minimizes the under or over-subtracted regions from imperfect galfit subtractions that can cause the lens model to be fixated on these unwanted features. Thirdly, it accounts for any counter-images predicted by the model but not accounted for by the data, reducing the bias in our fit.

The process of comparing the lens model to the data is iterated using the IDL routine `amoeba_sa`, which performs multidimensional minimization using the downhill simplex method with simulated annealing (Press et al., 1992) on the χ^2 function, defined as:

$$\chi^2 = \sum_{x,y}^N \frac{(I_{\text{obs}}(x,y) - I_{\text{mod}}(x,y))^2}{\sigma(x,y)^2}, \quad (3.2)$$

where I_{obs} and I_{mod} is the surface brightness map of the observed and the model image, respectively, σ is the 1σ uncertainty map for the observed image that accounts for background and shot noise, x and y are the pixel coordinates, and N represents the number of pixels enclosed in the fitting region. Typically, $N \sim 200$ for the least constrained systems (e.g., double) and $N \sim 1000$ for the most constrained systems (Einstein rings or giant arcs). Depending on how well constrained the lensing system is, the correct configuration for the observed lensing morphology is usually obtained after the first few iterations of `amoeba_sa` and the probability of accepting worse solutions decreases for each iteration due to the simulated annealing. The rest of the calls are then spent on performing an extensive search around the optimal solution with the given configuration. All parameters and calculated quantities are saved in each iteration and the 1σ confidence interval for the best fit model

parameters are calculated from $\chi^2 - \chi_{\min}^2 \leq 1$. We note that χ^2 is renormalized to minimize correlated noise between pixels. This is done by dividing the total number of pixels of the original unbinned χ^2 values from the original images by the square area of the PSF (Fu et al., 2012).

The near-IR magnification factor μ_{NIR} is calculated in the same manner as in Bussmann et al. (2013). Briefly, we integrate the model flux (F_{SP}) within elliptical apertures with the same orientations and ellipticities as the model but with double the semi-major axis length. Then, these source plane elliptical apertures are mapped on to the image plane using the foreground lens model and the image plane flux is integrated (F_{IP}). The magnification factor is then simply a ratio of the two integrated fluxes, $\mu_{\text{NIR}} = F_{\text{IP}}/F_{\text{SP}}$, and is representative of total from all background source components.

To measure near-IR photometry, we use our fitting region to define the aperture and our results are listed in Table 3.4. The same aperture is also applied when measuring available multi-wavelength high-resolution near-IR data (Fig. A.4). Photometric statistical errors are measured by calculating the standard deviation of the total counts from non-overlapping background-dominated fields on the data, using the same sized aperture. A simple aperture correction is calculated by measuring the ratio of total counts from the lens model with and without the aperture. We divide the integrated flux densities by μ_{NIR} for each background source to obtain a magnification-corrected value.

3.4.2 Notes on Individual Lens Models

In this section, we provide notes on the basic characteristics for each lensing system with available lens models. We do not provide lens models for HLock01 and G12v2.30, as they have already been subjects of detailed studies from previous works (Gavazzi et al., 2011; Fu et al., 2012) and are also included in the sub-mm sample from Bussmann et al. (2013).

The SMGs with lens models derived here are shown in Fig. 3.4. The best-fit parameters along with the 1σ errors describing the foreground lens and the background source are presented in Tables 3.2 and 3.3. As a test for differential lensing and size comparison analysis in Section 3.5.1, we also generate lens models for the four new sources (NB.v1.78, HBoötes02, G09v1.40, and HLock04) that overlap with Bussmann et al. (2013), using the same foreground lens parameters reported in their paper, allowing the foreground lens position to vary within $0.3''$ to account for any astrometric offset between the near-IR and sub-mm data. The use of sub-mm derived foreground lens parameters generally yields poorer fits but is able to reproduce the observed near-IR lensing configuration. The lens models for this near-IR/sub-mm subsample are discussed on an object-by-object basis and shown in the Appendix.

NB.v1.78 (Grade A1): The K_s -band image shows a classic configuration observed when the background source lies on top of the caustic fold, the same configuration shown by the lensing system SDSS J0737+3216 (Marshall et al., 2007). The H -band image (Fig. A.4) shows a consistent configuration, but the lensing morphology is fainter. The multiple, well-separated arcs, in addition to the incomplete Einstein ring strongly constrains the lens model. The best-fit lens model requires two background Sérsic profiles to account for a compact, brighter and extended, fainter, component. The best fit model shows a compact source located off-center within an extended component, indicating an asymmetric morphology. Using a single component model yields a significantly worse fit ($\chi^2_{\nu}=1.50$) and fails to reproduce the extended Einstein ring. This source was also discussed in Bussmann et al. (2013), in which the SMA image reveal a similar configuration to the compact component in the K_s -band image. We measure a marginally lower magnification factor of $\mu_{\text{NIR}} = 10.8^{+0.3}_{-0.2}$, compared to $\mu_{880} = 13.0 \pm 1.5$ for the SMA data.

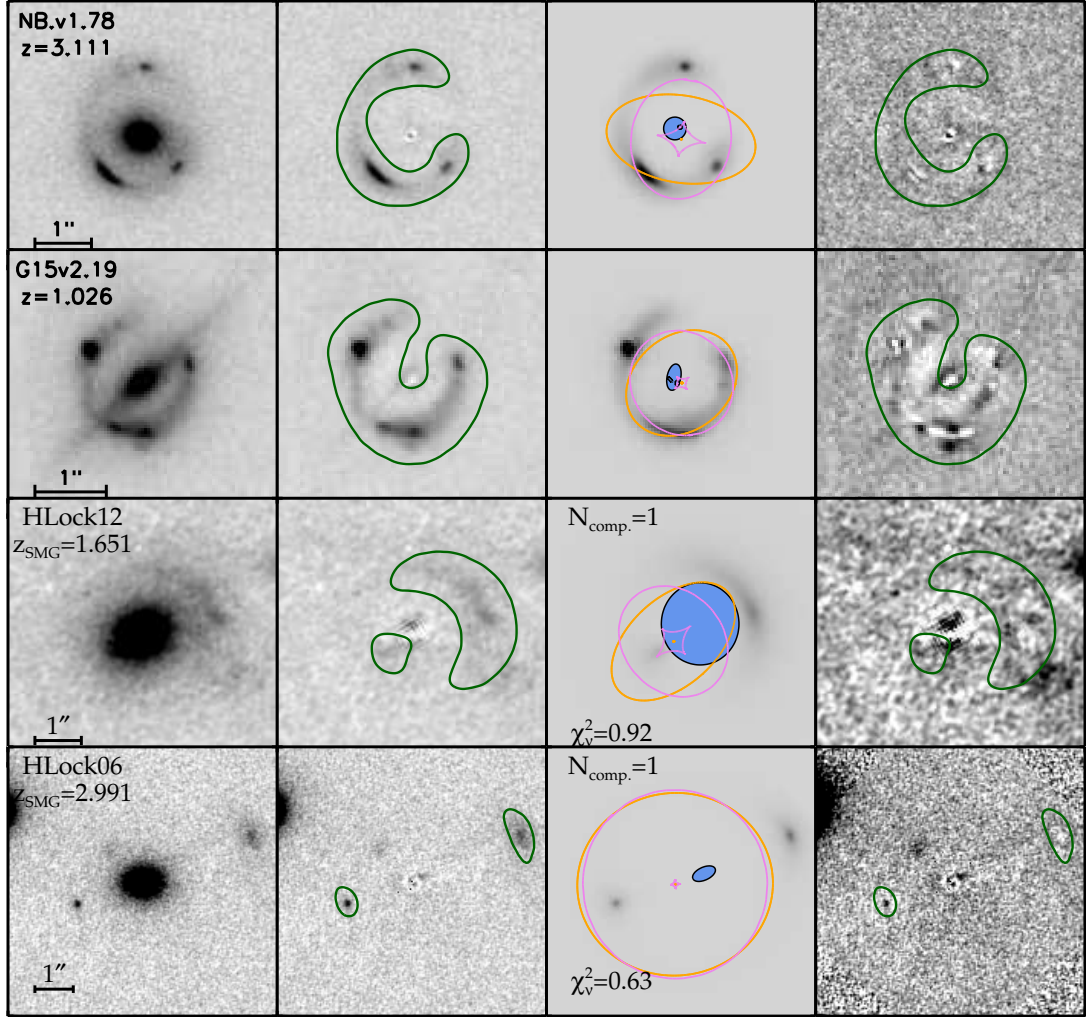


Figure 3.4: Near-IR lens models of Grade 1 systems.

North is up and east is left for all images. From left to right: postage stamp of observed image; foreground lens subtracted image; best-fit lens model; and the residual image. Green apertures enclose the final fitting region used. The orange and pink outlines trace the critical and caustic curves, respectively. Blue ellipses are the source plane models, displayed with the best-fit half-light semi-major axis, ellipticity, and position angle. Redshifts labeled with square brackets are photometric redshifts estimated from far-IR to sub-mm photometry and those without are spectroscopic. The third panel also lists the number of background components used in the best fit, denoted as N_{comp} and the reduced χ^2 , defined as $\chi_v^2 = \chi^2/N_{\text{DOF}}$.

G15v2.19 (Grade A1): The observed lensing morphology features a quad-like configuration accompanied by an incomplete Einstein ring, observed in both H -band and K_s -band images. The background source is being lensed by an edge-on disk and has the most complicated background galaxy model in our whole sample, requiring three components. It has the poorest fit, $\chi_\nu^2 = 2.6$, with both over- and under-subtracted regions that can be $\geq 5\sigma$. Using less than 3 components resulted in $\chi_\nu^2 > 5$. This system serves as an example in which substructure in the background source dominates, such that our assumed Sérsic profile is an inadequate description of the source. Furthermore, if the observed emission from the individual knots are from the same source, then their surface brightnesses should be somewhat comparable, which is a property of the counter-images in the image plane (Kochanek et al., 1989). Instead, we observe the surface brightness to be significantly inconsistent relative to each other, which supports our hypothesis that the morphology of the background source is highly complex and the observed emission is due to multiple background components.

We regard our lens model as a simple solution that can serve as a basis for future analysis on this object. Our source-plane reconstruction consists of two compact objects separated by $\sim 0.1''$ within a third extended elongated source. The positions of the two compact objects forms quads and double images in the observations, in which one of the counter-images from each component converge at roughly the same position in the image plane to produce the brightest knot located in the northeast. The extended component straddles the caustic, causing the incomplete Einstein ring. Due to the poor fit and under-subtracted regions in the residual image, the error bars in the magnification factor we report, $\mu_{\text{NIR}} = 9.6_{-0.3}^{+0.8}$, are most likely underestimated, since the contribution for the complexity of the system is not included. More extensive lens modeling of this will be discussed in Messias et al. (in prep.), which will also feature a nonparametric approach to multi-wavelength lens modeling.

HLock12 (Grade A1): The subtraction of the bright early-type galaxy reveals a counter-

image detected at 5σ located $1''$ east of the foreground lens. This constrains the lens model, which features a classic cusp configuration. The background SMG is extended with a half-light radius comparable to the foreground lens ($\sim 1''$). At $z = 1.7$, $1''$ is ~ 7 kpc, so this source is larger than the average for $z \sim 2.5$ SMGs (Aguirre et al., 2013; Targett et al., 2013, 2011; Swinbank et al., 2004; Chapman et al., 2003), although it is still consistent with other near-IR observations of SMGs at $z = 0.5 - 1.5$ (Mosleh et al., 2011). The *HST* image has multiple peaks in the arc, causing the residual image to contain under-subtracted regions. This could indicate the presence of substructure in the background source or the foreground lens. It is unlikely that the most prominent under-subtracted region, $\sim 2''$ south-west from the centroid of the arc emission, is associated with the background, since all variations of the lens model fail to reproduce any emission in this area, even when it is included in the fitting region and multiple components are allowed.

HLock06 (Grade A1): The lensing morphology of this source shows an arc to the west and a counter image to the east of the foreground lensing galaxy. The same features are also detected in the *HST* image (Fig. A.4). The lens model shows that the Einstein radius of the foreground lens is very extended compared to the observed emission, which could be due to overlapping mass profiles from the neighboring galaxies. However, additional mass profiles has little effect on the derived source morphology so here we present the simplest best-fit model using a single mass component. There is significant under-subtraction in the eastern counter-image, which is not reproduced even when multiple components are used, which could be due to substructure being present in the source plane. It is also unlikely that the residual emission northeast of the foreground lens is associated with the background galaxy since the lens model also fails to reproduce any counter-images in this region.

HBoötes02 (Grade A1): The lens model for the sub-mm emission was discussed in

Bussmann et al. (2013). A multi-wavelength analysis for this object will be featured in Wardlow et al. 2014 (in prep.). The K_s -band image shows an edge-on disk galaxy with an incomplete quad configuration, accompanied by faint, extended emission between the counter-images. The WFC3 F110W image shows no detections of the background source, while the detection in the NIRC2 H -band is marginal.

To model the background source, we consider both a one component point-source (circular Gaussian profile) and a two component model with a point-source and an extended Sérsic profile. The one component fit yields a $\chi^2_\nu = 1.42$ and reproduces all the observed features. However, the converged solution predicts the fourth undetected counter-image in the data to be detected at 10σ in the model. One possible explanation favoring this model would be severe obscuration from the edge-on disk. However, there is also EVLA radio observations of this system (Wardlow et al., 2013), which will not be affected by dust obscuration from the foreground lensing galaxy. In the EVLA data only the three near-IR luminous sources are detected, despite the sensitivity being high enough to detect the fourth image predicted by the single component model, if the flux ratios are as predicted. Therefore we consider it unlikely that the single component model is correct.

Furthermore, the two component model (shown in Fig. 3.4) has a marginally improved fit, with $\chi^2_\nu = 1.19$ and has a configuration in which the fourth faint counter-image is faint and expected to be undetected ($< 5\sigma$). This model also has some physical motivation, since the sub-mm data (Bussmann et al., 2013) shows an extended component, interpreted as star-forming regions, while the radio data (Wardlow et al., 2013) show a point source, indicative of an AGN. Both AGN and star-formation can be bright in the near-IR, which is supported by the faint extended emission in the observed frame K_s -band data.

The center of the foreground mass profile is significantly offset from the stellar light profile ($\sim 0.20''$ or 1.2 kpc), but this separation could be due to the dust-lane partially obscuring the true center of the stellar emission or the foreground galaxy not being perfectly edge-on.

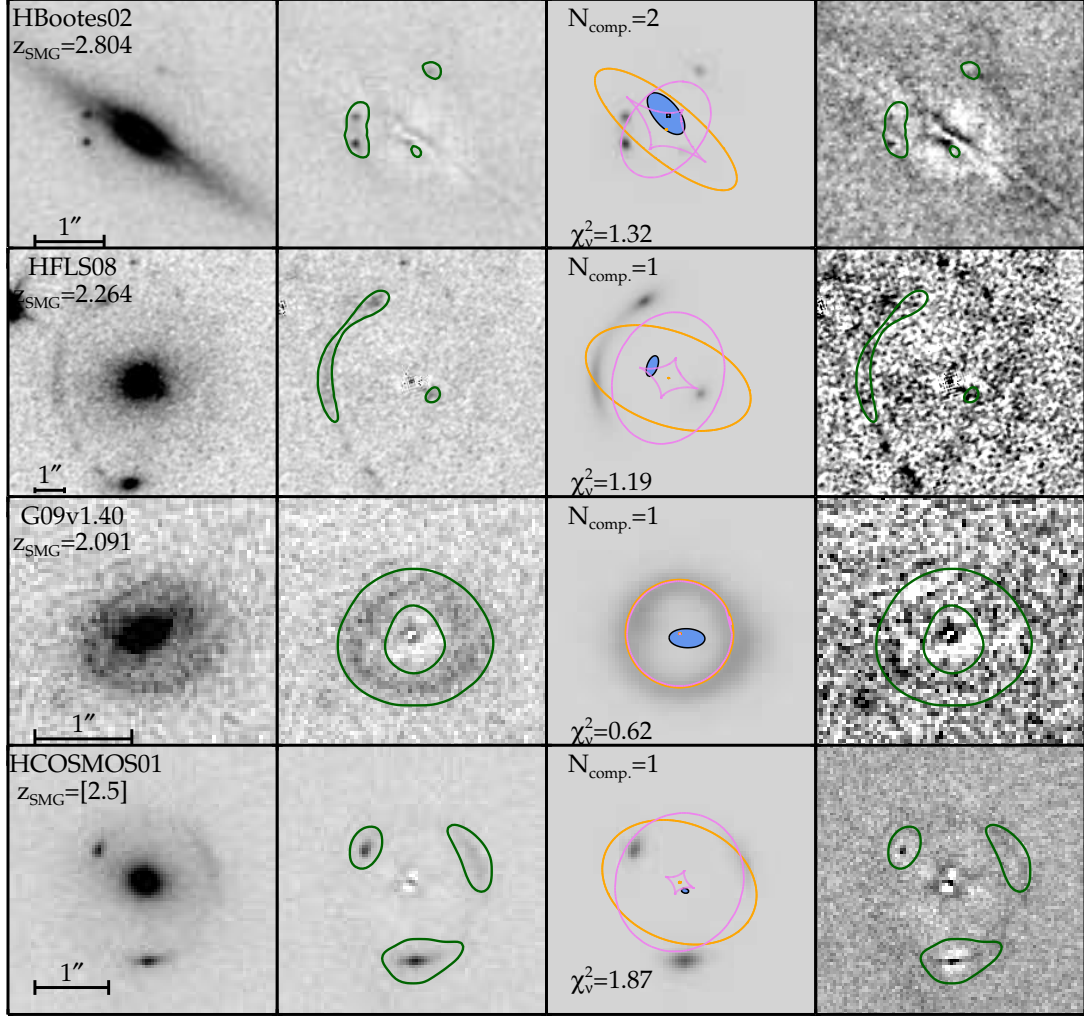


Figure 3.4 — continued.

The near-IR model also predicts a smaller Einstein radius ($0.56'' \pm 0.01$ vs. 0.77 ± 0.03) and magnification factor than the sub-mm lens model ($\mu_{\text{NIR}} = 5.3_{-0.4}^{+1.4}$ vs. $\mu_{880} = 10.3 \pm 1.7$).

HFLS08 (Grade A1): The *HST* image shows an arc-like morphology east of the foreground lens. A counter-image located south-west from the foreground lens centroid is also detected at $> 5\sigma$ after surface brightness profile subtraction. Since there are multiple regions of emission that could all potentially be associated with the arc, we use an initial fitting region that encloses all the suspected features for our preliminary models. We also tried models in which the background galaxy is described by multiple components, or a

two component mass profile. None of these solutions successfully account for the compact emission $\sim 3''$ south of the foreground lens. We are unable to produce a configuration that accounts for the faint regions northeast and southeast of the foreground lens shown in the residual image. Therefore, we consider it unlikely that these features are from the lensed galaxy. Spectroscopy is required to confirm whether all the emission is associated with the background SMG. Since a single background component provides the best fit to the lensed arc, that is the model that we retain, and that is presented in Fig. 3.4.

NB.v1.43 (Grade A1): This object was presented in Bussmann et al. (2013) and George et al. (2013) and will be further analyzed in Fu et al. (in prep.). This object could potentially be lensed by a cluster, as discussed in Bussmann et al. (2013). The K_s -band and H -band images (Fig A.4) show a much more elongated morphology than the sub-mm data, but there is little curvature. The lack of additional counter-images and a central position for the lensing mass places very weak constraints on the configuration, so we do not provide a lens model for this source.

G09v1.40 (Grade A2): The lens model for the $880 \mu\text{m}$ emission for this source was presented in Bussmann et al. (2013). The near-IR model for the background galaxy is a highly elongated, extended object with $a_{\text{eff}} = 0.18$, which is roughly three times the size of the sub-mm model. In the near-IR, the background galaxy is nearly in perfect alignment with the foreground lens, producing the observed Einstein ring. This configuration shows a slight contrast with the sub-mm data, which show two peaks in the emission which could represent a double configuration, as supported by their lens model. However, the near-IR magnification $\mu_{\text{NIR}} = 11.4_{-1.0}^{+0.9}$ is consistent with the SMA data, ($\mu_{880} = 15.3 \pm 3.5$), which suggests that the lensing configurations are similar and the two peaks seen in the SMA map are likely a result of having poor spatial resolution compared to Keck AO.

HCOSMOS01 (Grade A3): The K_s -band image shows an incomplete Einstein ring in which three well-separated arcs are visible. The F110W image (Fig. A.4) shows a consistent configuration but appears to be fainter. Only one component is required to reproduce the observations and using multiple components results in only a marginal improvement in the fit. The wide range of magnifications ($\mu_{\text{NIR}} = 9_{-2}^{+5}$), is due to the compact size of the background galaxy ($a_{\text{eff}} \sim 0.04''$) and its location relative to the caustics. The residual image shows areas of under and over subtraction, also reflected by a relatively worse fit $\chi_{\nu}^2 = 1.86$, indicating that the Sérsic profile could be an over-simplified model to describe the background SMG.

HLock04 (Grade A3): The double arc lensing morphology of HLock04 is detected in both the near-IR and sub-mm, which makes it ideal for multi-wavelength studies. This morphology is consistent in the J , H , and K_s , but is brightest at the K_s -band, shown in Fig. A.4. We calculate a slightly higher magnification factor of $\mu_{\text{NIR}} = 8.1_{-0.3}^{+0.2}$ compared to $\mu_{\text{NIR}} = 6.17 \pm 0.03$ from Wardlow et al. (2013), but is consistent in the sub-mm ($\mu_{880} = 7.1 \pm 1.5$ Bussmann et al., 2013). This is likely due to the background galaxy being located outside, near the central caustic, which is a region with a steep magnification gradient (Hezaveh et al., 2012). A slight positional offset between the two lens models could then cause a significant change in magnification value.

HFLS02 (Grade A3): This object was included in the supplementary sample of Wardlow et al. (2013). The *HST* imaging shows an asymmetric Einstein ring lens morphology that suffers blending with the foreground lens. The residual image shows areas of under-subtraction, which could be either due to the presence of substructure in the source plane or left-over emission from the foreground lens. This is also a rare case in which the background source has a larger angular size than the foreground lens.

HECDFS05 (Grade A4): Subtracting the foreground lens emission reveals a counter-

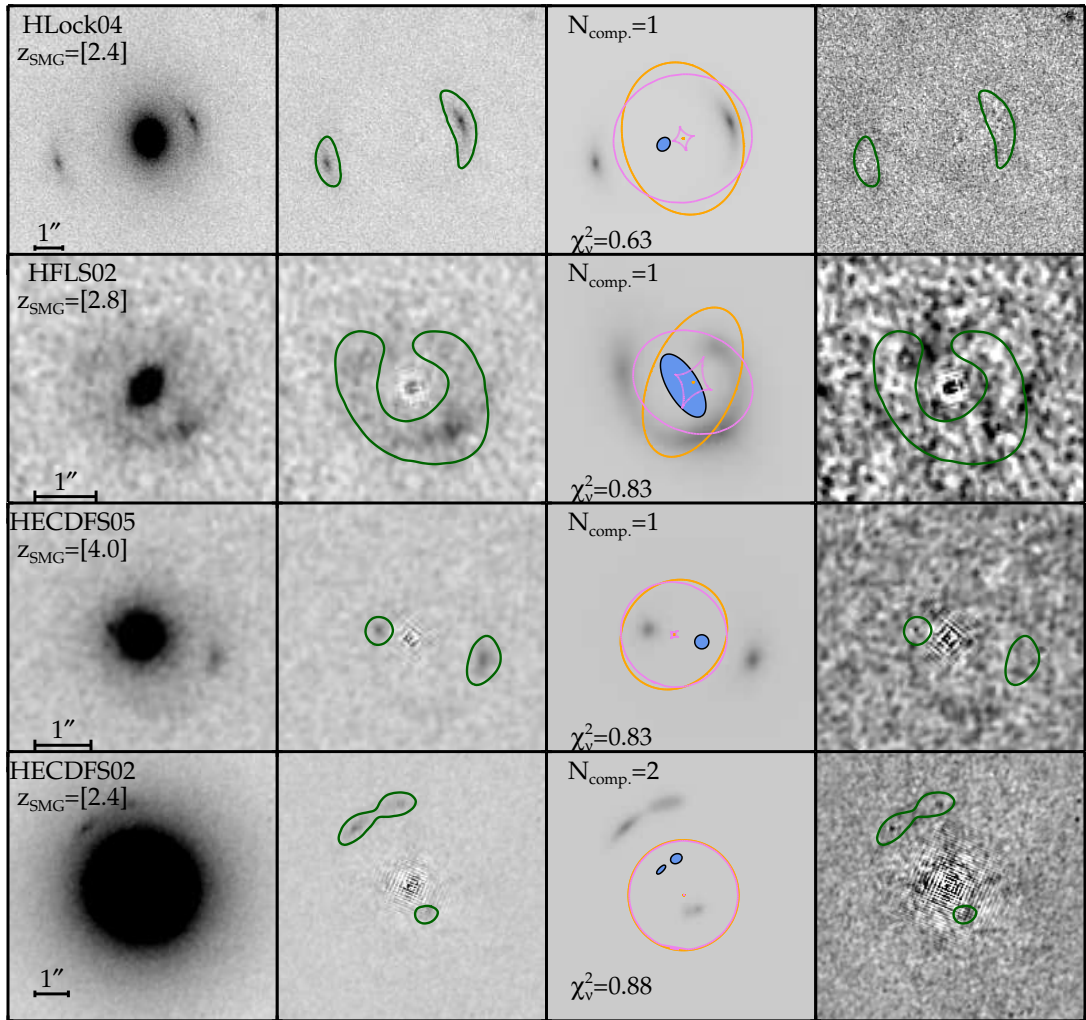


Figure 3.4 — continued.

image ($> 7\sigma$) east of the foreground lens, exhibiting a double configuration. The residual image shows an under-subtracted region to the south of the foreground lens, which could be an arc. However, the low signal to noise feature is not reproduced in the lens modeling and may not be part of the lensed SMG. The source plane reconstruction shows a strongly magnified ($\mu_{\text{NIR}} = 4.0_{-0.7}^{+0.8}$), compact ($a_{\text{eff}} = 0.11 \pm 0.01$), spherical ($\epsilon_s \sim 0$) galaxy.

HECDFS02 (Grade A4): This source was discussed in Wardlow et al. (2013) and we present an updated lens model in this paper. The *HST* image shows an arc with two knots north-east of the foreground lens. We detect a counter-image at $> 10\sigma$ after subtracting the foreground lens. The best-fit lens model contains two background sources of similar size ($\sim 0.15''$), with their centroids separated by $\sim 0.4''$. The SPIRE colors suggest a redshift of 2.4, which corresponds to two ~ 1 kpc objects separated by ~ 3 kpc. Both background sources are distorted by the lensing galaxy to produce a double configuration in the image plane, where the fainter counter-image of both sources are in the same region and blended in our data. Leaving the ellipticity as a free parameter in the two-component model consistently caused it to converge to zero ($\epsilon = 0$ corresponds to circular symmetry), which is the lower limit, so we fix this parameter to this value in our best-fit model. The background source is reminiscent of merger-like systems presented in figure 2 of Chapman et al. (2003). A single-component model gives a slightly worse fit ($\chi^2_{\nu} = 1.2$), which yields a mass profile that is significantly elongated ($\epsilon \sim 0.6$) in contrast to the rounder light profile ($\epsilon \sim 0.1$) and a cusp configuration similar to HFLS08.

Table 3.2: Properties of the Foreground Lenses of Grade 1 Systems⁴

Name	b	δx	δy	ϵ	θ	χ^2/N_{DOF}
	"	"	"		°	
NB.v1.78	$0.944^{+0.002}_{-0.001}$	$0.018^{+0.001}_{-0.003}$	$-0.042^{+0.003}_{-0.001}$	$0.419^{+0.002}_{-0.007}$	$80.9^{+0.2}_{-0.2}$	1455/1897
G15v2.19	$0.738^{+0.002}_{-0.001}$	$0.027^{+0.002}_{-0.002}$	$0.044^{+0.002}_{-0.003}$	$0.208^{+0.005}_{-0.003}$	$-51.0^{+0.5}_{-0.4}$	5452/2097
HLock12	$1.14^{+0.04}_{-0.07}$	$-0.15^{+0.06}_{-0.04}$	$-0.05^{+0.03}_{-0.05}$	$0.41^{+0.05}_{-0.08}$	132^{+7}_{-12}	2641/2871
HLock06	$2.46^{+0.01}_{-0.01}$	$-0.14^{+0.03}_{-0.01}$	$-0.14^{+0.01}_{-0.03}$	$0.067^{+0.02}_{-0.005}$	94^{+2}_{-4}	415/ 656
HBoötes02	$0.56^{+0.01}_{-0.01}$	$-0.201^{+0.005}_{-0.01}$	$0.084^{+0.005}_{-0.005}$	$0.68^{+0.01}_{-0.01}$	$50.7^{+0.3}_{-0.5}$	227/172
HFLS08	$1.95^{+0.05}_{-0.04}$	$-0.42^{+0.05}_{-0.07}$	$-0.38^{+0.07}_{-0.05}$	$0.46^{+0.04}_{-0.04}$	-110^{+2}_{-1}	1630/1364
G09v1.40	$0.56^{+0.01}_{-0.02}$	$0.0034^{+0.01}_{-0.001}$	$-0.01^{+0.01}_{-0.02}$	$0.0^{+0.1}_{-0.2}$	-57^{+4}_{-1}	544/874
HCOSMOS01	$0.91^{+0.01}_{-0.01}$	$-0.00^{+0.01}_{-0.02}$	$-0.01^{+0.02}_{-0.02}$	$0.26^{+0.04}_{-0.03}$	67^{+2}_{-1}	1182/633
HLock04	$2.403^{+0.01}_{-0.005}$	$0.080^{+0.001}_{-0.02}$	$-0.092^{+0.013}_{-0.003}$	$0.22^{+0.01}_{-0.02}$	14^{+1}_{-1}	1268/2013
HFLS02	$0.87^{+0.020}_{-0.05}$	$0.21^{+0.06}_{-0.01}$	$-0.01^{+0.04}_{-0.04}$	$0.46^{+0.04}_{-0.04}$	-23^{+4}_{-3}	1644/1981
HECDFS05	$0.96^{+0.02}_{-0.03}$	$-0.11^{+0.02}_{-0.02}$	$-0.10^{+0.02}_{-0.02}$	$0.12^{+0.01}_{-0.01}$	-38^{+11}_{-11}	305/369
HECDFS02 ^α	$1.6477^{+0.03}_{-0.05}$	$0.09^{+0.01}_{-0.02}$	$-0.10^{+0.01}_{-0.03}$	[0.0]	[0.0]	860/983

⁴**Notes**—The following parameters discussed in Section 3.4.1 are used to describe the foreground lens: b = Einstein radius, $(\delta x, \delta y)$ = centroid position of mass relative to light, ϵ = elongation, θ = orientation of mass profile (east of north), $\chi^2/N_{\text{DOF}} = \chi^2$ value and the number of degrees of freedom.

^α – The ellipticity and position angle is fixed to assume a circular shape, since the best fit for the foreground lens converges to this lower limit if left as free parameters.

Table 3.3: Properties of the Background Lensed Galaxy for Grade 1 Systems.⁵

Name	Flux Ratio	δu (")	δv (")	ϵ_s	θ_s (deg)	a_{eff} (")	n	μ_{NIR}
NB.v1.78	...	$0.11^{+0.01}_{-0.01}$	$0.19^{+0.01}_{-0.01}$	$0.01^{+0.04}_{-0.02}$	-13^{+14}_{-13}	$0.188^{+0.01}_{-0.002}$	$0.37^{+0.07}_{-0.03}$	$10.8^{+0.3}_{-0.2}$
...	$0.22^{+0.01}_{-0.02}$	$0.017^{+0.002}_{-0.004}$	$0.211^{+0.004}_{-0.002}$	$0.015^{+0.036}_{-0.003}$	24^{+24}_{-22}	$0.0220^{+0.0019}_{-0.0006}$	$0.99^{+0.11}_{-0.06}$...
HLock12	...	$0.6^{+0.1}_{-0.1}$	$0.31^{+0.04}_{-0.1}$	$0.06^{+0.1}_{-0.02}$	-0.1^{+50}_{-10}	$0.9^{+0.2}_{-0.1}$	$2.6^{+0.4}_{-0.4}$	$4.0^{+0.4}_{-0.4}$
HLock06	...	$0.75^{+0.03}_{-0.02}$	$0.78^{+0.02}_{-0.04}$	$0.50^{+0.03}_{-0.1}$	114^{+4}_{-1}	$0.30^{+0.01}_{-0.02}$	$2.5^{+0.3}_{-0.2}$	$6.9^{+0.4}_{-0.3}$
G15v2.19	...	$0.161^{+0.003}_{-0.003}$	$0.013^{+0.003}_{-0.004}$	$0.80^{+0.01}_{-0.02}$	-136^{+2}_{-1}	$0.031^{+0.001}_{-0.002}$	$0.34^{+0.06}_{-0.03}$	$9.6^{+1}_{-0.3}$
...	$0.24^{+0.05}_{-0.02}$	$0.062^{+0.003}_{-0.004}$	$0.025^{+0.003}_{-0.01}$	$0.4^{+0.04}_{-0.1}$	1^{+17}_{-7}	$0.028^{+0.002}_{-0.002}$	$0.15^{+0.1}_{-0.01}$...
...	$1.8^{+0.2}_{-0.1}$	$0.108^{+0.01}_{-0.01}$	$0.037^{+0.01}_{-0.004}$	$0.51^{+0.03}_{-0.02}$	-11^{+2}_{-1}	$0.18^{+0.01}_{-0.01}$	$0.34^{+0.1}_{-0.02}$...
HBoötes02 ⁶	...	$0.04^{+0.01}_{-0.01}$	$0.20^{+0.01}_{-0.01}$	[0.0]	[0.0]	$0.013^{+0.001}_{-0.001}$	[0.5]	$5.3^{+1.4}_{-0.4}$
...	$1.7^{+0.4}_{-0.3}$	$0.00^{+0.01}_{-0.01}$	$0.23^{+0.01}_{-0.02}$	$0.5^{+0.1}_{-0.1}$	40^{+3}_{-1}	$0.35^{+0.03}_{-0.03}$	$2.0^{+0.4}_{-0.4}$...
HFLS08	...	$0.5^{+0.1}_{-0.1}$	$0.6^{+0.1}_{-0.1}$	$0.6^{+0.1}_{-0.2}$	-19^{+30}_{-19}	$0.34^{+0.01}_{-0.05}$	$2.6^{+0.4}_{-1}$	$7.7^{+1.6}_{-0.7}$
G09v1.40	...	$0.08^{+0.01}_{-0.01}$	$0.05^{+0.01}_{-0.03}$	$0.49^{+0.02}_{-0.06}$	87^{+6}_{-4}	$0.18^{+0.01}_{-0.01}$	$0.51^{+0.02}_{-0.04}$	$11.4^{+0.9}_{-1}$
HCOSMOS01	...	$0.08^{+0.02}_{-0.02}$	$0.12^{+0.02}_{-0.02}$	$0.4^{+0.1}_{-0.1}$	76^{+25}_{-24}	$0.037^{+0.005}_{-0.005}$	$1.0^{+0.7}_{-0.2}$	9^{+5}_{-2}
HLock04	...	$0.69^{+0.01}_{-0.02}$	$0.714^{+0.02}_{-0.003}$	$0.22^{+0.02}_{-0.01}$	$-40.0^{+0.1}_{-0.1}$	$0.24^{+0.01}_{-0.01}$	$2.0^{+0.1}_{-0.2}$	$8.1^{+0.2}_{-0.3}$
HFLS02	...	$0.16^{+0.1}_{-0.02}$	$0.04^{+0.04}_{-0.05}$	$0.58^{+0.03}_{-0.1}$	-148^{+9}_{-6}	$0.57^{+0.01}_{-0.1}$	$1.7^{+0.2}_{-0.3}$	$7.4^{+0.5}_{-0.6}$
HECDFS05	...	$0.50^{+0.03}_{-0.03}$	$0.47^{+0.03}_{-0.03}$	$0.0018^{+0.0003}_{-0.0003}$	-168^{+4}_{-4}	$0.11^{+0.01}_{-0.01}$	$3.9^{+1.1}_{-0.5}$	$4.0^{+0.8}_{-0.7}$
HECDFS02	...	$0.68^{+0.02}_{-0.05}$	$0.02^{+0.03}_{-0.09}$	$0.7^{+0.1}_{-0.2}$	-49^{+23}_{-19}	$0.15^{+0.03}_{-0.02}$	$0.7^{+0.9}_{-0.2}$	$3.1^{+0.2}_{-0.3}$
...	$0.7^{+0.1}_{-0.1}$	$0.25^{+0.04}_{-0.06}$	$0.56^{+0.03}_{-0.1}$	$0.001^{+0.2}_{-0.001}$	-18^{+17}_{-38}	$0.15^{+0.03}_{-0.02}$	$0.110^{+0.4}_{-0.003}$...

⁵**Notes**—The following parameters discussed in Section 3.4.1 are used to describe the background source: Flux Ratio = ratio of integrated flux, relative to the first listed component (fixed in the case of single components), $(\delta u, \delta v)$ = background source position, relative to the the centroid of the mass profile, ϵ_s = elongation of the background source, θ_s = orientation of the background source (east of north), a_{eff} = effective semi-major axis, n = Sérsic index, μ_{NIR} = near-IR magnification factor (represents the total value, with all subcomponents included).

⁶Background component assumes a gaussian point source.

3.5 Results and Discussion

3.5.1 Differential Lensing and Source Sizes

Differential lensing is caused by spatially offset regions of the background galaxy, which, if they have different colors or SEDs, effectively corresponds to different wavelength regimes. This effect is more pronounced in galaxy-galaxy lensing than cluster lenses because of the steeper gradients of the magnification factors mapped onto the source plane. Recent simulations predict the effect of differential lensing in galaxy-galaxy SMG systems (Hezaveh et al., 2012; Serjeant, 2012), but few observations studies have successfully measured it (Gavazzi et al., 2011; Fu et al., 2012; Dye et al., 2014). In order to measure the effects of differential lensing, a consistent mass profile to describe the foreground galaxy must be applied on lens modeling multi-wavelength data sets of the same background source. Here, we search for evidence of differential lensing by comparing the sub-millimeter lens models (from Bussmann et al. 2013) with our near-IR lens models. Figure 3.5 compares μ_{NIR} with μ_{880} for the systems in our sample that are also in Bussmann et al. (2013), where we show both our best-fit near-IR magnifications, and the values calculated using the same foreground lens parameters from sub-mm data. To verify that the difference in lens modeling methods between the near-IR and the sub-mm is not a dominant source of error, we also model sub-mm data from Bussmann et al. (2013) and are able to recover consistent magnifications values. The results of applying sub-mm foreground lens parameters on near-IR data are summarized in Fig. 3.5 and Table A.3. For comparison, we also show the lensed SMGs with both near-IR and sub-mm magnification measurements from Dye et al. (2014), Fu et al. (2012), Gavazzi et al. (2011), and Bussmann et al. (2013)⁷. Our overlapping sample has $\mu_{\text{NIR}} < \mu_{880}$, in most

⁷Differential magnification for G12v2.30 was measured in Fu et al. (2012) by applying the near-IR foreground lens parameters in the sub-mm. However, we note that an updated model for this source was discussed (Bussmann et al., 2013), due to additional SMA EXT data. The studies of SDP lenses featured in Dye et al. (2014), HLock01 in Gavazzi et al. (2011), and Bussmann et al. (2013) use independent foreground lens parameters.

cases, with $\mu_{880}/\mu_{\text{NIR}} \sim 1.5$ on average, providing observational evidence of differential lensing 500- μm selected galaxies. Therefore, in cases where magnification factors can only be measured in one regime, caution should be used when interpreting physical quantities at other wavelengths. However, it is also important to note that the measurement uncertainties are often greater than the average effect of differential magnification (e.g. stellar masses have systematic uncertainties from 2-5 Michałowski et al., 2010; Wardlow et al., 2011; Michałowski et al., 2012a; Targett et al., 2013; Simpson et al., 2013).

Lensing magnification values are generally negatively correlated to intrinsic sizes of the lensed background source. Therefore, Fig. 3.5 suggests that the near-IR emission regions in lensed SMGs are larger than sub-mm emission regions in the source plane. Physically, this could imply that the lensed dusty star-forming regions have clumpier morphologies than the older stellar distribution. We further explore this, by showing in Fig. 3.6 the circularized effective radius ($r_{\text{eff}} = \sqrt{a_{\text{eff}}b_{\text{eff}}}$) of the most extended background component in our near-IR models compared with the sub-mm emission. Indeed, in most cases the dust emission does appear to originate from a smaller region than the stellar light (as proxied by the observed frame near-IR data).

It is difficult to assess whether the disagreement at larger values of $r_{\text{eff},880}$ is generally true for lensed SMGs. Lensed sources that are intrinsically extended in the sub-mm are also less magnified, which means a lower probability for detection in near-IR observations. HLock04 is the only source from our analysis with a larger measured intrinsic size in the near-IR relative to the sub-mm, which could be due to the uncertainty in the observed sub-mm lensing configuration as discussed in the Appendix. The results of Fig. 3.5 and 3.6 could be a direct consequence of the bias that exists in selecting lensing events in the sub-mm. Simulations predict that detections of sub-mm selected gravitationally lensed galaxies are subject to an angular size bias towards the most compact emission regions that are both comparable to the size of, and near the source-plane caustics (Hezaveh et al., 2012; Serjeant,

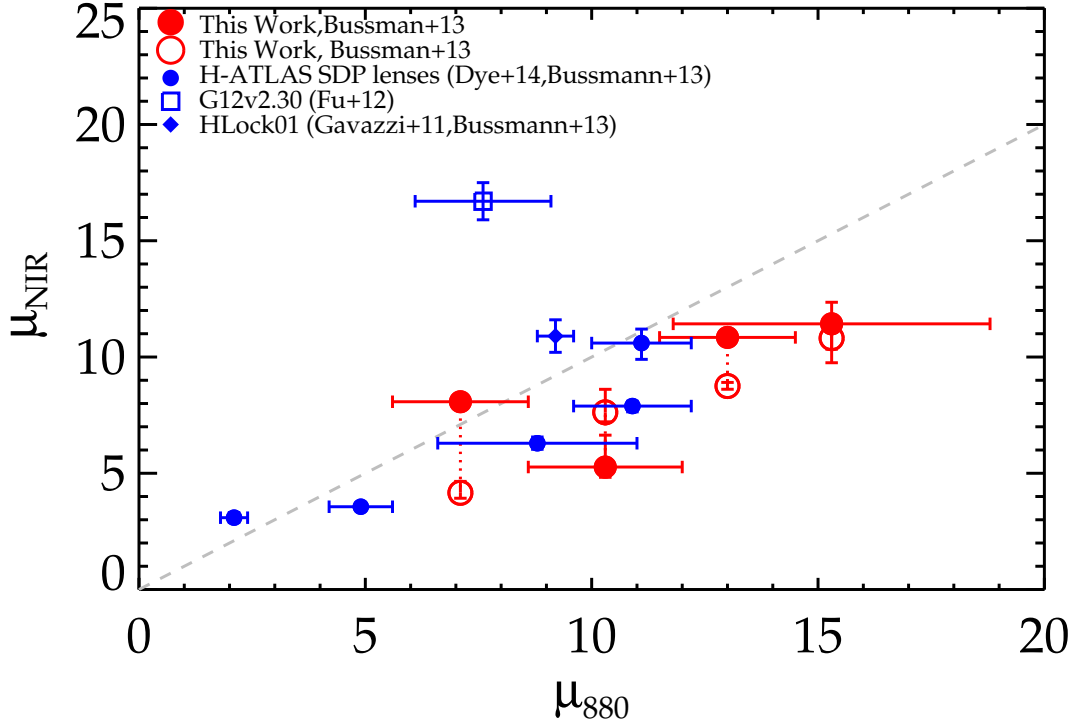


Figure 3.5: Comparison of near-IR and sub-mm magnifications

Filled symbols are magnification values from independent near-IR and sub-mm lensing analyses. Open symbols denote best-fit lens models using consistent foreground lens parameters in the near-IR and sub-mm. For our work, we fix sub-mm lens parameters from Bussmann et al. (2013) to our near-IR data. The blue circles, diamonds and square are near-IR data points from Dye et al. (2014); Gavazzi et al. (2011), and Fu et al. (2012), respectively, with the corresponding sub-mm magnifications from Bussmann et al. (2013), if available. The dashed line shows one-to-one correspondence between μ_{NIR} and μ_{880} . Most sources lie below this line, with $\mu_{\text{NIR}} < \mu_{880}$. Differential magnification is observed and is likely due to spatial variations or a morphological difference between the near-IR (stellar) and sub-mm (dust) emission.

2012; Lapi et al., 2012). The bias towards compact sub-mm sources translates to larger values of μ_{880} . However, this effect is reduced in the near-IR and hence contributes to the deviation from the one-to-one correspondence line in Fig. 3.5. If this bias has the same effect on sources that are less amplified, more extended sources in the sub-mm (Busmann et al., 2013), then its possible that our result in Fig. 3.6 could also hold true for larger values of $r_{\text{eff},880}$.

Spatially resolved radio and gas/dust continuum observations (Chapman et al., 2004; Biggs & Ivison, 2008; Ivison et al., 2008; Tacconi et al., 2008; Engel et al., 2010) of SMGs have measured the emission due to star-formation to be as extended as ~ 10 kpc. This is also in agreement with high-resolution sub-mm observations (Younger et al., 2008, 2009; Hodge et al., 2013). While in the near-IR regime, SMGs have a typical size range of 2 – 4 kpc (Swinbank et al., 2010; Targett et al., 2011, 2013; Aguirre et al., 2013). For our sample of lensed SMGs that overlap in the near-IR and sub-mm, we calculate a median intrinsic physical size of ~ 2 kpc in the near-IR, compared to ~ 1 kpc in the sub-mm (Busmann et al., 2013). These results are in contrast to the larger values of the previous findings but could also be demonstrating one of the main drawbacks of galaxy-scale lenses. The area of high magnification in galaxy-scale lenses is smaller compared to cluster-scale lenses, so it is entirely possible that only a sub-region of the total emission in both near-IR and the sub-mm is being amplified and detected. Future high-resolution sub-mm observations using the full capabilities of the Atacama Large Millimeter Array (ALMA) with sub-arcsecond spatial resolutions (0.10-0.4") will be able to confirm this by measuring the sizes of star-forming clumps in unlensed SMGs.

Figures 3.5 and 3.6 also give a measure of the variation of μ_{NIR} and a_{eff} from performing lens models independently (i.e. without using 880 μm parameters). On average, using 880 μm foreground lens parameters to derive magnification factors and intrinsic sizes are in agreement relative to our independent analysis to within $\sim 30\%$. Less deviation is observed in the magnification measurements when the lensing morphology provide strong constraints and

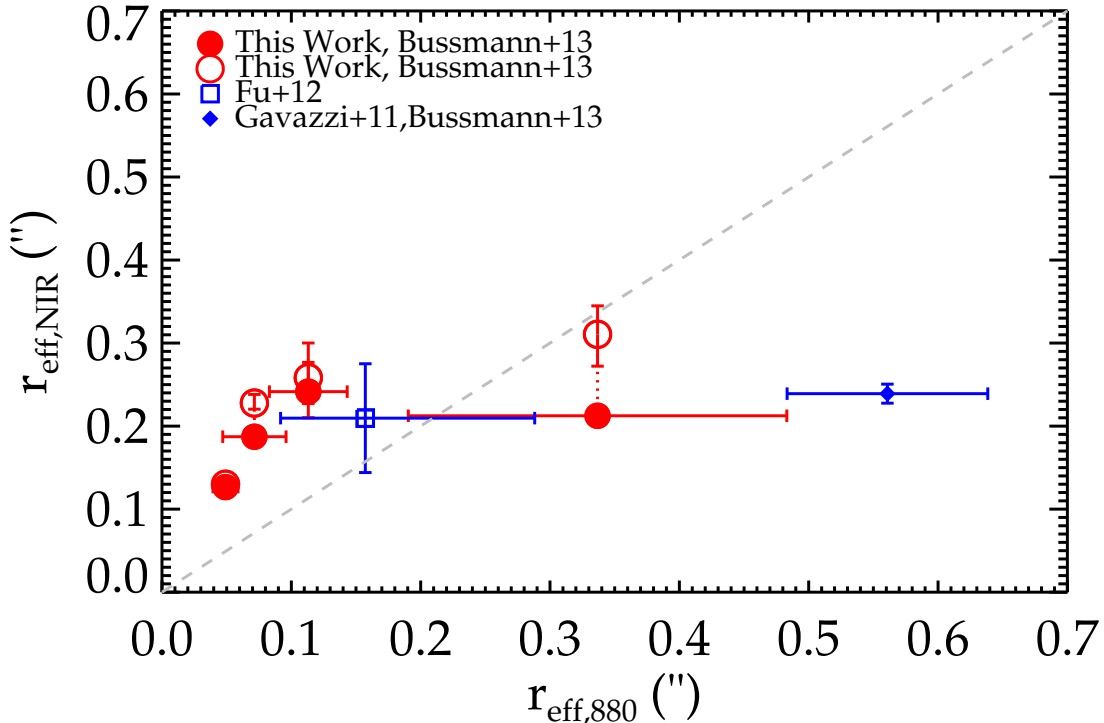


Figure 3.6: Intrinsic sizes of SMGs in the near-IR and sub-mm.

Open symbols denote consistent foreground lens parameters between the near-IR and sub-mm. Here, the foreground lens parameters are fixed to those derived from the sub-mm (Bussmann et al., 2013). Most of the SMGs lie above the line of 1-to-1 correspondence (dashed line), showing that their dust emission is typically more extended than the rest-frame optical (likely stellar) emission. This is consistent with the observed differential magnification (Fig. 3.5), and suggests that smaller emission regions are usually more highly magnified.

show similar configurations in both the sub-mm and near-IR.

The analysis of *Herschel*-selected SMGs in Bussmann et al. (2013) confirmed the angular size bias present in sub-mm selected lensing systems. We investigate whether this bias also affects near-IR observations of lensed SMGs in Fig. 3.7, where we show the observed near-IR magnification factors against the intrinsic size of the lensed galaxy. For objects with multiple components, we use the one with the largest angular size. We find a hint of negative correlation between magnification factors and size, albeit with large scatter, but consistent with simulations and sub-mm observations.

In Fig. 3.7 we also highlight sizes of $0.24'' - 0.48''$, which corresponds to 2-4 kpc at $z = 2.5$, the range measured for the observed-frame near-IR median sizes of $850 \mu\text{m}$ selected unlensed SMGs (Chapman et al., 2003; Swinbank et al., 2010; Aguirre et al., 2013; Targett et al., 2013). Few of our targets are more extended than this, and most are smaller than $0.24''$. If $500 \mu\text{m}$ selected lensed SMGs are evolutionarily similar to unlensed 850 or $880 \mu\text{m}$ -selected galaxies (as is likely, since the sample from Bussmann et al. (2013) have $S_{880} \geq 4$ mJy, when corrected for magnification, comparable to the classical SMG selection. Also, see Section 3.5.3 for a discussion), then it appears that the lensed galaxies are preferentially those with the smallest near-IR emission regions. Thus, it appears that the sub-mm selection method, which is biased towards the highest sub-mm fluxes, and therefore highest sub-mm magnifications and smallest intrinsic sub-mm emission region (Bussmann et al., 2013) also selects the galaxies with the most intrinsically compact near-IR emission regions. This follows from Fig. 3.5, which shows a correlation between μ_{NIR} and μ_{880} .

In our sample of lensed SMGs, we calculate a median intrinsic size of 2.3 kpc for sources with secure redshifts and if we include sources with photometric redshifts derived from SPIRE colors (Grade A3 and A4 sources), this number is reduced to 1.9 kpc. If we also assume that the photometric redshift subset have a redshift range of $z = 1 - 4$ (Chapman et al., 2005; Chapin et al., 2009; Wardlow et al., 2011; Michałowski et al., 2012b; Yun et al., 2012; Wardlow et al., 2013; Simpson et al., 2013; Umehata et al., 2014), the maximum angular size scale variation is $\sim 1.5 \text{ kpc arcsec}^{-1}$, which we use to constrain a minimum and a maximum median intrinsic size of 1.66 and 2.03 kpc for our whole sample. This difference is not significant, given the large uncertainties associated with photometric redshifts. These values are smaller than the median sizes previously found for $850 \mu\text{m}$ selected SMGs in the near-IR ($r_{\text{eff}} = 2.5 - 2.7$ kpc, Aguirre et al. 2013; $r_{\text{eff}} = 4.0$ kpc, Targett et al. 2013, $r_{\text{eff}} = 3.1$ kpc, Targett et al. 2011; $r_{\text{eff}} = 2.3 - 2.8$ kpc, Swinbank et al. 2010). Although the smaller measured intrinsic size could be due to the sub-mm size bias, our study of lensed SMGs is performed at spatial resolutions well above the observational limitations of the current near-

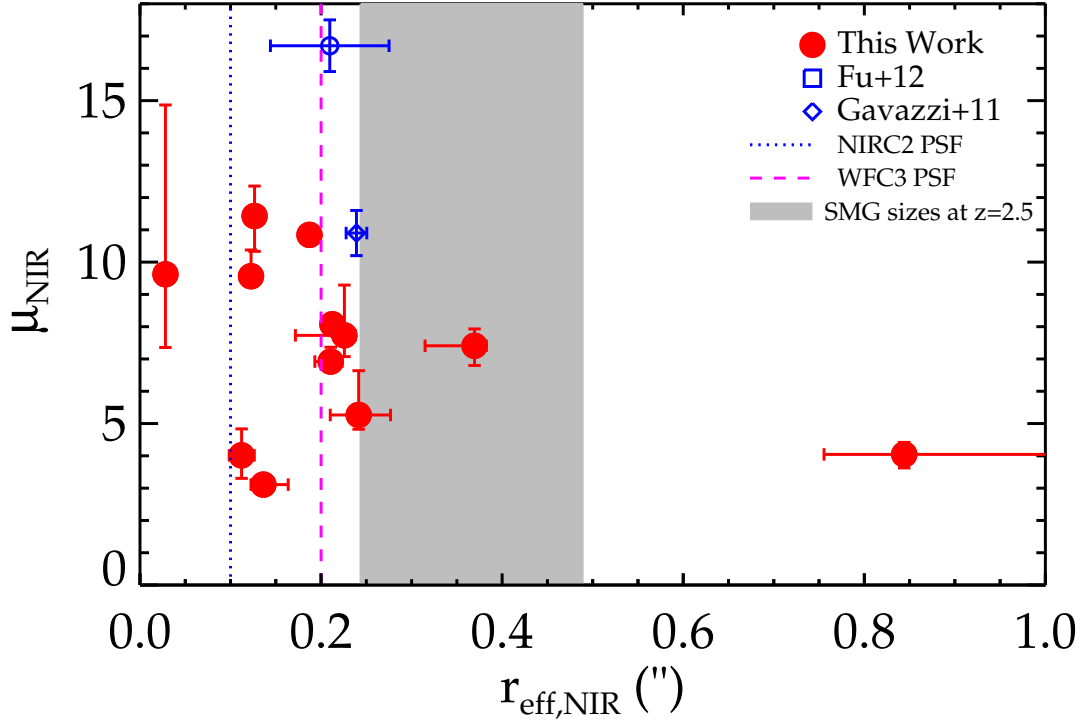


Figure 3.7: Near-IR magnifications and sizes for lensed SMGs.

For sources with multiple components, we plot the most extended component. Vertical dashed lines show typical spatial resolutions of our NIRC2-LGS/AO and *HST* F110W WFC3 data. The grey shaded region covers the range of 2–4 kpc for unlensed 880 μm -selected SMGs at $z = 2.5$, based on high resolution near-IR analyses of Swinbank et al. (2010); Targett et al. (2011, 2013), and Aguirre et al. (2013). A size bias for sub-mm selected lensing systems is observed in the near-IR, in which compact sources typically have larger magnifications. The near-IR emission for *Herschel*-selected lensed SMGs is generally more compact than previous size measurements of unlensed classical SMGs.

IR facilities. Therefore, if we are observing the total near-IR emission from the background source, it could represent the typical size scales for this galaxy population.

3.5.2 Morphological Comparison With Previous Near-IR Studies of SMGs

Previous studies of SMGs in the rest-frame optical have revealed a variety of morphologies. Aguirre et al. (2013) identified that five out of 10 SMGs from their sample observed with *HST*/WFC3's F110W and F160W band have multiple components. The stellar mass ratio calculations of these multi-component SMGs showed that they could be associated with major and minor mergers. In contrast, the same study found that some of their most massive SMGs are single-component systems and have morphologies that resemble hydrodynamic simulations of rapidly star-forming galaxies (Davé et al., 2010). In agreement with this picture are the near-IR observations of unlensed SMGs in Targett et al. (2011) and Targett et al. (2013), in which SMGs appeared to be compact star-forming disks and are simply extreme examples of normal star-forming galaxies at $z \sim 2.5$. Many factors can provide an explanation for this discrepancy: varying levels of dust-obscuration in the rest-frame optical that gives rise to distinct observed morphologies (Swinbank et al., 2010); SMGs or their substructure having intrinsic sizes that are either comparable or smaller than the measured seeing could cause them to appear smoothed; or SMGs could simply be a heterogeneous sample with different galaxy formation mechanisms.

The boost in both flux and spatial resolution from gravitational lensing should reduce some of the limiting factors present in previous studies, provided that there are no significant morphological differences between $500 \mu\text{m}$ -selected and $850 \mu\text{m}$ -selected SMGs. Indeed, this assumption is justified since Bussmann et al. (2013) shows that the majority of the $500 \mu\text{m}$ selected lensed SMG sample observed in $880 \mu\text{m}$ have magnification corrected flux densities

consistent with $S_{880} \geq 4$ mJy. Of the 12 systems with lens models featured here, four are best fit with multiple components in the source plane. In three of these systems (NB.v1.78, HBoötes02, G15v2.19) the rest-frame optical SMG consists of a smaller component embedded in a larger one. We note that these multiple component systems also place a lower limit on the size of substructure ($0.02'' \sim 0.2$ kpc at $z \geq 1$) found in lensed SMGs, which would otherwise not be readily detected with current instrumentation.

These compact components could be interpreted as SMGs hosting an optically-bright AGN, small regions of star-formation embedded in a larger galaxy, or the remnants of a merger. Our findings suggest that near-IR studies of unlensed SMGs described as single components could have complicated morphologies that are unresolved even when using instruments that offer the highest spatial resolution. The morphologies of the SMGs in Aguirre et al. (2013) could support this claim, given that all their single component SMGs are unlensed and four out of five with multiple components are lensed by a nearby cluster. We also note that HECDFS02 is similar to the SMGs shown in Chapman et al. (2003); however a more accurate redshift and velocity information for each individual component is needed to confirm if this source is indeed in the process of a major-merger.

The remaining eight gravitationally lensed galaxies in our Grade A sample are composed of a single component that dominates the surface brightness profile of the background source, consistent with the axisymmetric models in Targett et al. (2011, 2013); Aguirre et al. (2013) and simulated SMGs in Davé et al. (2010). We note that five systems have excess flux in the residual images, which could be due to some substructure in the background galaxy, although our data cannot robustly determine whether this, or substructure in the foreground lens is responsible. The median Sérsic index for the subset that are best fit with a single component is $n \sim 2.5$, a significant deviation from the disk-like morphologies in Targett et al. (2013) ($n \sim 1.5$) but comparable with the measured values from Swinbank et al. (2010) ($n \sim 2.0$). However, we note that the statistical uncertainties associated with the best-fit Sérsic indices,

which are on the level of 10 – 30% is likely underestimated since it does not account for the assumptions used in the lens modeling that can affect the morphology of the background source, such as the shape of the PSF or the assumed mass profile.

3.5.3 Rest-Frame Optical Photometry

Given the average redshift of our sample ($z \sim 2.5$) and the fact that half of the Grade A sources we present are only observed in a single near-IR band, it is impossible to derive well-constrained physical quantities (e.g., stellar masses) without making sweeping assumptions about the effects of dust extinction, different star-formation histories, and inferred mass-to-light ratios of the near-IR SED. Instead, we opt to report observable quantities to minimize sources of systematic uncertainty and aim to use this paper as a starting point for future studies once sufficient multi-wavelength data have been acquired. The rest-frame wavelength range in the observed J and K band of our Grade A candidate lensing systems with secure redshifts (Grade A1 and A2) corresponds to $\sim 0.3 - 0.6 \mu\text{m}$. We use SMG SED templates from Michałowski et al. (2010) and our measured magnification corrected photometry, listed in Table 3.4, to extrapolate the rest-frame B band ($\lambda = 0.450 \mu\text{m}$) flux density. To measure the uncertainty of our extrapolated B -band magnitudes, we perform the same calculation using the near-IR data from the H-ATLAS SDP sample in Negrello et al. (2014) and calculate the scatter between the values using our fitting method and from their best-fit SED. On average, we find that the extrapolated B -band values are in agreement within 0.2 mag and show this as part of the errors shown in Fig. 3.8 and 3.9. For sources with one near-IR band, we simply normalize the SEDs to the observed datapoint and quote the average redshifted B band flux density and the standard deviation as an additional source of error.

Table 3.4: Near-IR Photometry of Lensed SMGs ⁸

Name	F_{F110W} (μJy)	$\sigma_{F110W,\text{stat.}}$ (μJy)	$\sigma_{F110W,\text{tot.}}$ (μJy)	F_H (μJy)	$\sigma_{H,\text{stat.}}$ (μJy)	$\sigma_{H,\text{tot.}}$ (μJy)	F_{K_s} (μJy)	$\sigma_{K_s,\text{stat.}}$ (μJy)	$\sigma_{K_s,\text{tot.}}$ (μJy)
NB.v1.78	2.5	0.1	0.2	3.9	0.1	0.2
HLock12	3.5	0.4	0.7
HLock06	2.4	0.2	0.2
G15v2.19	14.17	2.5	2.5	12.4	1.0	1.7
HBoötes02	$< 0.12^9$	< 0.36	2.5	0.7	1.4
HFLS08	0.7	0.2	0.2
HCOSMOS01 ¹⁰	0.49	0.3	0.3	2.8	1.5	1.5
HLock04	0.5	0.1	0.1	3.0	0.5	0.5	6.1	0.2	0.5
HFLS02	1.0	0.1	0.2
HECDFS05	0.5	0.1	0.2
HECDFS02	0.9	0.1	0.2

⁸**Notes**— The following columns describe the near-IR photometry: F = measured flux density, corrected for magnification, $\sigma_{\text{stat}} = 1\sigma$ error due to statistical noise, which accounts for the error in the background and magnification, σ_{tot} = Total noise, which accounts for both systematic and statistical errors. Systematic errors are dominated by the zero-point derivations from UKIDSS flux calibrations.

⁹These values represent $3\sigma_{\text{tot}}$ limits.

¹⁰The measured errors for these sources are dominated by the error in their magnification values.

Figure 3.8 shows that the magnification-corrected B -band absolute magnitudes (M_B) for our lens Grade A1 and A2 sources are consistent with both $880\ \mu\text{m}$ and $500\ \mu\text{m}$ selected unlensed and lensed SMG samples (Simpson et al., 2013; Negrello et al., 2014; Aguirre et al., 2013), with our sample typically on the fainter end of the distribution. We obtain a similar result in Fig. 3.9 if we compare magnification corrected $500\ \mu\text{m}$ flux densities. For sources that have a lens model from Bussmann et al. (2013), we use the sub-mm magnification factors to correct for the observed S_{500} , otherwise we use the values from the near-IR lens modeling. Our sample typically has intrinsic $S_{500} \leq 20\ \text{mJy}$, which corresponds to the $\sim 3\sigma$ limit (confusion and instrumental noise) for unlensed SMGs (Swinbank et al., 2014). This result is likely due to the benefits of flux amplification from lensing, which allows fainter objects to be detected at a higher significance. Although we find that lensed SMGs are on average intrinsically fainter in the rest-frame optical and far-IR compared to the unlensed populations, they are consistent with the observed flux distribution. This adds further evidence that the lensed SMGs in this paper are lensed analogs of the unlensed population, consistent with the findings of Harris et al. (2012) and Bussmann et al. (2013).

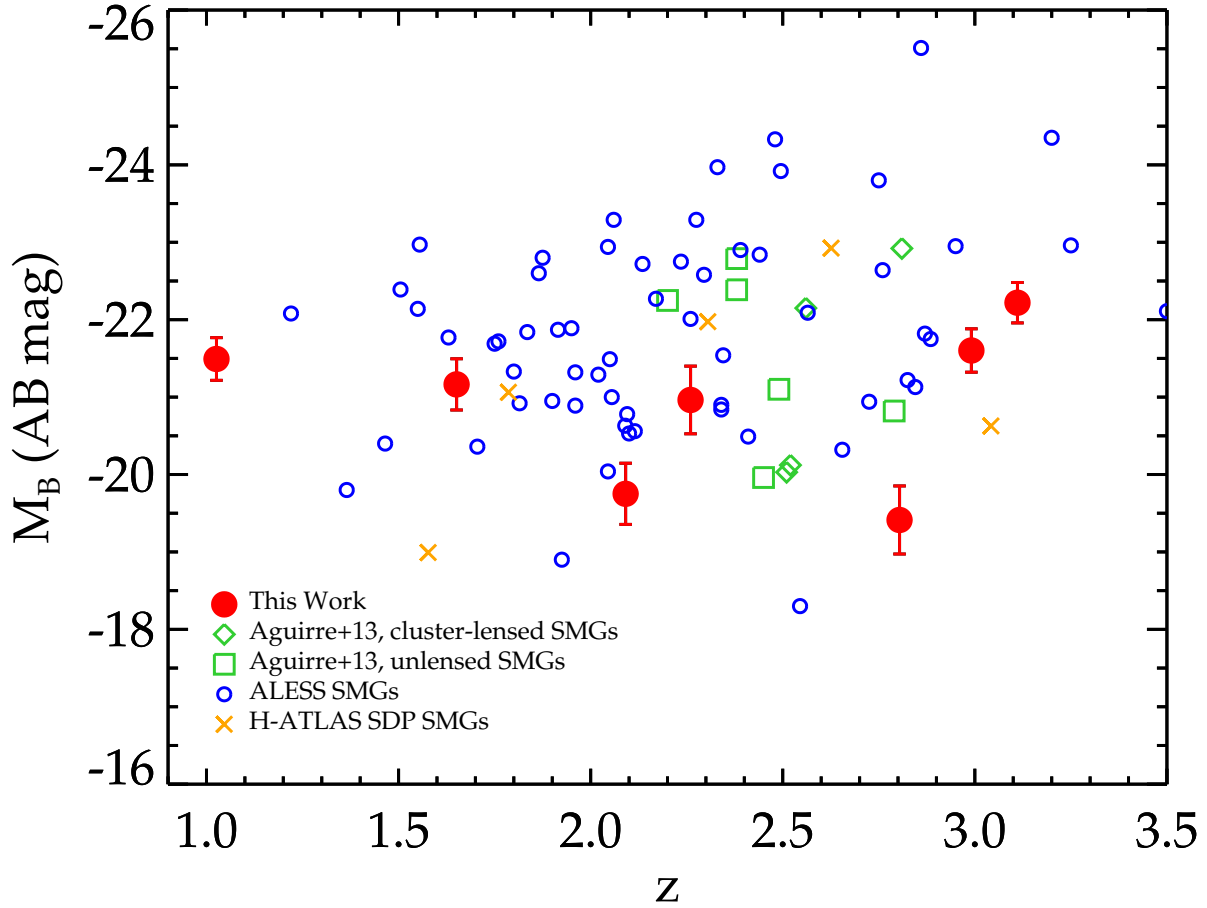


Figure 3.8: Intrinsic M_B and redshift.

Rest-frame magnification-corrected absolute B -band magnitudes (M_B) for Grade A1 and A2 candidates versus redshift. Open diamonds and squares represent cluster-lensed and unlensed SMGs from Aguirre et al. (2013), respectively. Open circles are unlensed ALESS SMGs from Simpson et al. (2013). The M_B values for lensed SMGs are consistent with unlensed SMGs at $z > 1$, but tend to lie towards the fainter end of the distribution.

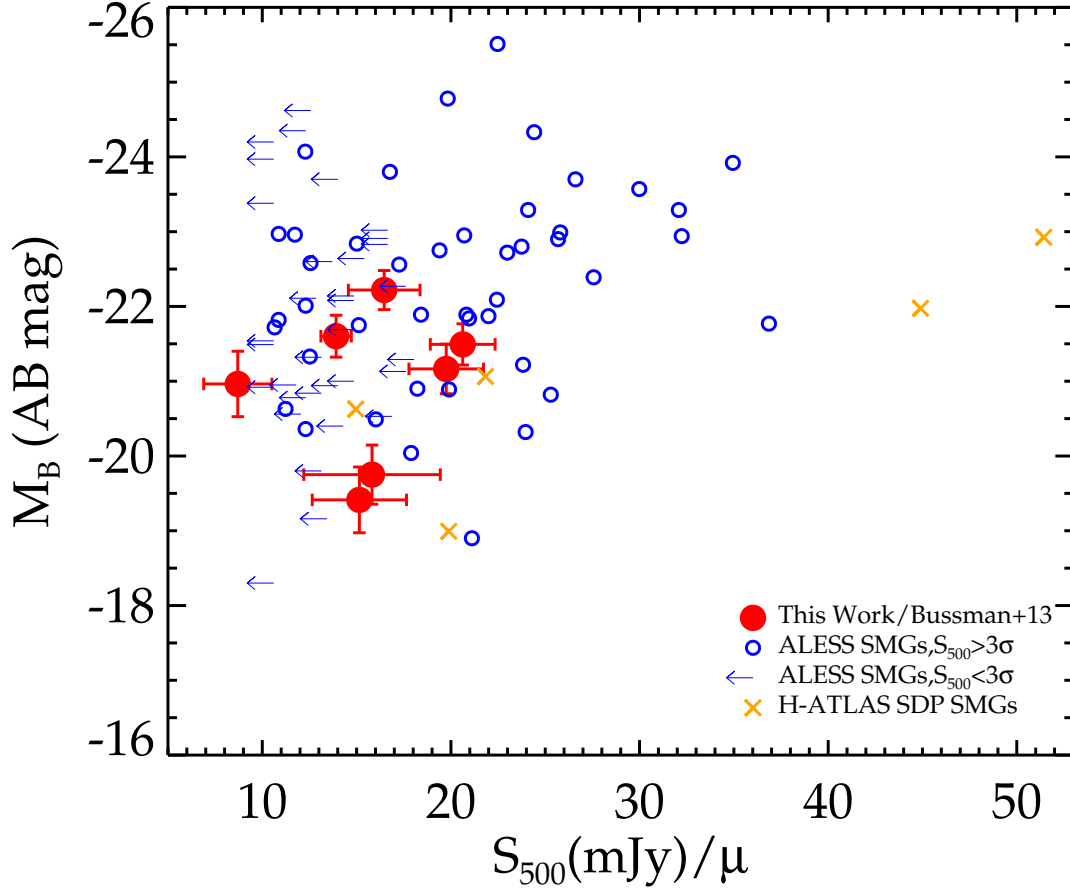


Figure 3.9: Intrinsic M_B and S_{500} for lensed SMGs.

Rest-frame magnification-corrected absolute B -band magnitudes (M_B) for Grade A1 and A2 candidates versus magnification corrected SPIRE S_{500} . We use the sub-mm magnification from Bussmann et al. (2013) when available to correct for the observed S_{500} . Open circles are unlensed ALESS SMGs from Swinbank et al. (2014) and Simpson et al. (2013). Our sample of lensed SMGs have consistent S_{500} values for a given M_B relative to the unlensed population, suggesting that *Herschel*-selected lensed SMGs are similar to classical unlensed $850\ \mu\text{m}$ -bright SMGs.

Chapter 4

HFLS3: A Massive Dust-Obscured Starburst at $z = 6.34$

4.1 Background

The unexpected discovery of HFLS3 (HerMES J170647.8+584623) at a redshift of 6.3369 ± 0.0009 in *Herschel* Space Observatory’s (Pilbratt et al., 2010) has led to the possibility that massive starbursting galaxies could be an appreciable contributor to the star-formation rate density of the Universe during the epoch of reionization (Riechers et al., 2013). The galaxy was first identified in the *Herschel* Multi-Tiered Extragalactic Survey (HerMES, Oliver et al. 2012) as a high-redshift candidate due to its “red” color in the SPIRE (Griffin et al., 2010) data, with $S_{500}/S_{350} \sim 1.45$ and $S_{500} \sim 47 \pm 3$ mJy. The redshift of HFLS3 was secured through the detection of more than 20 individual molecular and atomic lines at far-IR/sub-mm wavelengths with ground-based interferometers. HFLS3 was found to be luminous ($L_{\text{IR}} = (3.4 \pm 0.3) \times 10^{13} L_{\odot}$), gas-rich ($M_{\text{gas}} \sim 10^{11} M_{\odot}$) and dusty ($T_{\text{d}} = 49 \pm 2$ K). The instantaneous star-formation rate (SFR) implied by the above total IR luminosity (Kennicutt,

1998) is around $2900 M_{\odot} \text{ yr}^{-1}$ for a Chabrier (2003) initial mass function. It is also the highest redshift sub-mm galaxy (SMG) known to date, potentially probing the earliest formation epoch of dust in the Universe (for a recent review of SMGs and dusty star-forming galaxies in general see Casey, Narayanan, & Cooray, 2014).

One complication in interpreting the properties of HFLS3 is that it was found to be $\sim 0.5''$ to the South of a $z = 2.09$ galaxy (Figure 4.1), identified by Keck/NIRC2 K-band AO imaging and Keck/LRIS spectroscopy. This suggests some possibility that the flux density of HFLS3 is enhanced by gravitational lensing with a magnification factor, μ_{lens} . Due to the steepness of the SMG number counts and their high redshifts, and the corresponding high magnification bias, sub-mm surveys are known to be highly sensitive to gravitational lensing modifications (Blain, 1996; Perrotta et al., 2002; Negrello et al., 2007; Paciga et al., 2009). At the bright-end of the number counts at wavelengths longer than $350 \mu\text{m}$, lensed SMGs appear as a power-law distinct from the intrinsic counts (e.g., Negrello et al. 2010; Wardlow et al. 2013; Vieira et al. 2013). At $z > 4$, we expect the lensing fraction to be substantial for current generation surveys, where the flux density limit for the source detection is relatively high. An example of a high efficiency lensing selection at $z > 3$ is the bright SMG sample from the South Pole Telescope at 1.4 mm (Vieira et al., 2013; Weiß et al., 2013). If lensing is a statistically important correction to the flux densities of high-redshift SMGs we expect them to be discovered near foreground galaxies and groups. Such a close association with a foreground galaxy is consistent with the existing indications that a reasonable fraction of the $z > 7$ Lyman-break drop-outs are also magnified by $\mu_{\text{lens}} \sim \text{few}$ due to their closeness to foreground bright galaxies (Wyithe et al., 2011).

In the case of HFLS3, a possibility for lensing was expected since the Keck/LRIS spectroscopy showed emission lines corresponding to a foreground galaxy at a $z = 2.1$ within one arcsecond of the peak 1.1 mm continuum emission. The high resolution Keck/NIRC2 LGS-AO imaging data in the K_s -band showed two galaxies within $1.''5$ of HFLS3. In Riechers et al. (2013)

the northern component was taken to be the $z = 2.1$ foreground galaxy, while the southern component, close to the peak 1.1 mm emission, was taken to be the rest-frame optical counterpart, or the least obscured part, of HFLS3. Under such an assumption, deblended NIRC2 and *Spitzer*/IRAC photometry suggested a stellar mass of $\sim 3.7 \times 10^{10} M_{\odot}$. Thus, HFLS3 is already a stellar mass-rich galaxy at $z = 6.34$, while continuing to form stars at a very high rate of $\geq 2000 M_{\odot} \text{ yr}^{-1}$.

The lack of multiple images of HFLS3 in mm-wave interferometric imaging data was inferred to imply that the lensing magnification factor is negligible, with $\mu_{\text{lens}} = 1.5 \pm 0.7$ associated with lensing by the foreground galaxy to the north of the assumed rest-frame optical counterpart. Due to such a small magnification a lensing correction to the properties of HFLS3 was not included in Riechers et al. (2013). However, the lensing magnification determination is subject to assumptions related to the counterpart identification and the location of foreground galaxies relative to the mm-wave emission. Since the true mass and star-formation rate of HFLS3 are directly related to its cosmic rarity, a potential lensing correction is even more important when addressing whether HFLS3 is a rare source among the SMG sample or if it is a source typical of $z > 4$ SMGs (Daddi et al., 2009; Coppin et al., 2010; Capak et al., 2011; Walter et al., 2012; Combes et al., 2012).

In this thesis we report *Hubble*/WFC3 and ACS imaging observations of HFLS3 in five filters from optical to near-IR wavelengths. We use these data to study the physical properties of HFLS3 by improving the lensing model and by identifying rest-frame optical/UV emission for a new estimate of the stellar mass of HFLS3. This paper is organized as follows. In the next Section we summarize the observations and the analysis. We discuss the counterpart identification and GALFIT (Peng et al. 2002) models in Section 4.3. Our lens models and the magnification factor of HFLS3 are presented in Section 4.4. In Section 4.5 we present the modeling of optical to IR SED of foreground galaxies and the UV to far-IR SED of HFLS3. We present a discussion of our key results and the implications for the

presence of massive, dusty starbursts galaxies at high redshifts in Section 4.6 and conclude with a summary in Section 5.1.3. For lensing and SED models we assume the best-fit concordance cosmology consistent with WMAP-9 year and Planck data (Hinshaw et al., 2013; Planck Collaboration et al., 2013).

4.2 *Hubble Space Telescope Observations*

HFLS3 was observed with *Hubble*/ACS and WFC3 in Cycle 21 (GO 13045; PI Cooray) in order to understand the nature and environment of currently the highest redshift dusty starburst known from sub-mm survey data. The observations were carried out in F160W/F125W/F105W filters with WFC3 and in F814W and F625W with ACS over a total of six orbits. The imaging data reach 5σ point source depths of $m_{\text{AB}} = 26.0, 26.3, 25.9, 27.0,$ and 26.1 in F160W, F125W, F105W, F814W, and F625W, respectively. While the WFC3 imaging was aimed at detecting the rest-frame UV emission from HFLS3, the ACS imaging was aimed at establishing the exact location, size, and morphology of the nearby $z \sim 2.1$ galaxy for an improved lens model. The five band photometry was aimed at completing the rest-UV SED of HFLS3 to improve the stellar mass estimate once combined with Keck/NIRC2 K_s and *Spitzer*/IRAC photometry. Here we focus on properties of HFLS3, but another study will discuss the environment of HFLS3 (La Porte et al. in preparation). The HST data are also useful for a near-IR counterpart search of SCUBA-2 sources detected in the HFLS3 field (Robson et al., 2014).

The *Hubble* data were analyzed with the standard tools. For WFC3 imaging data, we make use of CALWFC3 in the IRAF.STSDAS pipeline for flat-fielding and cosmic-ray rejection. Individual exposures in each of the filters were combined with ASTRODRIZZLE (Fruchter & et al., 2010) and we produced images at a pixel scale of $0.''06$ from the native scale of $0.''13$ per pixel. For flux calibration we made use of the latest zero-points from

STScI, with values of 26.27, 26.26 and 25.96 in F105W, F125W and F160W, respectively. Similarly, *Hubble*/ACS imaging data were flat-fielded, cosmic ray-rejected and charge transfer efficiency (CTE)-corrected with the pipeline CALACS (version 2012.2). Exposures were remapped with ASTRODRIZZLE to a pixel scale of $0.''03$. The ACS zero points used from an online tool are 25.94 and 25.89 for F814W and F625W, respectively.

The final *Hubble* mosaics were astrometrically calibrated to the wider SDSS frame with an overall rms uncertainty, relative to SDSS, of less than $0.05''$. This astrometric calibration involved more than 60 galaxies and stars. The previous Keck/NIRC2 imaging data, due to the limited field of view of $40''$ in the highest resolution NIRC2 imaging data used for LGS/AO observations, had large astrometric errors as astrometry was determined based on two bright sources that were also detected in 2MASS. Once the HST frames are calibrated, we fixed the astrometry of Keck/NIRC2 image with close to 10 fainter sources detected in both WFC3 and NIRC2 images. This astrometric recalibration resulted in a small ($0''.1$) shift to the optical sources relative to the peak PdBI/1.1 mm emission from HFLS3, as can be seen by comparing Figure 4.1 here with Figure 3 of Riechers et al. (2013). There is still an overall systematic uncertainty in the relative astrometry between IRAM/PdBI image and *Hubble*/Keck images of about $0''.1$, with this value possibly as high as $0''.3$ in an extremely unlikely scenario. We account for such a systematic offset in the lens model by allowing the peak 1.1-mm flux to have an offset from the two lens galaxies with a value as high as $0''.3$.

As shown in Fig. 4.1 (left panel), we detect optical emission from more than one galaxy near HFLS3 (galaxies labeled G1 and G2). This is similar to what was previously reported with Keck/NIRC2 LGS-AO imaging data, with the southern component (G2) taken to be the rest-frame optical counterpart to HFLS3 (Riechers et al., 2013). If this assumption is correct we expect the southern component to be invisible in the shortest wavelength images, as it is a Lyman drop-out at wavelengths shorter than 8900 \AA . Here, however, we have detected both galaxies in *Hubble*/ACS images, establishing that G2 is a galaxy at $z < 5$. Since these

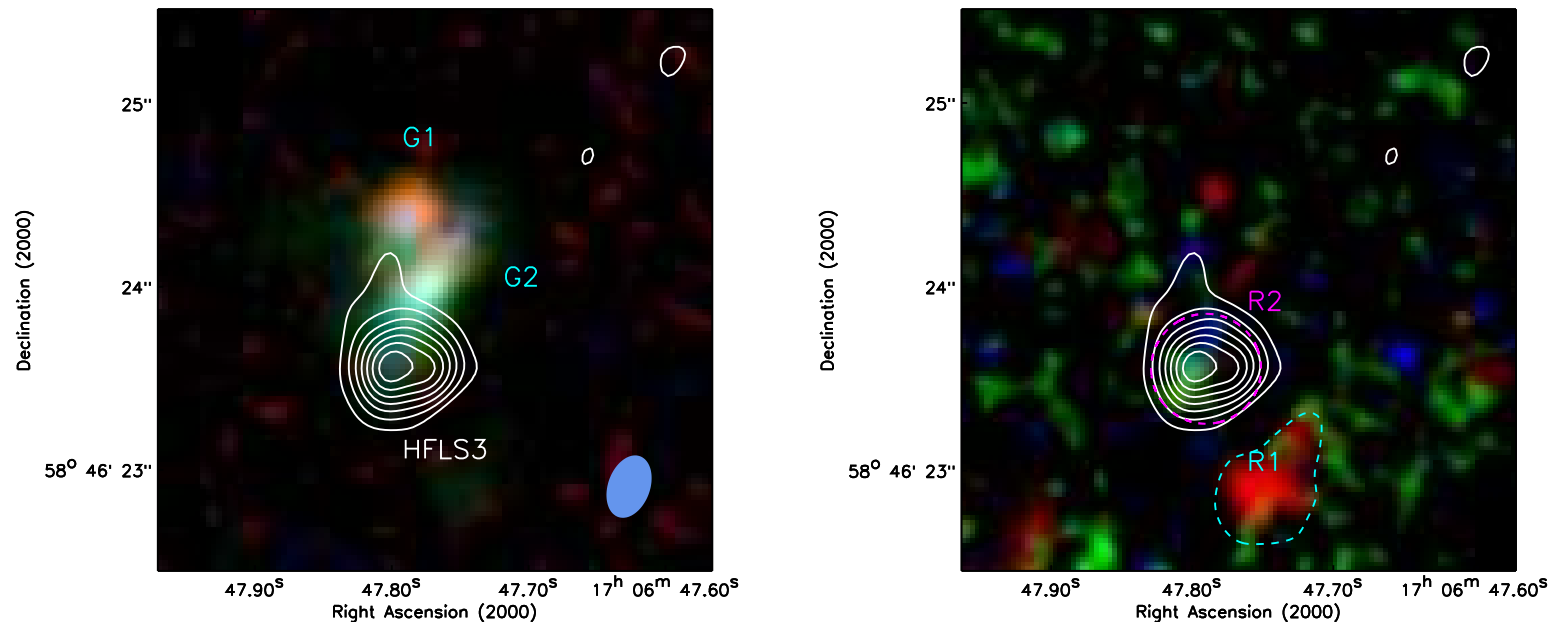


Figure 4.1: HST imaging of HFLS3.

Left: The three-color image using HST/ACS combined F625W and F814W (blue), HST/WFC3-IR combined F160W, F125W and F105, and Keck/NIRC-2 K_s -band LGS-AO (red) images. Note the clear detection of two galaxies close to HFLS3 shown here in terms of the IRAM/PdBI 1.1 mm (rest-frame $158 \mu\text{m}$) emission. The r.m.s. uncertainty in the PdBI A-array configuration data is $180 \mu\text{Jy beam}^{-1}$ and the contours are shown in steps of 3σ starting at 5σ . The instrumental beam is shown to the bottom right with FWHM of $0.35'' \times 0.23''$. *Right:* The three-color GALFIT residual map where we remove models for the HST/ACS-detected galaxies in HST/WFC3. Here we show the combination of ACS/F625W+F814W (blue), WFC3/F105W (green) and WFC3/F160W (red). Both G1 and G2 are detected in the combined ACS/F625W and F814W stack, consistent with the scenario that both G1 and G2 are at $z < 6$ and G2 is not the least obscured region, or the rest-frame optical counterpart, of HFLS3, as was previously assumed. We find a marginal detection of rest-UV emission at the location of HFLS3 (labeled R2) and a higher significance diffuse emission $0.''5$ to the South-West of HFLS3 (labeled R1). We use WFC3 fluxes and ACS upper limits of R2 for combined SED modeling of HFLS3 with far-IR/sub-mm flux densities. We determine a photometric redshift for R1 and find it to be consistent with emission from either a galaxy at $z \sim 6$ or a dusty galaxy at $z \sim 2$.

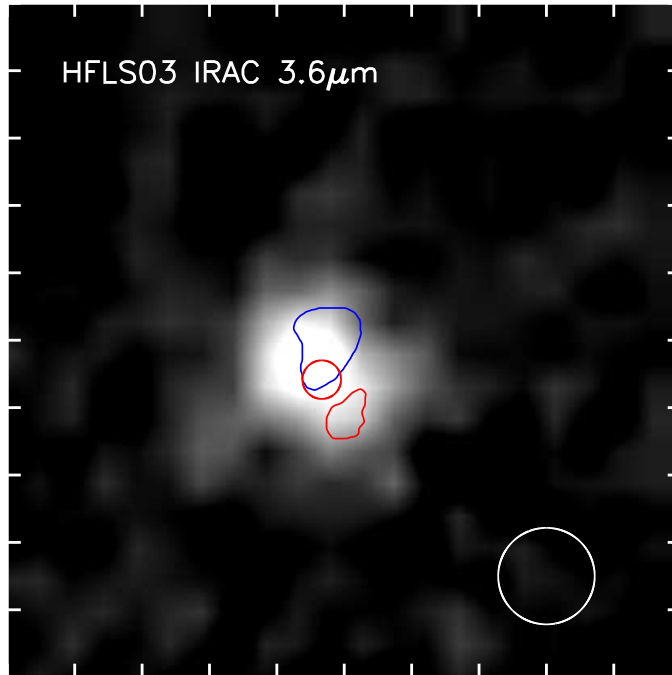


Figure 4.2: *Spitzer* IRAC Image of HFLS3.

$4 \times 4''$ *Spitzer*/IRAC $3.6 \mu\text{m}$ image from Riechers et al. (2013) showing a detected source. Each tick mark represents $2''$. The contours on the intensity scale show the region of G1 and G2 (blue) and R1 and R2 (red). The IRAC PSF ($\text{FWHM} = 1.5''$) is marked with a white circle on the bottom right.

Hubble observations, we have reanalyzed the Keck/LRIS spectrum shown in Riechers et al. (2013) with $z = 2.1$ CIV (1549 \AA) and OIII] ($1661, 1666 \text{ \AA}$) emission lines within $1''$ of HFLS3. We now find some marginal evidence that this emission is extended, consistent with the scenario that more than one galaxy may be contributing to the emission lines. A further confirmation of the redshift of G2 will require additional spectroscopic observations or UV imaging data where $z \sim 2$ galaxies would be Lyman dropouts. For simplicity, hereafter, we assume that both G1 and G2 are at the same redshift of 2.1. The SED modeling we discuss later is consistent with this assumption.

4.3 Rest-frame UV fluxes of HFLS3

We use the publicly available software GALFIT (Peng et al., 2002) to model the surface brightness profiles of *Hubble*-detected galaxies near HFLS3 and to see if there is any excess emission in WFC3 data relative to the ACS images. Using GALFIT on the individual *Hubble*/ACS and WFC3 frames proved to be difficult because the output models tend to overfit regions of low signal in which HFLS3 is expected to reside. To remedy this, we stacked the HST/ACS in two bands to increase the signal-to-noise ratio and to model the foreground galaxies in the combined F625W and F814W images. Under the assumption that the stacked model best represents the two foreground galaxies, we then subtracted the stacked model from individual HST/ACS and WFC3 frames, with the flux density at each wavelength allowed to vary as an overall normalization in GALFIT models. Any excess in WFC3 relative to ACS would suggest the presence of detectable rest-UV emission from HFLS3. As shown in Fig. 4.1 (right panel) we find excess emission primarily $0.''5$ to the South-West of HFLS3 (labeled R1). We also find some marginal evidence for excess emission near the 1.1-mm peak (labeled R2), with detection levels between 2.5 to 3.2σ . In Table 1 we summarize GALFIT and other intrinsic properties of the two foreground galaxies G1 and G2 as well as the residual emission R1 and R2, with R2 emission assumed to be from HFLS3. We also use the latter for a combined UV to far-IR SED modeling with MAGPHYS (da Cunha et al., 2008). We also model the SED of R2 to determine its photometric redshift and address its association with HFLS3.

4.4 Lens Modeling

We use the publicly available software GRAVLENS (Keeton, 2001) to generate the lens model. As the background source is not multiply-imaged, and remains undetected in the rest-frame

optical, we measure the goodness of fit of the model using the highest resolution IRAM/PdBI 1.1-mm continuum emission map from Riechers et al. (2013). This map is currently our highest resolution view of HFLS3, and the source is resolved in these data. The magnification factor we determine here with lens modeling is the value for the mm-wave continuum emission. It could be that HFLS3 will be subject to differential magnification, with different emission components within the galaxy subject to different magnification factors (e.g, Serjeant 2012; Hezaveh et al. 2012). This is especially true if the different components associated with HFLS, such as dust, gas, and stellar mass, have peak intensities that are offset from each other, as in the case of a complex merging galaxy system.

To simplify the lens modeling, we use singular isothermal ellipsoidal (SIE) models to fit for the Einstein radius and positions of the two lens galaxies. The position angles and ellipticities for G1 and G2 are fixed to the values derived from profile fitting using GALFIT, but their masses are allowed to vary freely. The relative positions of G1 and G2 are also kept fixed to *Hubble*/ACS-stack measurements, though we do allow the optical galaxy positions to vary relative to the peak location of the 1.1-mm continuum emission. For the source plane description of HFLS3, we considered two options: a single source for HFLS3; or a two component model for HFLS3. The latter is motivated by the fact that the highest resolution [CII] line emission may involve two velocity components separated by about 400 km s^{-1} (Riechers et al., 2013). In both these cases, the background source(s) is/are modeled with free parameters for the positions and effective radii. For simplicity, we assume Gaussian circular profiles with a fixed Sersic index of 0.5. The effective radii in the source plane are allowed to vary in the range of $0.005''$ to $2.0''$, with the upper end at a value higher than the measured size of the 1.1-mm continuum emission in the PdBI image. In the case of the two component model, the flux ratio between the two background components is also left as a free parameter. Hence, the lens model fits for a total of five free parameters for the case with one component for HFLS3 or nine free parameters for the case with two components. We take this two component model for the background source as a default model here, though

our conclusions do not change if we adopt the single component model.

In the lens modeling procedure, we output a lensed image as would be observed at 1.1-mm. However, to compare with the data, we convolve that image with the PdBI beam before calculating the χ^2 value. This process is iterated over a wide parameter space using the IDL routine AMOEBA_SA, which uses a downhill simplex algorithm and simulated annealing to perform multidimensional minimization. We use a circle of a radius $1''.5$ centered on the peak pixel value of the PdBI 1.1-mm image to measure parameter errors from uncorrelated noise. For each iteration, the 1.1-mm magnification factor we quote, μ_{lens} , is calculated by simply summing up all the pixel values in the image plane and dividing it by the sum of the pixel values in the source plane.

Fig. 4.3 shows the best-fit model for the two scenarios with one and two components. In the case of two components, we determine $\mu_{\text{lens}} = 2.2 \pm 0.3$. The two components have effective radii of 0.5 ± 0.1 kpc and 0.3 ± 0.1 . The best-fit model has χ^2 and number of degrees of freedom (Ndof) values of 9929 and 7835, respectively. For reference, the model with a single component for the background source has $\mu_{\text{lens}} = 2.0_{-0.1}^{+0.9}$, an effective radius of 0.6 ± 0.1 kpc, and χ^2/Ndof of 100552/7839. The lensing masses are $M_{\text{lens}} = 1.2_{-0.2}^{+6.4} \times 10^9 M_{\odot}$ and $1.2_{0.1}^{+0.2} \times 10^{10} M_{\odot}$ for G1 and G2, respectively for the two component model. We find masses consistent within these errors for the case when HFLS3 is described by a single component. The lensing model is mostly sensitive to the mass of G2, while G1, the galaxy fatherst from HFLS3, remains as a minor contribution to the lens model. Therefore the mass of G1 is less constrained in the lens model. The best-fit Einstein radius for G1 that we find with the value of $0''.05_{-0''.04}^{+0''.06}$ is barely above the lower value of $0''.01$ for the Einstein radius that we placed on the parameter ranges. We emphasize that the lens model presented here does not require the presence of two lenses in the foreground or two sources in the background to fit the data.

Note that we have assumed the redshifts of G1 and G2 are the same in the lens model. The

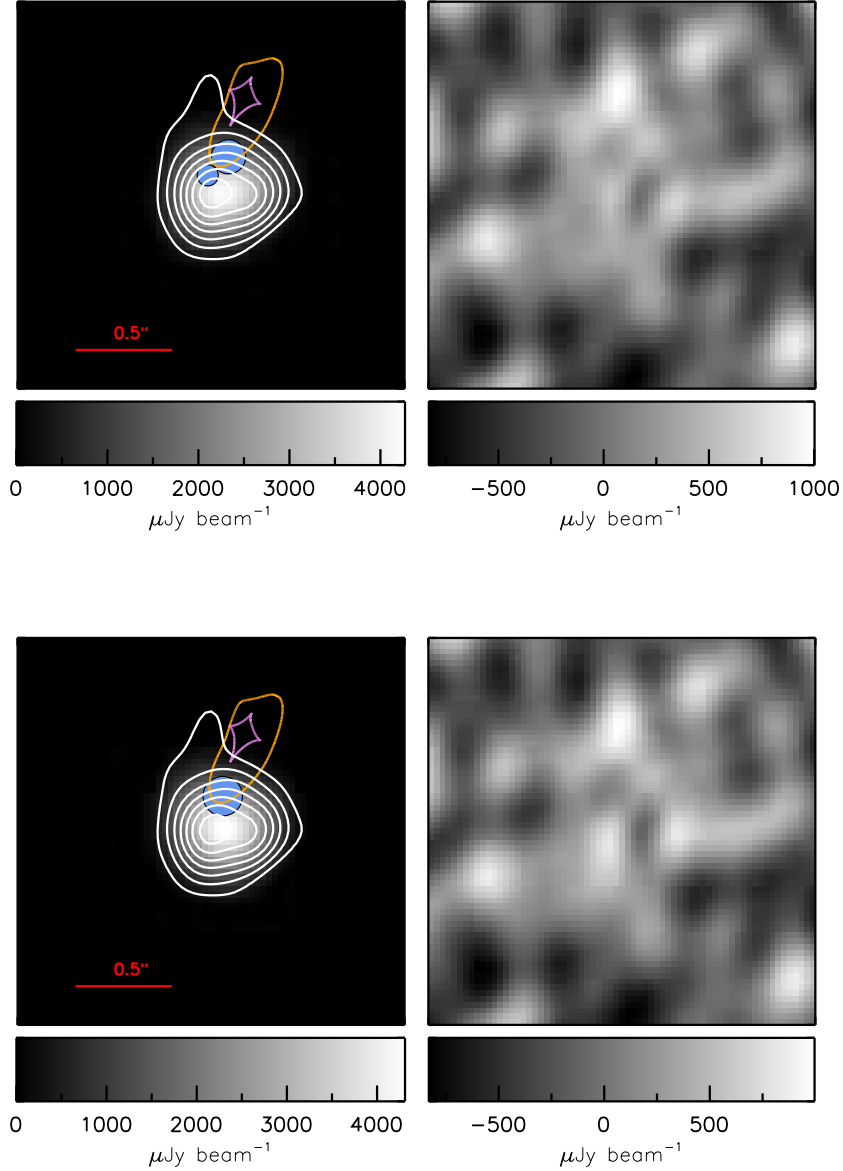


Figure 4.3: Lens Model of HFLS3.

Top Left: The source and image planes of HFLS3 under the best-fit lens model with two components for the background source to describe HFLS3. In blue we show the two components of HFLS3 in the source plane that are gravitationally magnified. The image plane involves the background grey-scaled color that is compared to the measured IRAM/PdBI 1.1-mm continuum emission shown with contours. The two lines are the critical line (orange), in the image plane, and the lensing caustic (pink), in the source plane. *Top Right:* Residual map for the best-fit model showing the difference between observed IRAM/PdBI 1.1-mm continuum emission and the lens model output. *Bottom Left and Right:* The lens model and residual for the case involving HFLS3 described by a single source (shown in blue). The lines and the residual intensity to the right follow the same as top two panels.

lens models discussed here are insensitive to the exact assumption related to the redshifts of G1 and G2 as a change in redshift is degenerate with their lensing masses. Our lens model also assumes a single lensing plane and do not account for multiple-plane lensing if G1 and G2 are at two different redshifts. If the two galaxies are indeed at the same redshift, they could be part of a galaxy group. The mass we have determined then could have a contribution from the group potential and will be higher than the value implied by the stellar mass of these galaxies. Our lens models do show some evidence for such a possibility, but due to overall uncertainties in the stellar mass from SED fits, we cannot reliably confirm this with current data.

In addition to the best-fit lens model, we are also able to place a reliable upper limit on the lensing magnification of HFLS3 at 1.1 mm. This is simply based on the fact that we have not detected a counter image to HFLS3, while large magnification factors usually result in image multiplication leading to a detectable counter image. Using the same modeling procedure as described above, and allowing for the model to vary over all ranges and including a relative astrometry as high as $0''.3$ between 1.1-mm image and lens locations, we constructed the probability distribution function (PDF) of magnification for the two cases involving one and two source components to describe HFLS3 in the source plane. In Fig. 4.4 we show the histogram where we highlight the 95% confidence level upper limit on magnification such that $\mu_{\text{lens}} < 3.5$ and 2.7 for the two cases with one and two components, respectively. The probability distribution functions also show that there is a strict lower limit to magnification and the case with $\mu_{\text{lens}} = 1$, HFLS3 is unlensed, is ruled at more than 6σ . This is simply because of the fact that even a very small mass for G2, the galaxy closest to HFLS3, will result in some lensing magnification of HFLS3.

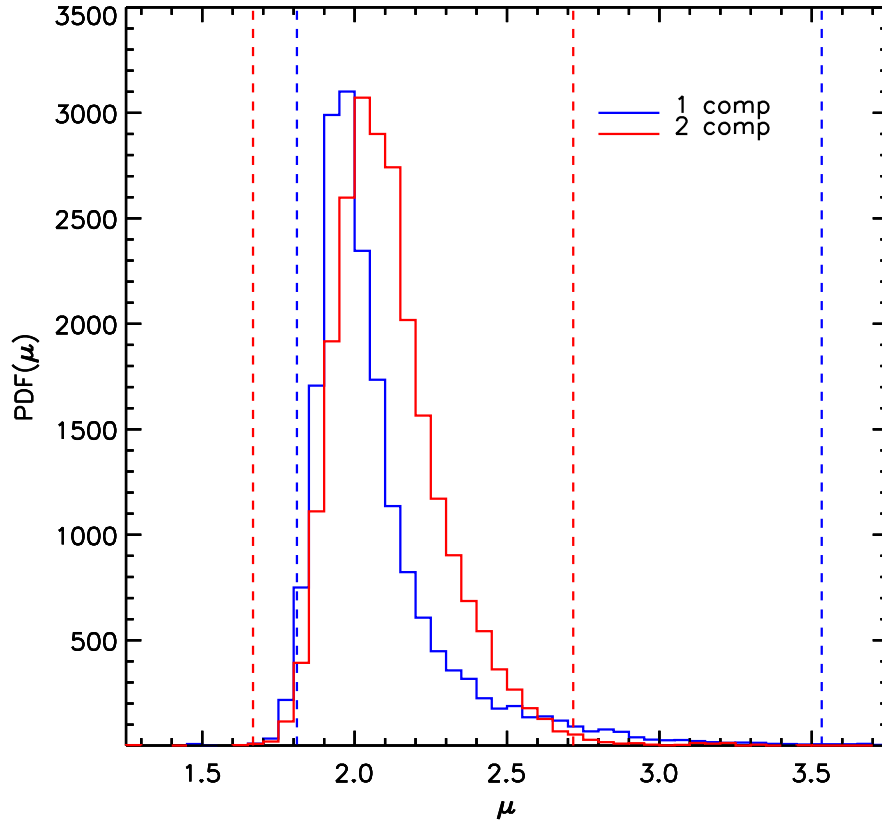


Figure 4.4: Probability distribution function of μ_{lens}

Probability distribution function of the lensing magnification μ_{lens} at 1.1 mm for HFLS3. We show two scenarios here for the case where HFLS3 is described by either a single (blue) or double (red) source in the source plane. The vertical lines show the 95% confidence level upper limit on the magnification. Note that in both scenarios there is also a strict lower limit for magnification with $\mu_{\text{lens}} > 1.6$ at the 95% confidence level. The case with $\mu_{\text{lens}} = 1$ is rejected at $> 6\sigma$ in both cases.

4.5 SED Modeling

We carry out SED modeling of both foreground and background galaxies using a combination of HYPERZ¹ (Bolzonella et al., 2000) and MAGPHYS (da Cunha et al., 2008). For SED modeling involving G1 and G2, we fix the redshift to the value determined from optical spectroscopy (Fig. 4.5). We make use of Bruzual & Charlot (2003) SED templates with a combination of single burst, constant, and exponentially declining star-formation history (τ -models), with τ fixed at 1 Gyr (“E”) and 5 Gyr (“Sb”). Internal reddening is included using the Calzetti et al. (2000) extinction law, and allowing $A_V = 0$ to 5 magnitudes in steps of 0.2. We also make use of the default Lyman- α forest following the prescription from (Madau, 1995). Given the parameters from the SED modeling (SED type, A_V , age etc), we then make use of the Bruzual & Charlot (2003) models to calculate the H-band mass-to-light ratio assuming a Chabrier IMF (Chabrier, 2003). In the case of SED fits, we note that quoted error bars are the formal uncertainties and do not include systematic effects. In most of our modeling cases, it could very well be that uncertain systematics, such as on the choice of SED templates, dominate the error budget.

For G1 and G2, we find stellar masses of 8×10^8 and $1 \times 10^{10} M_\odot$, respectively. The ratio of stellar-to-lensing mass for two lensing galaxies at $z = 2.1$ ranges from 0.66 to 0.85. We find that significant dust attenuation is present in the northern galaxy G1, with $A_V \sim 3.4$ mag. We do not find mm-wave emission from that galaxy in our deep 1.1 mm interferometric continuum emission data, ruling out a sub-mm bright dusty galaxy at this location. It could be that G1 is blended with another galaxy or that our assumption of 2.1 for the redshift is invalid. As our conclusions related to the physical properties of the two foreground galaxies depends on their redshifts, we caution that the properties of these galaxies not be overly-interpreted. Further deep imaging and spectroscopy should resolve some of the remaining puzzles in the data.

¹v12.2 available from <http://userpages.irap.omp.eu/~rpello/newhyperz/>

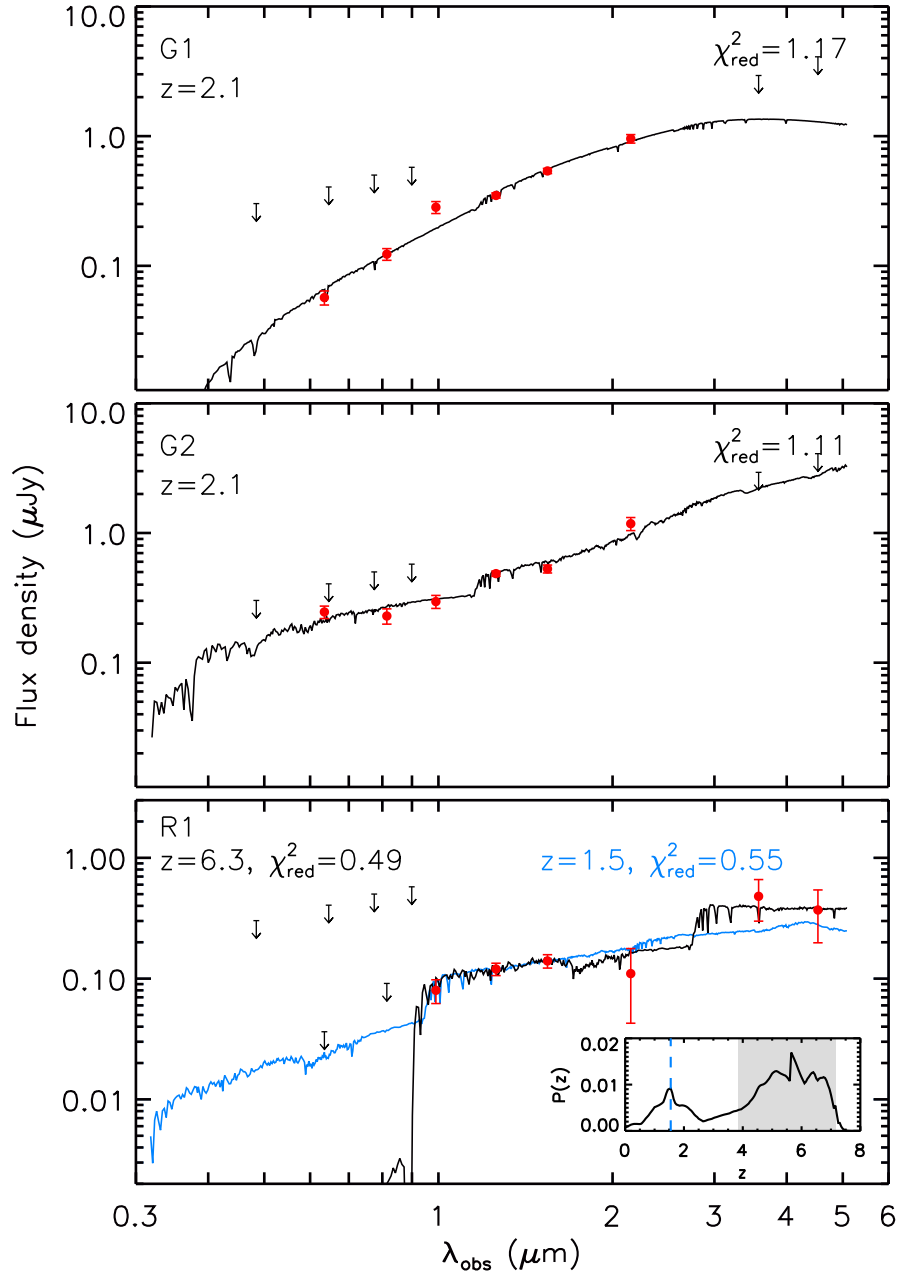


Figure 4.5: SEDs and best-fit HYPERZ models for the HFLS3 lensing system. SEDs and best-fit HYPERZ models for optical to IR SEDs of G1 (top), G2 (middle), and R1 (bottom). For G1 and G2 we assume the optical redshift of 2.1, though we have yet to establish if the measured optical redshift applies to either G1 or G2, or both. For R1, we allow the redshift to vary as part of the SED models, and the probability distribution function for the photometric redshift is shown in the inset to the bottom right of the panel. We find two solutions with one at high redshift consistent with $z \sim 6$ and a second, involving dusty galaxy templates, at $z \sim 1.3 - 2.3$.

Given the nature and rarity of sources such as HFLS3 at $z > 5$, it is useful to address the extent to which the recent *Hubble*/ACS and WFC3 imaging changes the underlying properties of this dusty, starburst galaxy. In order to establish the rest-frame UV fluxes of HFLS3, we made use of the ACS-based models of the two foreground galaxies to search for excess emission in the longer wavelength data. Note that in ACS, $z > 6$ emission should not appear, since as at those redshifts galaxies will be dropping out of the band due to the Lyman limit. Using the ACS models on WFC3 data, we found marginal evidence, at around 3.5σ , for rest-frame UV emission at the PdBI 1.1-mm emission position in F125W (region marked as R2 in Fig. 4.1 right panel). At the same location we also found 2.8σ residual emission in both the F160W and Keck/NIRC2 images. We consider these flux densities to be the rest-UV emission from HFLS3 itself.

Unfortunately due to blending in the $\sim 2''$ PSF, we are not able to deconvolve the existing *Spitzer*/IRAC data to precisely determine the rest-frame optical fluxes of HFLS3 (Fig. 4.2). The IRAC fluxes for HFLS3 reported in Riechers et al. (2013) made use of a GALFIT model for G2 with Keck/NIRC2 image to deblend its contribution from the total. The residual fluxes are then those corresponding to G1 and HFLS3 in IRAC data and the total residual was assumed to be those of HFLS3, under the assumption that G1 is the near-IR counterpart of HFLS3. However, as discussed above, such an assumption no longer applies. We can only place an upper limit on the fluxes after removing both G1 and G2. We find that even such an upper limit is subject to assumptions related to GALFIT modeling in IRAC images, where multiple components exist within a single IRAC PSF.

With the rest-UV fluxes for HFLS3 determined with *Hubble*/WFC3 and Keck/NIRC2 data fluxes, we cover four orders of magnitude in wavelength from rest-frame UV to far-infrared (Fig. 4.6). This SED of HFLS3 is fitted using MAGPHYS, where models are calibrated to reproduce ultraviolet-to-infrared SEDs of local, purely star-forming Ultra Luminous Infrared Galaxies (ULIRGS; $10^{12} < L_{\text{IR}}/L_{\odot} < 10^{13}$). Such models, however, are best on the assump-

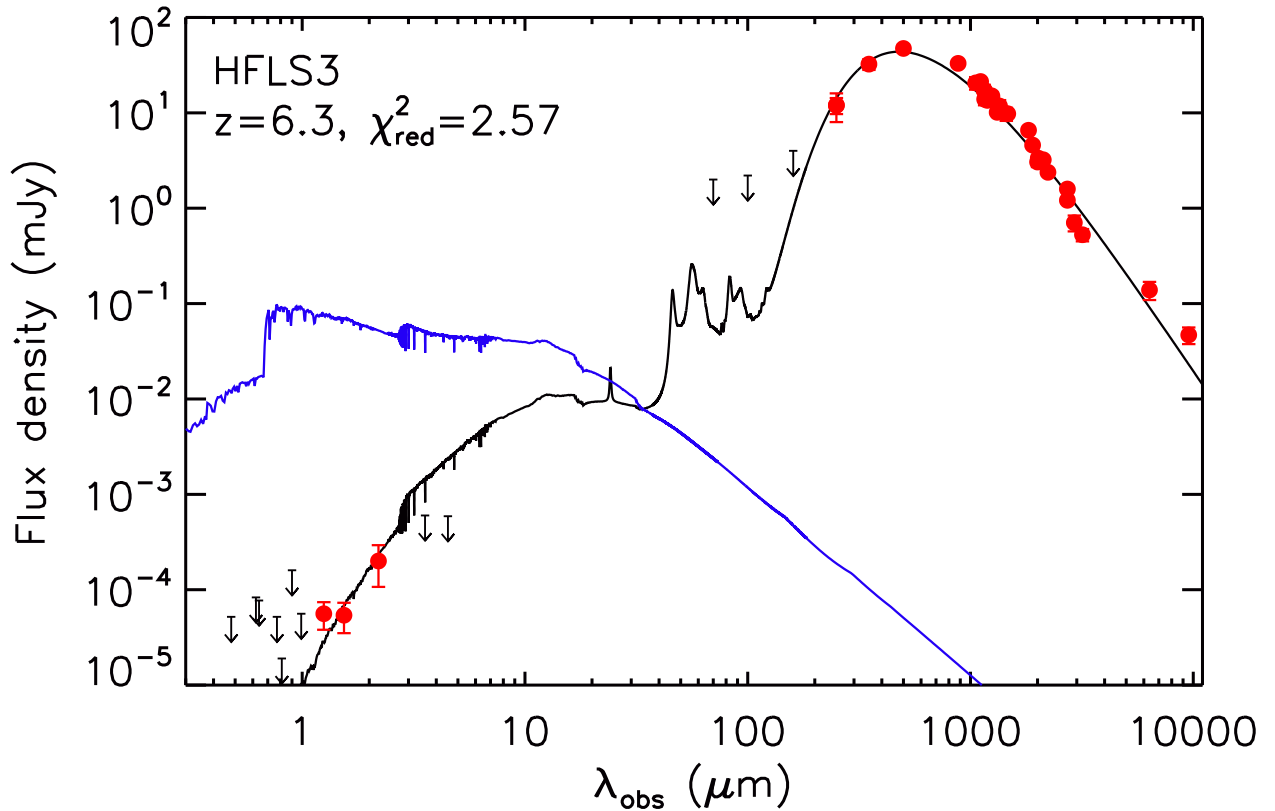


Figure 4.6: Best-fit composite SED of HFLS3.

MAGPHYS (da Cunha et al. 2008) best-fit SED model of HFLS3 from rest-UV to far-infrared over four decades in wavelength. The blue line shows the unobscured template. For UV to sub-mm SED modeling, we make use of the far-IR/sub-mm data shown by solid symbols. Other measurements shown with open symbols involve non-standard bands that are not part of the filter and bandpass table of MAGPHYS. They were obtained as part of continuum measurements during atomic and molecular line measurements of HFLS3 with ground-based interferometers.

tion that dust and stars are in a fully-mixed medium. Massive, dusty starbursts at $z > 2$ may not follow such mixing with differential obscuration causing biases in the combined UV to radio SED. For example, regions that are bright in the rest-frame optical may only be a small fraction of the regions that are bright in the far-infrared and sub-mm wavelengths. The use of MAGPHYS to model such complex galaxies may result in biased estimates of the physical parameters, but in the absence of other methods to study the combined SED, we have decided to use MAGPHYS here with appropriate cautions.

The SED model assumes a Chabrier (2003) initial mass function (IMF) that has a cutoff below $0.1 M_{\odot}$ and above $100 M_{\odot}$; using a Salpeter IMF instead gives stellar masses that are a factor of ~ 1.7 to 1.8 larger. With MAGPHYS-based SED models, we find that HFLS3, with rest-UV fluxes in the region marked as R2, shows significant dust attenuation with $A_V \sim 3.6$ mag. Such attenuation is consistent with $z \sim 2$ ULIRGs and SMGs (e.g., Smail et al. 2004; Chapman et al. 2005; Geach et al. 2007; Swinbank et al. 2010; Wardlow et al. 2011; Hainline et al. 2011; Lo Faro et al. 2013). The best-fit MAGPHYS SED model is shown in Fig. 4.6. The fit is dominated by the far-IR/sub-mm data and the overall fit has a reduced χ^2 value of 1.6.

4.6 Discussion

The MAGPHYS SED models of HFLS3 described above lead to SFR, dust mass, stellar mass among other properties. As outlined in Riechers et al. (2013), instantaneous SFR, using the FIR luminosity and assuming a Chabrier (2003) IMF to scale the Kennicutt (1998) relation, is $\sim 2900 M_{\odot} \text{ yr}^{-1}$. Using the MAGPHYS SED model, we find that the apparent SFR, averaged over the last 100 Myr, to be $1450 \pm 100 M_{\odot} \text{ yr}^{-1}$. Note that these SFRs must be corrected down by the factor μ_{lens} to account for lensing magnification. With our preferred best-fit correction factor of 2.2 ± 0.3 for the model involving two components to

describe 1.1-mm emission from HFLS3, the instantaneous and 100-Myr averaged SFRs are $\sim 1300 M_{\odot} \text{ yr}^{-1}$ and $\sim 660 M_{\odot} \text{ yr}^{-1}$, respectively. The two are different as the Kennicutt (1998) relation assumes a bolometric luminosity of a constant star-formation lasting over 100 Myr emitted in the infrared (Kennicutt, 1998; Leitherer & Heckman, 1995). For a constant star-formation, bolometric luminosity after the first 10 Myr evolves relatively slowly as the rate of birth and death of massive stars that dominate the bolometric luminosity reach a steady state. For starbursting galaxies, however, the SFR is likely changing rapidly over the 100 Myr time interval and we may be observing the galaxy at the peak of the SFR. Such a possibility then naturally explains why the instantaneous SFR is a factor of two higher than the SFR averaged over the last 100 Myr.

We can also place a strict lower limit on the SFRs using the 95% confidence level upper limit on lensing magnification. This leads to values of $> 780 M_{\odot} \text{ yr}^{-1}$ and $390 M_{\odot} \text{ yr}^{-1}$ for instantaneous and 100-Myr averaged SFRs, respectively. This revision of the SFR to a lower value is consistent with a similar revision to the SFR of $z = 5.3$ SMG AzTEC-3 (Capak et al., 2011). While the total IR luminosity implies a SFR of $1800 M_{\odot} \text{ yr}^{-1}$ (Capak et al., 2011; Riechers et al., 2010), SED modeling of the fluxes with population synthesis models have shown the SFR, averaged over the last 100 Myr, to be as low as $500 M_{\odot} \text{ yr}^{-1}$ (Dwek et al., 2011). Our SED models also show that the age of the oldest stars in HFLS3 is around 200 Myr, suggesting that HFLS3 started assembling its stars at a redshift of ~ 8 , during the epoch of reionization.

Using the far-IR/sub-mm SED and the standard assumptions used in MAGPHYS, and correcting for magnification, the dust mass of HFLS3 is $\sim 3 \times 10^8 M_{\odot}$, with a lower limit at $2 \times 10^8 M_{\odot}$. The ISM includes two components with dust temperatures of 24 ± 2 and 50 ± 2 K. The best-fit SED model is such that $> 90\%$ of the dust mass is in the warm phase, contrary to low-redshift star-forming galaxies that have a lower ratio. Such a high ratio for HFLS3 establishes that most of the dust is associated with star-bursting clumps and not the

diffuse cirrus. The implied dust temperature of the cold phase component is comparable to the CMB temperature at $z = 6.3$, suggesting that the extended cirrus of this galaxy may be in radiative equilibrium with the CMB. Using the Chabrier (2003) IMF, with parameters derived again from the SED fits using MAGPHYS, and with lensing magnification included, we find that HFLS3 has a stellar mass of about $5 \times 10^{10} M_{\odot}$. This stellar mass, however, is highly uncertain as it is based on just three detections at the rest-frame UV wavelengths. And in all of these cases, the detections are at the level of 3σ . Furthermore, we have assumed that the magnification factor derived with 1.1-mm continuum map also applies for the rest-frame UV emission from which the stellar mass is derived. Regardless of these uncertainties, we find that HFLS3 has already formed a substantial amount of stellar mass already. Such a high stellar mass is already at the limits allowed by the dynamical mass of HFLS3 reported in Riechers et al. (2013).

While the SED-based stellar mass is uncertain by an order of magnitude once all modeling errors are accounted for, the dust mass of HFLS3 with a value $\sim 3 \times 10^8 M_{\odot}$ provides an additional constraint on the stellar mass of HFLS3. This comes from models related to the dust formation mechanisms in massive starbursts where core collapse supernovae (CCSNe) are expected to be the origin of the bulk of the elements that formed the dust. The contribution of low mass stars to the refractory elements is negligible in a young galaxy such as HFLS3. Thus, the total number of CCSNe that exploded in the galaxy dictates the maximum dust mass. Following the arguments in Watson et al. (2014, in preparation), from an observed dust mass, we can infer the minimum number of supernovae that occurred and for a particular initial mass function, the resulting lower bound on the stellar mass. The simplest and most robust way to make such an estimate on the stellar mass is to work from observations. SN 1987A is close to the mass-integrated mean CCSN mass for most IMFs and is the best-observed CCSN remnant known. Assuming SN 1987A as a good mass-weighted mean for the dust production, and using the preferred value of a carbonaceous and silicate grain mix of $0.60.7 M_{\odot}$ (Matsuura et al., 2011; Indebetouw et al., 2014), we can infer that

at least $2 \times 10^8 M_{\odot}$ CCSNe exploded in HFLS3 to account for the dust mass of $3 \times 10^8 M_{\odot}$.

The stellar-to-dust mass ratio should be around 100 for a Chabrier IMF, and a factor of two larger than this for a Salpeter IMF. The precise value of this ratio depends on how CCSNe produce refractory metals as a function of mass. When considering model uncertainties, the stellar-to-dust mass ratio is within 20% of the value quoted above, where the dust masses are tied through the observational pivot point provided by the dust mass observed in SN 1987A. Note that this argument is currently based on the dust mass observed in SN 1987A as an indication of the refractory element production, rather than claiming that CCSNe necessarily produce all the dust directly. But since the dust mass observed is believed to be close to the maximal dust production for this SN (Indebetouw et al., 2014), it is therefore a reasonable reflection of the most dust we could ultimately expect to be produced by the elements synthesised by SN 1987A. Thus, for $3 \times 10^8 M_{\odot}$ mass of dust in the galaxy, we expect a minimum of $\sim 2 \times 10^{10} M_{\odot}$ mass of stars for a Chabrier IMF, and twice this for a Salpeter IMF. This is comparable to the lensing magnification-corrected stellar mass inferred from MAGPHYS at $5 \times 10^{10} M_{\odot}$, though we note once again that this value has a large uncertainty due to various assumptions and low signal-to-noise ratio of the rest-frame UV measurements. For a SFR averaged over 100 Myr of about $660 M_{\odot} \text{ yr}^{-1}$, the above arguments imply a characteristic dust production time of at least 40 Myr, assuming a negligible dust destruction during the same period. This is lower than the suggested lifetime for dust mass assembly in AzTec-3 of about 200 Myr (Dwek et al., 2011). While our current estimates are uncertain, the above argument, however, can be strengthened in the future with more precise measurements of dust and stellar masses to constrain dust production mechanisms at $z \sim 6$.

We also attempted a SED model with far-IR/sub-mm data points combined with rest-UV fluxes from R1, with peak emission $0.5''$ to the South-West of HFLS3 (Fig. 4.1). This emission is detected in all three WFC3 bands at significances greater than 6σ in each, although the

emission remains undetected in ACS. The emission, however, is blended in IRAC data with the near-IR emission from the two galaxies (Fig. 4.2). The MAGPHYS fit was considerably poor as there was no consistent SED that can fit the four orders of magnitude in wavelength from UV to sub-mm in that case with the best-fit case having a reduced χ^2 of greater than 5. This ruled out a scenario in which HFLS3 sub-mm emission is associated with R1. It also rules out an extreme scenario in which our relative astrometry between IRAM/PdBI and *Hubble* images are wrong such that the near-IR counterpart to HFLS3 is R1. We find that R1 must be a separate source. The HYPERZ SED model shown in Fig. 4.5 leads to a photometric redshift for this emission is consistent with a source at $z \sim 6.3$ (Fig. 4.3 bottom panel), though a dusty galaxy SED at $z \sim 2$ is also consistent with this emission. The HYPERZ fit to the data leads to a stellar mass of $\sim 1.2 \times 10^{10} M_{\odot}$ for R1. We have two possibilities for this source. It could be part of the emission associated with a complex galaxy merger system involving HFLS3, especially if HFLS3 starburst is triggered by a merger as is the case for most $z \sim 2$ bright SMGs (e.g., Casey et al. 2014 for a recent review). **add ref** Alternatively, it could be part of the $z \sim 2.1$ foreground structure that is responsible for lensing of HFLS3. If latter is indeed the case, the region in the foreground of HFLS3 involves a massive galaxy group, but the magnification upper limit of 3.7 we have derived here is unlikely to be revised higher as it accounts for a wide variation of model parameters, including to the total lens mass in the foreground. It is far more likely that R1 is part of the complex merger system associated with HFLS3.

Table 4.1: IR Properties of HFLS3 and Nearby Galaxies²

Quantity	Value	Ref
G1		
RA	17 : 06 : 47.80	ACS I_{814} -band
Dec	+58 : 46 : 24.33	ACS I_{814} -band
Redshift	2.019	Riechers et al. 2013
ACS/F625W	27.01 ± 0.14 (AB mag)	Photometry
ACS/F814W	26.17 ± 0.12 (AB mag)	Photometry
WFC3/F105W	25.27 ± 0.12 (AB mag)	Photometry
WFC3/F125W	25.27 ± 0.04 (AB mag)	Photometry
WFC3/F160W	24.57 ± 0.09 (AB mag)	Photometry
NIRC2/ K_s -band	23.94 ± 0.04 (AB mag)	Photometry
R_E	$0''.05^{+0''.06}_{-0''.01}$	lens model
M_E	$(1.2^{+6.4}_{-0.2}) \times 10^9 M_\odot$	lens model
R_e	$0''.9 \pm 0''.3$	GALFIT
	7.1 ± 2.3 kpc	
ϵ	0.48 ± 0.02	GALFIT
PA_d	$(88 \pm 2)^\circ$	GALFIT
n (Sérsic)	4.3 ± 0.8	GALFIT
M_\star	$\sim 8 \times 10^8 M_\odot$	SED (HYPERZ)
A_V	~ 3.4 mag	SED (HYPERZ)
L_V (extinction corrected)	$\sim 3 \times 10^{11} L_\odot$	SED (HYPERZ)
G2		
RA	17 : 06 : 47.77	ACS I_{814} -band
Dec	+58 : 46 : 23.95	ACS I_{814} -band

Table 4.1 – Continued

Quantity	Value	Ref
ACS/F625W	25.42 ± 0.13 (AB mag)	Photometry
ACS/F814W	25.50 ± 0.16 (AB mag)	Photometry
WFC3/F105W	25.22 ± 0.13 (AB mag)	Photometry
WFC3/F125W	24.68 ± 0.05 (AB mag)	Photometry
WFC3/F160W	24.59 ± 0.13 (AB mag)	Photometry
NIRC2/K _s -band	23.72 ± 0.09 (AB mag)	Photometry
R_E	$0''.15^{+0''.02}_{-0''.01}$	lens model
M_E	$(1.2^{+0.2}_{-0.2}) \times 10^{10} M_\odot$	lens model
R_e	$0.34 \pm 0.01''$	GALFIT
	2.8 ± 0.1 kpc	
ϵ	0.63 ± 0.01	GALFIT
PA _d	$(-30 \pm 1)^\circ$	GALFIT
n (Sérsic)	0.98 ± 0.03	GALFIT
M_\star	$1 \times 10^{10} M_\odot$	SED (HYPERZ)
A_V	1.20 mag	SED (HYPERZ)
L_V (extinction corrected)	$4 \times 10^{10} L_\odot$	SED (HYPERZ)
HFLS3		
RA	17 : 06 : 47.80	Riechers et al. 2013
Dec	+58 : 46 : 23.51	Riechers et al. 2013
Redshift	6.3369 ± 0.0009	Riechers et al. 2013
ACS/F625W	> 27.01 (AB mag)	Photometry
ACS/F814W	> 28.20 (AB mag)	Photometry
WFC3/F105W	> 27.58 (AB mag)	Photometry

Table 4.1 – Continued

Quantity	Value	Ref
WFC3/F125W	27.02 ± 0.35 (AB mag)	Photometry
WFC3/F160W	27.06 ± 0.38	Photometry
NIRC2/K _s -band	25.64 ± 0.50	Photometry
μ_{lens}	2.2 ± 0.3	two-component model
Θ_{s1}	$0''.5 \pm 0''.1$	component 1
	2.6 ± 0.7 kpc	
Θ_{s2}	$0''.3^{+0''.2}_{-0''.1}$	component 2
	$1.6^{+1.2}_{-0.6}$ kpc	
$\frac{F_2}{F_1}$	$0.3^{+0.4}_{-0.2}$	Flux ratio
M_{dust}	$9 \times 10^8 M_{\odot}$	SED (MAGPHYS)
SFR_{int}	$1320 M_{\odot} \text{ yr}^{-1}$	Kenicutt (1998)
$\langle \text{SFR} \rangle_{100 \text{ Myr}}$	$654^{+104}_{-90} M_{\odot}/\text{yr}$	SED (MAGPHYS)
M_{\star}	$\sim \times 10^{11} M_{\odot}$	SED (MAGPHYS)
A_V	3.6 mag	SED (MAGPHYS)
L_V (extinction corrected)	$\sim 4 \times 10^{12} L_{\odot}$	SED (MAGPHYS)
R1		
RA	17 : 06 : 47.76	WFC3 H_{160} -band
Dec	+58 : 46 : 22.87	WFC3 H_{160} -band
ACS/F625W	> 27.01 (AB mag)	Photometry
ACS/F814W	> 26.85 (AB mag)	Photometry
WFC3/F105W	26.68 ± 0.28 (AB mag)	Photometry
WFC3/F125W	26.20 ± 0.14 (AB mag)	Photometry
WFC3/F160W	26.03 ± 0.15 (AB mag)	Photometry

Table 4.1 – Continued

Quantity	Value	Ref
NIRC2/K _s -band	26.30 ± 0.92 (AB mag)	Photometry

²**Notes**—We assume $z_{G1} = z_{G2}$. Flux density lower limits are given at 3σ .

Chapter 5

Conclusions

In this thesis we describe how we use far-IR observations to study dusty star-forming galaxy populations. The study of DOGs in Chapter 2 allows us to constrain the shape of the far-IR SED from direct observations, effectively making calculations of IR luminosities and star-formation rates more accurate. In Chapter 3, we use *Herschel* data to select a lensed candidate sample of $500\ \mu\text{m}$ bright sources. A follow-up effort to acquire near-IR imaging for these sources reveal that some of these candidates are indeed bonafide lensing events. By exploiting our high-resolution data, we derive lens models to recover the intrinsic properties of the background SMG. I conclude this thesis by summarizing our main results and discuss unresolved questions which will be the focus of future studies.

5.1 Summary of Main Results

5.1.1 The Far-Infrared Emission From Dust-Obscured Galaxies

IR Luminosity Function and Stacking: The IR luminosity function of DOGs at $z = 1.5 - 2.5$ is calculated and shows that they contribute 30% to the luminosity function of $24\ \mu\text{m}$ -selected galaxies. The stacked infrared luminosities provide significant contribution in the lowest detected IR luminosity bin, causing an increase of ~ 0.2 dex. IR luminosities derived from extrapolating $24\ \mu\text{m}$ flux densities of local galaxy templates are overestimated by a factor of around 2 and therefore, direct observations in the far-IR that sample the cold-dust emission from galaxies should always be used, if available, to calculate more accurate estimates.

DOG Contribution to ρ_{SFR} : DOGs contribute 10 – 30% to the overall star-formation rate density of the Universe and 39% for all $24\ \mu\text{m}$ galaxies with $S_{24} \geq 100\ \mu\text{Jy}$. We also note that when compared to the total DOG ρ_{SFR} , power-law (AGN dominated) DOGs provide minor contributions. The ρ_{SFR} for DOGs and SMGs are comparable at $z \sim 2$, however we note that DOGs are more numerous, with individually lower star-formation rates for DOGs than SMGs.

Star-formation rates and Stellar Masses: DOGs have a large scatter in the $\text{SFR} - M_*$ plane, having sources in the starburst, main sequence and more quiescent galaxy regimes. The observed phase of star-formation for most DOGs is likely responsible for their observed stellar mass, supported by their mass doubling timescales ($1/\text{sSFR}$) being shorter than the age of the Universe at $z \sim 2$.

5.1.2 Gravitationally Lensed *Herschel*-selected Galaxies

Success Rate of Identifying Lensing Systems in Near-IR: Out of the current sample of 87 candidate lensing systems, 15 have definitive features of lensing and are highly prioritized for analysis, with nine, one, three, and two having existing redshifts for both foreground lens and background source (Grade A1), the background source (Grade A2), the foreground lens (Grade A3), and neither (Grade A4), respectively. We find that the Grade A sources typically have larger $500\ \mu\text{m}$ flux densities (median $S_{500} \sim 120\ \text{mJy}$) than their lower priority counterparts, with median $S_{500} \sim 90$ and $80\ \text{mJy}$ for Grade B and C sources, respectively. This is expected from the selection method, since galaxies with larger sub-mm flux densities have a higher probability of being lensed. We find that 32% of the sources with $S_{500} \geq 100\ \text{mJy}$ are classified as Grade A, demonstrating a lower success rate in identifying strong lensing events than spatially resolved sub-mm studies of *Herschel* SMGs (Bussmann et al., 2013, $\sim 80\%$). This is likely due to the rest-frame optical emission suffering heavy dust-obscuration, as well as the varying depth in our observations, being significantly spatially offset from regions of high-magnification in the source plane, or because *Herschel*-selected SMGs are typically at high redshift.

Magnifications and Intrinsic Sizes: We generate lens models for 12 Grade A systems to derive near-IR magnification factors and reconstruct the morphologies of SMGs. Our lensed SMGs have an average magnification factor of $\mu_{\text{NIR}} = 7 \pm 3$ and typically have rest-frame emission that extends out to angular sizes of $0.3''$, which is $\sim 2\ \text{kpc}$ at $z \geq 1$. For sources with multiple components, we calculate an upper limit of $0.02''$ ($0.2\ \text{kpc}$ at $z \geq 1$) for the size of substructures within the background galaxy. These angular sizes have been measured as lower limits from previous studies of the unlensed SMGs. While these smaller angular sizes could represent the typical size scales for this galaxy population, it could also be due to the lensing of a subregion that is located near areas of high magnification in the source plane.

Comparison with the Sub-mm: For the subset of sources that overlap with Bussmann et al. (2013), we derive near-IR magnification factors using foreground lens parameters derived in the sub-mm. Differential lensing is observed in all cases, with $\mu_{\text{NIR}} = \mu_{880}/1.5$, typically. A size comparison reveals that the near-IR background source models are generally $2\times$ more extended than their sub-mm counterparts in the same galaxies. This indicates that the lensed stellar emission regions in SMGs are typically more extended than the lensed dust emission regions, in the same galaxies.

Rest-frame Optical Flux: The rest-frame absolute B -band magnitude values and $500\ \mu\text{m}$ flux densities, both corrected for magnification, show that the lensed SMGs are intrinsically similar to unlensed SMGs from previous studies, but with our sources typically at the fainter end of the distribution.

5.1.3 The Rest-Frame UV Emission of HFLS3

Invalidation of HFLS3 Counterpart: The recently acquired *Hubble*/WFC3 and ACS imaging data show conclusively that the previously identified rest-frame optical counterpart of HFLS3 is at $z < 6$.

Lensing Model of HFLS3: We find two galaxies in the foreground leading, to a clear possibility for lensing magnification, though at a level below that needed to form multiple images. A lensing model based on the *Hubble* imaging data then leads to a magnification factor for the mm-wave continuum emission of 2.2 ± 0.3 , with a strict upper limit of 3.7 at the 95% confidence level. The scenario involving no lensing is ruled out at more than $6\ \sigma$ confidence level.

Intrinsic Properties of HFLS3: Using models for the rest-frame UV to far-IR spectral energy distribution we determine the instantaneous SFR, 100 Myr-averaged SFR, dust, and

stellar masses of HFLS3 to be $1320 M_{\odot} \text{ yr}^{-1}$, $660 M_{\odot} \text{ yr}^{-1}$, $3 \times 10^8 M_{\odot}$, and $2 \times 10^{11} M_{\odot}$, respectively, with large uncertainties especially on the stellar mass of HFLS3. The properties of HFLS3 suggest a galaxy that has intrinsic properties that are roughly consistent with $z = 5.3$ SMG AzTEC-3, but there are also differences resulting from the higher dust and stellar mass of HFLS3.

5.2 Future Studies:

The far-IR observations of *Herschel* have provided significant contributions in our overall knowledge of the dusty star-forming galaxy population at high redshift. During five years it was operational, *Herschel* has mapped over 1200 deg^2 of the sky and has paved the way for detailed follow-up observations for existing and new facilities. Although we have gained a better understanding of the Universe during the peak of star-formation, there are many questions that remain unresolved and will dictate the focus of future research. For example:

What is the total dust-enshrouded star-formation rate? The current samples of dusty star-forming galaxies have been subject to different selection effects that can under or overestimate their contribution in the cosmic star-formation history. For instance, the mid-IR selection in DOGs are biased to detecting a subset of $24 \mu\text{m}$ bright ULIRGs with a significant amount of hot dust and SMGs are biased to detecting galaxies that are cold dust-dominated. Therefore, a large, complete, luminosity limited sample of dusty star-forming galaxies at each epoch needs to be assembled in order to constrain the total contribution of dust enshrouded star-formation and compare this to optically selected galaxies. Furthermore, *Herschel*-SPIRE has only resolved $\sim 10\%$ of the cosmic IR background at 350 and $500 \mu\text{m}$ into individual galaxies while indirect methods such as gravitational lensing and stacking suggest that the fainter population comprise $\sim 80\%$. This could either be due to intrinsically far-infrared faint galaxies at low redshift or star-forming galaxies at very high redshift. In

any case, spatially resolved observations of this fainter population is necessary in order to accurately determine the major contributors to the cosmic infrared background, hence the dust enshrouded star-formation.

How are all the high-redshift galaxy populations related? Different galaxy populations are usually identified in different wavelength regimes in order to isolate specific properties. For example, sources that are X-ray bright or display a power-law continuum in the mid-IR are selected as galaxies that host an AGN. Selection criteria in the optical and the infrared regimes typically use colors to indicate star-formation activity in a galaxy or if it is evolving passively. Although we have expanded the known information about the properties of different galaxy populations, how exactly they are related to each other still remains to be determined. The idea that the galaxies we observe locally are comprised mostly spirals and ellipticals suggest that these galaxies follow similar evolutionary paths. If each high-redshift galaxy population is believed to represent a unique stage of evolution, then we need to accurately determine the timescales of these phases. This can then be compared to the observed overlapping fractions of these galaxy populations, e.g. the number of DOGs that are SMGs or SMGs that are DOGs, and help determine a consistent picture of how galaxies evolve. With the next generation of instruments that offer unprecedented detail and sensitivity at all wavelength regimes, such a census of high-redshift galaxies will certainly be possible.

What is the physical mechanism driving star-formation in dusty galaxies in the early Universe? The morphologies of SMGs can give important clues to answer this question. Our study of of lensed SMGs show a variety of derived morphologies for the background source, which range from being modeled as single component extended ellipsoids or having multiple components that resemble major mergers or merger remnants. This supports the idea that SMGs stem from different formation mechanisms in contrast to the popular result that they are mainly from gas rich major mergers. Observations of CO gas in

SMGs have shown rotationally supported clumpy galaxies with undisturbed gas kinematics, which also suggest the need for an alternative scenario other than mergers.

The future of studying dusty star-forming galaxies looks very promising with the next generation of facilities designed specifically to probe the birth and evolution of galaxies. The scientific breakthroughs these instruments will make in the next coming years will be numerous and here their capabilities are briefly described.

The Atacama Large Millimeter Array (ALMA) at the Atacama Desert in northern Chile, which has recently completed its first set of science observations (Cycle 0) and already making ground breaking discoveries, can effectively observe at $420\ \mu\text{m}$ to $3.6\ \text{mm}$. The full capabilities of ALMA will have all 45 antennae available with full access to compact and extended array configurations. The maximum spatial resolution achieved with the next cycle of observations are predicted to reach $0.09''$ in the shortest wavelengths and $0.4''$ in the longest wavelengths. At high redshift, ALMA will be able to identify SMG counterparts unambiguously and resolve the most compact star-forming regions in sub-mm and mm bright galaxies at physical scales as small as $80\ \text{pc}$. Its unparalleled sensitivity will be able to detect molecular gas allowing detailed studies of the spatial distribution and kinematics of dusty star-forming galaxies.

The Cerro Chajnantor Atacama Telescope (CCAT) is ground based 25 meter telescope which will be situated on Cerro Chajnantor in Northern Chile at an altitude of 5612 meters, allowing it to perform effectively at sub-mm wavelengths ($200\text{-}2200\ \mu\text{m}$). The CCAT is a telescope designed to compliment ALMA observations and features $3.5''$ spatial resolution and a one degree field of view. Its instruments are expected to map out the sub-mm sky 1000 times faster than SCUBA-2 instrument mounted on the JCMT, which will make it ideal to perform deep wide area sub-mm surveys and quickly recover large samples of high-redshift dusty star-forming galaxies.

At optical to mid-IR wavelengths, the Thirty-Meter Telescope (TMT) promises to be the largest, most advanced and powerful telescope ever constructed. As its name implies, the TMT will have a 30 m primary mirror composed of 492 segments which boasts a light collection area that is 10 times larger than the Keck telescopes. In order to achieve the best possible spatial resolution, the TMT will also have adaptive optics to correct for the blurring effects of the Earth's atmosphere. For instance, the TMT is expected to reach spatial resolutions of $0.015''$ at $2.2\ \mu\text{m}$, which is a factor of 10 better than HST.

The Japanese-team led SPace Infrared telescope for Cosmology and Astrophysics (SPICA) is the front runner to become the next generation space-based telescope to observe in the mid to far-IR ($5 - 200\ \mu\text{m}$) and built to bridge the gap between near-IR and sub-mm instruments. SPICA features a 3.5 meter telescope which is cryogenically cooled down to temperatures of 5 K, which is designed to achieve spatially-resolved background limited observations from the mid to far-IR. Furthermore, SPICA is a significant upgrade over *Herschel*-PACS and boasts to be 100 times more sensitive in the far-IR.

Finally, the highly anticipated James Webb Space Telescope (JWST), widely believed to be the successor of the HST and *Spitzer*, is expected to launch in 2018. It features a foldable, gold-coated 6.5 meter primary mirror, which is almost three times larger than HST's. The wavelength coverage of JWST will be in the near to mid-IR ($0.6 - 27\ \mu\text{m}$) regimes and is expected to achieve $\sim 0.1''$ spatial resolution even at its longest wavebands. Therefore, JWST is expected to detect, resolve and characterize the faintest, smallest, and dust-obscured star-forming galaxies at the highest redshifts.

Bibliography

- Abazajian, K., et al. 2003, *AJ*, 126, 2081
- Adelberger, K. L., & Steidel, C. C. 2000, *ApJ*, 544, 218
- Aguirre, P., Baker, A. J., Menanteau, F., Lutz, D., & Tacconi, L. J. 2013, *ApJ*, 768, 164
- Alexander, D. M., et al. 2003, *AJ*, 125, 383
- Barger, A. J., Cowie, L. L., Sanders, D. B., Fulton, E., Taniguchi, Y., Sato, Y., Kawara, K., & Okuda, H. 1998, *Nature*, 394, 248
- B  thermin, M., Dole, H., Beelen, A., & Aussel, H. 2010, *A&A*, 512, A78
- B  thermin, M., et al. 2012, *A&A*, 542, A58
- Biggs, A. D., & Ivison, R. J. 2008, *MNRAS*, 385, 893
- Blain, A. W. 1996, *MNRAS*, 283, 1340
- Blain, A. W., Chapman, S. C., Smail, I., & Ivison, R. 2004a, *ApJ*, 611, 52
- . 2004b, *ApJ*, 611, 725
- Blain, A. W., Kneib, J.-P., Ivison, R. J., & Smail, I. 1999, *ApJL*, 512, L87
- Blain, A. W., Smail, I., Ivison, R. J., Kneib, J.-P., & Frayer, D. T. 2002, *Phys. Rept.*, 369, 111
- Bolzonella, M., Miralles, J.-M., & Pell  , R. 2000, *A&A*, 363, 476
- Borys, C., et al. 2006, *ApJ*, 636, 134
- Bothwell, M. S., et al. 2013, *MNRAS*, 429, 3047
- Bouwens, R. J., et al. 2004, *ApJL*, 606, L25
- Brand, K., et al. 2006, *ApJ*, 644, 143
- Brodwin, M., et al. 2008, *ApJL*, 687, L65
- Bruzual, G., & Charlot, S. 2003, *MNRAS*, 344, 1000

Burgarella, D., et al. 2013, *A&A*, 554, A70

Bussmann, R. S., et al. 2009a, *ApJ*, 693, 750

— . 2009b, *ApJ*, 705, 184

— . 2011, *ApJ*, 733, 21

— . 2012, *ApJ*, 744, 150

— . 2013, ArXiv e-prints

Calanog, J. A., et al. 2013, *ApJ*, 775, 61

Calzetti, D., Armus, L., Bohlin, R. C., Kinney, A. L., Koornneef, J., & Storchi-Bergmann, T. 2000, *ApJ*, 533, 682

Capak, P., et al. 2007, *ApJS*, 172, 99

Capak, P. L., et al. 2011, *Nature*, 470, 233

Caputi, K. I., et al. 2007, *ApJ*, 660, 97

Casey, C. M., Chapman, S. C., Smail, I., Alaghband-Zadeh, S., Bothwell, M. S., & Swinbank, A. M. 2011, *MNRAS*, 411, 2739

Casey, C. M., Narayanan, D., & Cooray, A. 2014, ArXiv e-prints

Casey, C. M., et al. 2009, *MNRAS*, 399, 121

— . 2013, *MNRAS*, 436, 1919

Chabrier, G. 2003, *ApJL*, 586, L133

Chapin, E. L., et al. 2009, *MNRAS*, 398, 1793

— . 2011, *MNRAS*, 411, 505

Chapman, S. C., Blain, A. W., Smail, I., & Ivison, R. J. 2005, *ApJ*, 622, 772

Chapman, S. C., Smail, I., Blain, A. W., & Ivison, R. J. 2004, *ApJ*, 614, 671

Chapman, S. C., Windhorst, R., Odewahn, S., Yan, H., & Conselice, C. 2003, *ApJ*, 599, 92

Chary, R., & Elbaz, D. 2001, *ApJ*, 556, 562

Clements, D. L., et al. 2010, *A&A*, 518, L8

Combes, F., et al. 2012, *A&A*, 538, L4

Condon, J. J. 1992, *ARA&A*, 30, 575

- Condon, J. J., Cotton, W. D., Greisen, E. W., Yin, Q. F., Perley, R. A., Taylor, G. B., & Broderick, J. J. 1998, *AJ*, 115, 1693
- Cooray, A., et al. 2011, ArXiv e-prints
- . 2014, ArXiv e-prints
- Coppin, K., et al. 2010, *ApJ*, 713, 503
- Cox, P., et al. 2011, *ApJ*, 740, 63
- da Cunha, E., Charlot, S., & Elbaz, D. 2008, *MNRAS*, 388, 1595
- Daddi, E., et al. 2007, *ApJ*, 670, 156
- . 2009, *ApJ*, 694, 1517
- Dai, Y. S., et al. 2012, *ApJ*, 753, 33
- Damjanov, I., et al. 2009, *ApJ*, 695, 101
- Davé, R., Finlator, K., Oppenheimer, B. D., Fardal, M., Katz, N., Kereš, D., & Weinberg, D. H. 2010, *MNRAS*, 404, 1355
- Dekel, A., Sari, R., & Ceverino, D. 2009, *ApJ*, 703, 785
- Desai, V., et al. 2009, *ApJ*, 700, 1190
- Devlin, M. J., et al. 2004, in *Society of Photo-Optical Instrumentation Engineers (SPIE) Conference Series*, Vol. 5498, *Z-Spec: a broadband millimeter-wave grating spectrometer: design, construction, and first cryogenic measurements*, ed. C. M. Bradford, P. A. R. Ade, J. E. Aguirre, J. J. Bock, M. Dragovan, L. Duband, L. Earle, J. Glenn, H. Matsuhara, B. J. Naylor, H. T. Nguyen, M. Yun, & J. Zmuidzinas, 42–54
- Dey, A., et al. 2008, *ApJ*, 677, 943
- Diolaiti, E., Bendinelli, O., Bonaccini, D., Close, L., Currie, D., & Parmeggiani, G. 2000, in *Astronomical Society of the Pacific Conference Series*, Vol. 216, *Astronomical Data Analysis Software and Systems IX*, ed. N. Manset, C. Veillet, & D. Crabtree, 623
- Dole, H., et al. 2006, *A&A*, 451, 417
- Donley, J. L., Rieke, G. H., Pérez-González, P. G., Rigby, J. R., & Alonso-Herrero, A. 2007, *ApJ*, 660, 167
- Dowell, C. D., et al. 2014, *ApJ*, 780, 75
- Draine, B. T. 2003a, *ARA&A*, 41, 241
- . 2003b, *ARA&A*, 41, 241
- Driver, S. P., et al. 2009, *Astronomy and Geophysics*, 50, 050000

- Dunne, L., & Eales, S. A. 2001, *MNRAS*, 327, 697
- Dwek, E., et al. 2011, *ApJ*, 738, 36
- Dye, S., et al. 2014, *MNRAS*, 440, 2013
- Eales, S. A., et al. 2010, *A&A*, 518, L23
- Elbaz, D., et al. 2010, *A&A*, 518, L29
- . 2011, *A&A*, 533, A119
- Elvis, M., et al. 1994, *ApJS*, 95, 1
- Engel, H., et al. 2010, *ApJ*, 724, 233
- Farrah, D., Afonso, J., Efstathiou, A., Rowan-Robinson, M., Fox, M., & Clements, D. 2003, *MNRAS*, 343, 585
- Farrah, D., et al. 2006, *ApJL*, 641, L17
- . 2008, *ApJ*, 677, 957
- Fazio, G. G., et al. 2004, *ApJS*, 154, 10
- Finlator, K., Davé, R., Papovich, C., & Hernquist, L. 2006, *ApJ*, 639, 672
- Fiore, F., et al. 2008, *ApJ*, 672, 94
- . 2009, *ApJ*, 693, 447
- Fixsen, D. J., Dwek, E., Mather, J. C., Bennett, C. L., & Shafer, R. A. 1998, *ApJ*, 508, 123
- Fruchter, A. S., & et al. 2010, in 2010 Space Telescope Science Institute Calibration Workshop, p. 382-387, 382–387
- Fu, H., et al. 2010, *ApJ*, 722, 653
- . 2012, *ApJ*, 753, 134
- . 2013, *Nature*, 498, 338
- Gavazzi, R., et al. 2011, *ApJ*, 738, 125
- Geach, J. E., Smail, I., Chapman, S. C., Alexander, D. M., Blain, A. W., Stott, J. P., & Ivison, R. J. 2007, *ApJL*, 655, L9
- Genzel, R., Tacconi, L. J., Rigopoulou, D., Lutz, D., & Tecza, M. 2001, *ApJ*, 563, 527
- George, R. D., et al. 2013, *MNRAS*, 436, L99
- Greve, T. R., et al. 2005, *MNRAS*, 359, 1165

Griffin, M. J., et al. 2010, *A&A*, 518, L3

Hainline, L. J., Blain, A. W., Smail, I., Alexander, D. M., Armus, L., Chapman, S. C., & Ivison, R. J. 2011, *ApJ*, 740, 96

Harris, A. I., et al. 2012, *ApJ*, 752, 152

Hatziminaoglou, E., et al. 2010, *A&A*, 518, L33

Hauser, M. G., et al. 1998, *ApJ*, 508, 25

Hernán-Caballero, A., et al. 2009, *MNRAS*, 395, 1695

Hezaveh, Y. D., Marrone, D. P., & Holder, G. P. 2012, *ApJ*, 761, 20

Hezaveh, Y. D., et al. 2013, *ApJ*, 767, 132

Hickox, R. C., et al. 2012, *MNRAS*, 421, 284

Hildebrand, R. H. 1983, *QJRAS*, 24, 267

Hinshaw, G., et al. 2013, *ApJS*, 208, 19

Hodge, J. A., et al. 2013, *ApJ*, 768, 91

Hogg, D. W., Baldry, I. K., Blanton, M. R., & Eisenstein, D. J. 2002, *ArXiv Astrophysics e-prints*

Holland, W. S., et al. 1999, *MNRAS*, 303, 659

Hopkins, A. M., & Beacom, J. F. 2006, *ApJ*, 651, 142

Hopwood, R., et al. 2011, *ApJL*, 728, L4

Houck, J. R., et al. 2005, *ApJL*, 622, L105

Hughes, D. H., et al. 1998, *Nature*, 394, 241

Ilbert, O., et al. 2009, *ApJ*, 690, 1236

—. 2010, *ApJ*, 709, 644

Indebetouw, R., et al. 2014, *ApJL*, 782, L2

Ivison, R. J., Papadopoulos, P. P., Smail, I., Greve, T. R., Thomson, A. P., Xilouris, E. M., & Chapman, S. C. 2011, *MNRAS*, 412, 1913

Ivison, R. J., et al. 2008, *MNRAS*, 390, 1117

—. 2013, *ApJ*, 772, 137

Keeton, C. R. 2001, *ArXiv Astrophysics e-prints*

Kennicutt, Jr., R. C. 1998, *ApJ*, 498, 541

Kim, S., et al. 2012, *ApJ*, 756, 28

Kirkpatrick, A., et al. 2012, *ApJ*, 759, 139

Kochanek, C. S., Blandford, R. D., Lawrence, C. R., & Narayan, R. 1989, *MNRAS*, 238, 43

Koekemoer, A. M., Fruchter, A. S., Hook, R. N., & Hack, W. 2003, in *HST Calibration Workshop : Hubble after the Installation of the ACS and the NICMOS Cooling System*, ed. S. Arribas, A. Koekemoer, & B. Whitmore, 337

Komiyama, Y., et al. 2003, in *Society of Photo-Optical Instrumentation Engineers (SPIE) Conference Series, Vol. 4841, Society of Photo-Optical Instrumentation Engineers (SPIE) Conference Series*, ed. M. Iye & A. F. M. Moorwood, 152–159

Kormann, R., Schneider, P., & Bartelmann, M. 1994, *A&A*, 284, 285

Kovács, A., Chapman, S. C., Dowell, C. D., Blain, A. W., Ivison, R. J., Smail, I., & Phillips, T. G. 2006, *ApJ*, 650, 592

Lagache, G., Abergel, A., Boulanger, F., & Puget, J.-L. 1998, *A&A*, 333, 709

Lapi, A., Negrello, M., González-Nuevo, J., Cai, Z.-Y., De Zotti, G., & Danese, L. 2012, *ApJ*, 755, 46

Lapi, A., et al. 2011, *ApJ*, 742, 24

Le Flocc'h, E., et al. 2005, *ApJ*, 632, 169

Leitherer, C., & Heckman, T. M. 1995, *ApJS*, 96, 9

Levenson, L., et al. 2010, *MNRAS*, 409, 83

Lilly, S. J., Eales, S. A., Gear, W. K. P., Hammer, F., Le Fèvre, O., Crampton, D., Bond, J. R., & Dunne, L. 1999, *ApJ*, 518, 641

Lilly, S. J., et al. 2007, *ApJS*, 172, 70

Lo Faro, B., et al. 2013, *ApJ*, 762, 108

Lonsdale, C. J., Farrah, D., & Smith, H. E. 2006, *Ultraluminous Infrared Galaxies*, ed. J. W. Mason, 285

Madau, P. 1995, *ApJ*, 441, 18

Madau, P., Pozzetti, L., & Dickinson, M. 1998, *ApJ*, 498, 106

Magdis, G. E., et al. 2010, *MNRAS*, 409, 22

Magliocchetti, M., et al. 2008, *MNRAS*, 383, 1131

Magnelli, B., Elbaz, D., Chary, R. R., Dickinson, M., Le Borgne, D., Frayer, D. T., & Willmer, C. N. A. 2009, *A&A*, 496, 57

Magnelli, B., et al. 2010, *A&A*, 518, L28

—. 2012, *A&A*, 539, A155

Marshall, P. J., et al. 2007, *ApJ*, 671, 1196

Matsuura, M., et al. 2011, *Science*, 333, 1258

Melbourne, J., et al. 2012, *AJ*, 143, 125

Michałowski, M., Hjorth, J., & Watson, D. 2010, *A&A*, 514, A67

Michałowski, M. J., Dunlop, J. S., Cirasuolo, M., Hjorth, J., Hayward, C. C., & Watson, D. 2012a, *A&A*, 541, A85

Michałowski, M. J., et al. 2012b, *MNRAS*, 426, 1845

Mosleh, M., Williams, R. J., Franx, M., & Kriek, M. 2011, *ApJ*, 727, 5

Mullaney, J. R., et al. 2012, *MNRAS*, 419, 95

Narayanan, D., et al. 2010, *MNRAS*, 407, 1701

Negrello, M., Perrotta, F., González-Nuevo, J., Silva, L., de Zotti, G., Granato, G. L., Baccigalupi, C., & Danese, L. 2007, *MNRAS*, 377, 1557

Negrello, M., et al. 2010, *Science*, 330, 800

—. 2014, *MNRAS*, 440, 1999

Nguyen, H. T., et al. 2010, *A&A*, 518, L5

Oesch, P. A., et al. 2010, *ApJL*, 725, L150

Oliver, S. J., et al. 2010, *A&A*, 518, L21

—. 2012, *MNRAS*, 424, 1614

Omont, A., et al. 2013, *A&A*, 551, A115

Oyaizu, H., Lima, M., Cunha, C. E., Lin, H., Frieman, J., & Sheldon, E. S. 2008, *ApJ*, 674, 768

Paciga, G., Scott, D., & Chapin, E. L. 2009, *MNRAS*, 395, 1153

Papovich, C., et al. 2007, *ApJ*, 668, 45

Pascale, E., et al. 2011, *MNRAS*, 415, 911

Peng, C. Y., Ho, L. C., Impey, C. D., & Rix, H.-W. 2002, *AJ*, 124, 266

Penner, K., et al. 2012, ApJ, 759, 28

Pérez-González, P. G., et al. 2005, ApJ, 630, 82

Perrotta, F., Baccigalupi, C., Bartelmann, M., De Zotti, G., & Granato, G. L. 2002, MNRAS, 329, 445

Pilbratt, G. L., et al. 2010, A&A, 518, L1

Planck Collaboration et al. 2013, ArXiv e-prints

Poglitsch, A., et al. 2010, A&A, 518, L2

Polletta, M., et al. 2007, ApJ, 663, 81

Pope, A., et al. 2006, MNRAS, 370, 1185

—. 2008a, ApJ, 675, 1171

—. 2008b, ApJ, 689, 127

Press, W. H., Teukolsky, S. A., Vetterling, W. T., & Flannery, B. P. 1992, Numerical recipes in C. The art of scientific computing

Puget, J.-L., Abergel, A., Bernard, J.-P., Boulanger, F., Burton, W. B., Desert, F.-X., & Hartmann, D. 1996, A&A, 308, L5

Richards, G. T., et al. 2006, ApJS, 166, 470

Riechers, D. A., et al. 2010, ApJL, 720, L131

—. 2011, ApJL, 733, L12

—. 2013, Nature, 496, 329

Rieke, G. H., et al. 2004, ApJS, 154, 25

Rigby, E. E., et al. 2011, MNRAS, 415, 2336

Robson, E. I., et al. 2014, ArXiv e-prints

Rodighiero, G., et al. 2010, A&A, 518, L25

—. 2011, ApJL, 739, L40

Roseboom, I. G., et al. 2010, MNRAS, 409, 48

—. 2012, MNRAS, 419, 2758

Rowan-Robinson, M., et al. 2010, MNRAS, 409, 2

Sajina, A., Yan, L., Armus, L., Choi, P., Fadda, D., Helou, G., & Spoon, H. 2007, ApJ, 664, 713

Salvato, M., et al. 2009, *ApJ*, 690, 1250

Sanders, D. B., Soifer, B. T., Elias, J. H., Madore, B. F., Matthews, K., Neugebauer, G., & Scoville, N. Z. 1988, *ApJ*, 325, 74

Sanders, D. B., et al. 2007, *ApJS*, 172, 86

Santini, P., et al. 2010, *A&A*, 518, L154

Savage, R. S., & Oliver, S. 2007, *ApJ*, 661, 1339

Sawicki, M. 2002, *AJ*, 124, 3050

Schinnerer, E., et al. 2008, *ApJL*, 689, L5

Schlegel, D. J., Finkbeiner, D. P., & Davis, M. 1998, *ApJ*, 500, 525

Schmidt, K.-H. 1978, *Astronomische Nachrichten*, 299, 193

Scott, K. S., et al. 2011, *ApJ*, 733, 29

Scoville, N., et al. 2007, *ApJS*, 172, 1

Serjeant, S. 2012, *MNRAS*, 424, 2429

Sersic, J. L. 1968, *Atlas de galaxias australes*

Simons, D. A., & Tokunaga, A. 2002, *PASP*, 114, 169

Simpson, C., & Eisenhardt, P. 1999, *PASP*, 111, 691

Simpson, J., et al. 2013, *ArXiv e-prints*

Smail, I., Chapman, S. C., Blain, A. W., & Ivison, R. J. 2004, *ApJ*, 616, 71

Smail, I., Ivison, R. J., & Blain, A. W. 1997, *ApJL*, 490, L5

Smail, I., Ivison, R. J., Owen, F. N., Blain, A. W., & Kneib, J.-P. 2000, *ApJ*, 528, 612

Smith, A. J., et al. 2012, *MNRAS*, 419, 377

Springel, V., Di Matteo, T., & Hernquist, L. 2005, *ApJL*, 620, L79

Starikova, S., Berta, S., Franceschini, A., Marchetti, L., Rodighiero, G., Vaccari, M., & Vikhlinin, A. 2012, *ApJ*, 751, 126

Swinbank, A. M., Chapman, S. C., Smail, I., Lindner, C., Borys, C., Blain, A. W., Ivison, R. J., & Lewis, G. F. 2006, *MNRAS*, 371, 465

Swinbank, A. M., Smail, I., Chapman, S. C., Blain, A. W., Ivison, R. J., & Keel, W. C. 2004, *ApJ*, 617, 64

Swinbank, A. M., et al. 2010, *MNRAS*, 405, 234

—. 2014, MNRAS, 438, 1267

Swinyard, B. M., et al. 2010, A&A, 518, L4

Symeonidis, M., et al. 2013, MNRAS, 431, 2317

Tacconi, L. J., et al. 2006, ApJ, 640, 228

—. 2008, ApJ, 680, 246

Takeuchi, T. T., Ishii, T. T., Nozawa, T., Kozasa, T., & Hirashita, H. 2005, MNRAS, 362, 592

Targett, T. A., Dunlop, J. S., McLure, R. J., Best, P. N., Cirasuolo, M., & Almaini, O. 2011, MNRAS, 412, 295

Targett, T. A., et al. 2013, MNRAS, 432, 2012

Toft, S., et al. 2014, ApJ, 782, 68

Treu, T. 2010, ARA&A, 48, 87

Umehata, H., et al. 2014, MNRAS, 440, 3462

Veilleux, S., et al. 2009, ApJS, 182, 628

Vieira, J. D., et al. 2013, Nature, 495, 344

Viero, M. P., et al. 2013, ApJ, 772, 77

Walter, F., et al. 2012, Nature, 486, 233

Wang, L., et al. 2013, ArXiv e-prints

Wardlow, J. L., et al. 2011, MNRAS, 415, 1479

—. 2013, ApJ, 762, 59

Weedman, D. W., Le Floch, E., Higdon, S. J. U., Higdon, J. L., & Houck, J. R. 2006, ApJ, 638, 613

Wei, A., et al. 2009, ApJ, 707, 1201

—. 2013, ApJ, 767, 88

Werner, M. W., et al. 2004, ApJS, 154, 1

Wilson, G., Cowie, L. L., Barger, A. J., & Burke, D. J. 2002, AJ, 124, 1258

Wizinowich, P. L., et al. 2006, PASP, 118, 297

Wyithe, J. S. B., Yan, H., Windhorst, R. A., & Mao, S. 2011, Nature, 469, 181

- Yan, L., et al. 2004, ApJS, 154, 75
- . 2005, ApJ, 628, 604
- . 2007, ApJ, 658, 778
- Younger, J. D., et al. 2007, ApJ, 671, 1531
- . 2008, ApJ, 688, 59
- . 2009, ApJ, 704, 803
- Yun, M. S., et al. 2008, MNRAS, 389, 333
- . 2012, MNRAS, 420, 957

Appendix A

Data Tables and Supplementary Figures

A.1 Data Tables for *Herschel* Lensed Candidates

Table A.1: Summary of High Resolution Data¹

IAU Name	Short Name	Exp. Time Filter= $t_{\text{int}} \times N_{\text{frames}}$	Depth AB mag
1HerMES S250 J002854.0-420457	HELAISS04	$J = 62 \times 4$	$J = 25.8$
1HerMES S250 J002906.3-421420	HELAISS01	$J = 62 \times 4$	$J = 25.4$
1HerMES S250 J003823.7-433705	HELAISS02	$J = 125 \times 4$	$J = 25.7$
1HerMES S250 J021620.0-032520	HXMM26	$K_p = 60 \times 30$	$K_p = 25.6^\alpha$
1HerMES S250 J021632.1-053422	HXMM14	$J = 125 \times 4$	$J = 25.6$
1HerMES S250 J021830.6-053125	HXMM02	$J = 177 \times 4, K_p = 60 \times 18$	$J = 26.3, K_p = 25.6^\alpha$
1HerMES S250 J021836.7-035316	HXMM13	$J = 62 \times 4$	$J = 25.6$
1HerMES S250 J021942.9-052433	HXMM20	$J = 125 \times 4$	$J = 25.6$
1HerMES S250 J022016.6-060144	HXMM01	$J = 62 \times 4, K_s = 80 \times 35$	$J = 25.5, K_s = 25.6$
1HerMES S250 J022021.8-015329	HXMM04	$J = 62 \times 4$	$J = 25.6$
1HerMES S250 J022029.2-064846	HXMM09	$J = 62 \times 4, H = 120 \times 12, K = 80 \times 15$	$J = 25.2, H = 24.8, K = 24.5$
1HerMES S250 J022135.2-062618	HXMM03	$J = 62 \times 4$	$J = 25.4$
1HerMES S250 J022201.7-033340	HXMM11	$K_s = 100 \times 18$	$K_s = 25.6^\alpha$
1HerMES S250 J022205.5-070727	HXMM23	$J = 62 \times 4$	$J = 25.2$
1HerMES S250 J022212.9-070224	HXMM28	$J = 125 \times 4$	$J = 25.6$
1HerMES S250 J022250.8-032414	HXMM22	$J = 62 \times 4$	$J = 25.4$
1HerMES S250 J022515.3-024707	HXMM19	$J = 62 \times 4$	$J = 25.3$
1HerMES S250 J022517.5-044610	HXMM27	$J = 62 \times 4$	$J = 25.6$
1HerMES S250 J022547.9-041750	HXMM05	$J = 62 \times 4$	$J = 25.8$
1HerMES S250 J023006.0-034153	HXMM12	$J = 62 \times 4$	$J = 25.2$
1HerMES S250 J032434.4-292646	HECDFS08	$J = 62 \times 4$	$J = 25.4$
1HerMES S250 J032443.1-282134	HECDFS03	$J = 125 \times 4$	$J = 25.4$
1HerMES S250 J032636.4-270045	HECDFS05	$J = 62 \times 4$	$J = 25.6$
1HerMES S250 J032712.7-285106	HECDFS09	$J = 62 \times 4$	$J = 25.5$
1HerMES S250 J033118.0-272015	HECDFS11	$J = 62 \times 4$	$J = 25.3$

Table A.1 – Continued

IAU Name	Short Name	Exp. Time Filter= $t_{\text{int}} \times N_{\text{frames}}$	Depth AB mag
1HerMES S250 J033210.8-270536	HECDFS04	$J = 62 \times 4$	$J = 26.0$
1HerMES S250 J033732.5-295353	HECDFS02	$J = 177 \times 4$	$J = 26.8$
1HerMES S250 J043340.5-540338	HADFS04	$J = 62 \times 4$	$J = 25.6$
1HerMES S250 J043829.8-541832	HADFS02	$J = 62 \times 4$	$J = 25.7$
1HerMES S250 J044154.0-540351	HADFS01	$J = 62 \times 4$	$J = 25.5$
1HerMES S250 J044946.6-525427	HADFS09	$J = 125 \times 4$	$J = 25.3$
1HerMES S250 J045027.1-524126	HADFS08	$J = 62 \times 4$	$J = 25.1$
1HerMES S250 J045057.6-531654	HADFS03	$J = 62 \times 4$	$J = 25.3$
HATLASJ083051.0+013224	G09v1.97	$K_s = 80 \times 41$	$K_s = 25.5$
HATLASJ084933.4+021443	G09v1.124	$K = 80 \times 17$	$K = 24.5$
HATLASJ084957.6+010712	G09v1.1259	$K_s = 80 \times 30$	$K_s = 25.7$
HATLASJ085358.9+015537	G09v1.40	$K_s = 80 \times 45$	$K_s = 26.2$
HATLASJ090319.6+015636	SDP.301	$K_s = 80 \times 26$	$K_s = 25.7$
HATLASJ090542.1+020734	SDP.127	$K_s = 80 \times 24$	$K_s = 25.4$
HATLASJ091840.8+023047	G09v1.326	$K_s = 80 \times 41$	$K_s = 25.9$
1HerMES S250 J100030.6+024142	HCOSMOS03	$K_s = 80 \times 45$	$K_s = 25.6^\alpha$
1HerMES S250 J100057.1+022010	HCOSMOS02	$J = 177 \times 4, K_s = 80 \times 45$	$J = 26.3, K_s = 25.6^\alpha$
1HerMES S250 J100144.2+025712	HCOSMOS01	$J = 62 \times 4, K_s = 80 \times 23$	$J = 25.4, K_s = 25.6^\alpha$
1HerMES S250 J103330.0+563315	HLock15	$J = 125 \times 4$	$J = 25.5$
1HerMES S250 J103618.5+585456	HLock05	$J = 62 \times 4, K_s = 80 \times 44$	$J = 26.0, K_s = 25.6^\alpha$
1HerMES S250 J103826.6+581543	HLock04	$J = 62 \times 4, H = 120 \times 30, K_s = 80 \times 33$	$J = 25.6, H = 25.5, K_s = 25.2$
1HerMES S250 J103957.8+563120	HLock17	$J = 62 \times 4$	$J = 25.6$
1HerMES S250 J104050.6+560653	HLock02	$J = 62 \times 4$	$J = 25.9$
1HerMES S250 J104140.3+570858	HLock11	$J = 177 \times 4, K_s = 80 \times 40$	$J = 26.4, K_s = 26.1$
1HerMES S250 J104549.2+574512	HLock06	$J = 62 \times 4, K_s = 80 \times 34$	$J = 25.5, K_s = 25.6$

Table A.1 – Continued

IAU Name	Short Name	Exp. Time Filter= $t_{\text{int}} \times N_{\text{frames}}$	Depth AB mag
1HerMES S250 J105551.4+592845	HLock08	$J = 62 \times 4$	$J = 25.7$
1HerMES S250 J105712.2+565458	HLock03	$J = 62 \times 4, K_s = 80 \times 41$	$J = 26.2, K_s = 25.8$
1HerMES S250 J105750.9+573026	HLock01	$J = 62 \times 4, K_p = 64 \times 15, K_s = 80 \times 12$	$J = 25.5, K_p = 25.4, K_s = 25.6^{\alpha}$
1HerMES S250 J110016.3+571736	HLock12	$J = 62 \times 4$	$J = 25.9$
HATLASJ113526.4-014606	G12v2.43	$K_s = 80 \times 26$	$K_s = 26.0$
HATLASJ114638.0-001132	G12v2.30	$K_s = 80 \times 42$	$K_s = 25.3$
HATLASJ115101.8-020024	G12v2.105	$K_s = 80 \times 26$	$K_s = 25.7$
HATLASJ132426.9+284452	NB.v1.43	$H = 120 \times 14, K_s = 80 \times 48$	$H = 25.6, K_s = 26.0$
HATLASJ132630.1+334410	NA.v1.195	$K_s = 80 \times 35$	$K_s = 25.9$
HATLASJ132859.3+292327	NA.v1.177	$K_s = 80 \times 28$	$K_s = 25.9$
HATLASJ133008.3+245900	NB.v1.78	$H = 120 \times 9, K_s = 80 \times 20$	$H = 25.5, K_s = 25.7$
HATLASJ133255.8+342209	NA.v1.267	$K_s = 80 \times 42$	$K_s = 26.4$
HATLASJ141351.9-000026	G15v2.235	$K_s = 80 \times 16$	$K_s = 25.3$
1HerMES S250 J142201.4+533214	HEGS01	$J = 125 \times 4$	$J = 26.1$
HATLASJ142413.9+022303	G15v2.779	$K_s = 80 \times 27$	$K_s = 25.4$
1HerMES S250 J142557.6+332547	HBoötes09	$J = 62 \times 4$	$J = 25.5$
1HerMES S250 J142650.6+332943	HBoötes04	$K_s = 80 \times 36$	$K_s = 25.8$
1HerMES S250 J142748.7+324729	HBoötes11	$K_s = 80 \times 35$	$K_s = 25.4$
1HerMES S250 J142824.0+352620	HBoötes03	$J = 62 \times 4$	$J = 25.6$
1HerMES S250 J142825.7+345547	HBoötes02	$J = 62 \times 4, H = 120 \times 28, K_s = 80 \times 27$	$J = 25.6, H = 25.9, K_s = 25.2$
HATLASJ142935.3-002836	G15v2.19	$H = 120 \times 10, K_s = 80 \times 15$	$H = 25.6, K_s = 25.2$
1HerMES S250 J143204.9+325908	HBoötes10	$K_s = 80 \times 46$	$K_s = 25.3$
1HerMES S250 J143330.7+345439	HBoötes01	$J = 62 \times 4$	$J = 25.5$
1HerMES S250 J143543.5+344743	HBoötes12	$J = 62 \times 4, K_s = 80 \times 36$	$J = 25.5, K_s = 25.9$
1HerMES S250 J143702.0+344635	HBoötes08	$K_s = 80 \times 36$	$K_s = 25.8$

Table A.1 – Continued

IAU Name	Short Name	Exp. Time Filter= $t_{\text{int}} \times N_{\text{frames}}$	Depth AB mag
1HerMES S250 J144015.7+333055	HBoötes13	$K_s = 80 \times 37$	$K_s = 25.9$
1HerMES S250 J144029.8+333845	HBoötes07	$K_s = 80 \times 36$	$K_s = 25.9$
HATLASJ144556.1-004853	G15v2.481	$K_s = 80 \times 34$	$K_s = 26.0$
1HerMES S250 J161331.4+544359	HELAIN01	$J = 125 \times 4$	$J = 25.4$
1HerMES S250 J161334.4+545046	HELAIN04	$K_s = 80 \times 45$	$K_s = 25.6$
1HerMES S250 J170507.6+594056	HFLS07	$J = 62 \times 4$	$J = 25.5$
1HerMES S250 J170607.7+590922	HFLS03	$J = 62 \times 4$	$J = 26.7$
1HerMES S250 J170817.6+582845	HFLS05	$J = 125 \times 4$	$J = 24.5$
1HerMES S250 J171450.9+592634	HFLS02	$J = 62 \times 4$	$J = 25.3$
1HerMES S250 J171544.9+601239	HFLS08	$J = 62 \times 4$	$J = 25.5$
1HerMES S250 J172222.3+582609	HFLS10	$J = 355 \times 4, K_s = 80 \times 18$	$J = 26.5, K_s = 25.1$
1HerMES S250 J172612.0+583743	HFLS01	$J = 177 \times 4$	$J = 25.2$

¹**Notes**— The filters listed are J = HST F110W, H = Keck H-band, K_s = Keck Ks band, K = Keck K-band, and K_p = Keck Kp-band. For exposure time, t_{int} is exposure time per frame and N_{frames} is number of independent frames. The last column lists 5σ point-source depths, calculated using the specifications outlined in Section 3.2.2 and 3.2.3.

^α - Depth calculated using average zero point ($\Delta m_{\text{zpt}} = 0.4$) due to absence of a suitable point source in the frame.

Table A.2: Observed Properties of SMG Lens Candidates²

Name	S_{250} (mJy)	S_{350} (mJy)	S_{500} (mJy)	S_{880} (mJy)	z_{source}	Ref.	z_{lens}	Ref.	Lens Grade
HELAISS04	131	102	58	C4
HELAISS01	129	116	81	B4
HELAISS02	114	101	76	B4
HXMM26	45	56	47	C4
HXMM14	98	98	78	C4
HXMM02	91	122	113	51.9	3.390	R14	1.350	W13	B1
HXMM13	55	88	94	...	4.45 ^α	R14	C2
HXMM20	85	79	67	C4
HXMM01	180	192	131	25.1	2.307	F13,W13	0.654	F13,W13	B1
HXMM04	143	136	93	0.210	W13	C3
HXMM09	127	114	83	0.210	W13	B3
HXMM03	120	131	110	...	2.72 ^α	R14	0.359	O08	B1
HXMM11	106	108	81	...	2.179	W13	C2
HXMM23	137	108	57	C4
HXMM28	27	47	87	C4
HXMM22	97	82	62	C4
HXMM19	43	67	70	B4
HXMM27	0	48	43	C4
HXMM05	105	119	91	...	2.985	R14	B2
HXMM12	102	110	81	C4
HECDFS08	104	67	54	B4
HECDFS03	83	118	113	B4
HECDFS05	155	131	84	A4
HECDFS09	77	66	51	C4
HECDFS11	45	52	42	C4

Table A.2 – Continued

Name	S_{250} (mJy)	S_{350} (mJy)	S_{500} (mJy)	S_{880} (mJy)	z_{source}	Ref.	z_{lens}	Ref.	Lens Grade
HECDFS04	73	86	85	B4
HECDFS02	133	147	122	A4
HADFS04	76	90	72	B4
HADFS02	57	78	75	C4
HADFS01	79	103	92	B4
HADFS09	115	61	24	C4
HADFS08	88	81	50	B4
HADFS03	138	114	73	B4
G09v1.97	260	321	269	86.8	3.634	R14	0.626	B13	B1
G09v1.124	241	292	230	50.0	2.410	H12	0.348	I13	C1
G09v1.1259	90	123	95	B4
G09v1.40	388	381	242	62.2	2.091	H12	A2
SDP.301	83	87	65	B4
SDP.127	119	99	59	B4
G09v1.326	141	175	139	18.6	2.581	H12	B2
HCOSMOS03	82	64	37	...	3.25 ^{α}	R14	C2
HCOSMOS02	71	64	41	...	2.497 ^{α}	R14	C2
HCOSMOS01	91	100	74	0.608	new ^{β}	A3
HLock15	102	87	73	B4
HLock05	71	102	98	...	3.42 ^{α}	R14	0.490	W13	C1
HLock04	190	156	100	32.1	0.610	W13	A3
HLock17	62	82	67	...	3.039 ^{α}	R14	C2
HLock02	53	115	140	C4
HLock11	97	112	80	C4
HLock06	136	127	96	...	2.991	R14	0.200	W13	A1
HLock08	142	119	84	...	1.699 ^{α}	R14	B2

Table A.2 – Continued

Name	S_{250} (mJy)	S_{350} (mJy)	S_{500} (mJy)	S_{880} (mJy)	z_{source}	Ref.	z_{lens}	Ref.	Lens Grade
HLock03	113	146	114	47.0	2.771 ^α	R14	C2
HLock01	402	377	249	52.8	2.956	R11, S11	0.600	O08	A1
HLock12	224	159	79	...	1.651 ^α	R14	0.630	O08	A1
G12v2.43	289	295	216	...	3.127	H12	C2
G12v2.30	289	356	295	...	3.259	H13	1.225	B13	A1
G12v2.105	197	178	110	B4
NB.v1.43	347	377	267	27.0	1.680	G13	0.997	...	A1
NA.v1.195	179	278	265	57.6	2.951	H13	0.786	B13	B1
NA.v1.177	264	310	261	51.8	2.778	K13	B2
NB.v1.78	273	282	214	46.0	3.111	R14	0.428	R14	A1
NA.v1.267	164	186	133	C4
G15v2.235	189	240	198	33.5	2.478	H12	C2
HEGS01	74	98	89	0.530	W13	C3
G15v2.779	115	191	204	90.0	4.243	O13, C11	C2
HBoötes09	69	81	60	...	2.895 ^α	R14	C2
HBoötes04	141	133	94	C4
HBoötes11	103	93	63	C4
HBoötes03	323	243	139	18.4	1.034	B06	1.034	B06	B1
HBoötes02	159	195	156	35.5	2.804	R14	0.414	W13	A1
G15v2.19	778	467	225	...	1.026	M13	0.218	M13	A1
HBoötes10	113	92	57	B4
HBoötes01	158	191	160	61.0	3.274	R14	0.590	W13	C1
HBoötes12	11	52	51	B4
HBoötes08	65	78	67	C4
HBoötes13	112	109	72	B4
HBoötes07	86	88	72	...	4.167 ^α	R14	C2

Table A.2 – Continued

Name	S_{250} (mJy)	S_{350} (mJy)	S_{500} (mJy)	S_{880} (mJy)	z_{source}	Ref.	z_{lens}	Ref.	Lens Grade
G15v2.481	141	157	130	B4
HELAIN01	123	129	88	C4
HELAIN04	80	97	78	C4
HFLS07	115	92	69	C4
HFLS03	98	105	81	0.160	W13	C3
HFLS05	40	75	74	...	4.286	R14	C2
HFLS02	164	148	86	0.560	W13	A3
HFLS08	86	93	67	...	2.264	R14	0.330	O08	A1
HFLS10	52	50	32	C4
HFLS01	107	123	98	C4

²**Notes**—The following lists the reference key for redshifts: W13 = Wardlow et al. (2013); B13 = Bussmann et al. (2013); R14 = Riechers et al. (in prep.), M14 = Messias et al. (in prep.); O13 = Omont et al. (2013); C11 = Cox et al. (2011); H12 = Harris et al. (2012); H14 = Harris et al. (in prep.); I13 = Ivison et al. (2013); R11 = Riechers et al. (2011); S11 = Scott et al. (2011); O08 = Oyaizu et al. (2008); K14 = Krips et al. (in prep.); G13 = George et al. (2013); and B06 = Borys et al. (2006).

The $S_{250}, S_{350}, S_{500}$ are flux densities measured from SPIRE photometry. Typical errors which include confusion and instrumental noise on SPIRE photometry are 7-10 mJy (Smith et al., 2012), which includes both statistical and confusion noise. S_{880} corresponds to the 880 μm flux density measured from SMA. This is only available for sources that overlap with the sample from Bussmann et al. (2013). Typical errors for SMA photometry are 15% of the measured S_{880} value. z_{source} and z_{lens} refers to the redshifts of the background source and foreground lens, respectively. Lens Grade is the priority value assigned to the lensed candidate, discussed in Section 3.3.

^{α} Single line redshift measurement, using CO observations.

^{β} Based on Keck/LRIS observations, Fu et al. (in prep.)

A.2 Lens Models using Sub-mm Parameters

In this section, I describe the lens models shown in Fig. A.1 and summarized in Table A.3 for four sources that also have sub-mm data. We fix their foreground lens parameters to sub-mm derived values (Bussmann et al., 2013) as a test for differential magnification as discussed in Section 3.5.1.

NB.v1.78: The near-IR data is more poorly fit, with $\chi_\nu^2 = 1.08$ compared to $\chi_\nu^2 = 0.77$ for our original solution. The lens model is able to reproduce the configuration demonstrated by the brightest knots, similar to the sub-mm emission. However, it fails to fully account for the extended emission producing the fainter Einstein ring.

HBoötes02: A similar configuration with an incomplete quad can be reproduced using sub-mm foreground lens parameters. However, the position of the northern counter-image is offset by $\sim 0.1''$, which is a significant offset since it is comparable to the size of the NIRC2 PSF. The orientation of the extended component in the source plane compared to the original model is significantly different, offset by $\sim 90^\circ$. This could indicate that the observed configuration of the fainter extended emission in the image plane causes the lens model to be poorly constrained.

G09v1.40: A consistent result compared to our original near-IR model is obtained if we instead model the system using sub-mm foreground lens parameters. We measure a marginally lower magnification ($\mu_{\text{NIR}} = 10.8_{-1.1}^{+0.9}$) but is comparable to the sub-mm magnification value ($\mu_{880} = 15.3 \pm 3.5$).

HLock04: The overall fit is significantly degraded ($\chi_\nu^2 = 1.27$ compared to the original $\chi_\nu^2 = 0.63$) when sub-mm foreground lens parameters are used. However, this is because the larger beam size of the 880 μm image shows a configuration that is less constrained. While the near-IR image shows a clear double arc configuration, the sub-mm image is more ambiguous

and the model from Bussmann et al. (2013) statistically favored the cusp-configuration.

Table A.3: Properties of Background Galaxies Using Sub-mm Lens Parameters

Name	ϵ_s	a_{eff}	μ_{NIR}	χ^2_{ν}
NB.v1.78	$0.11^{+0.04}_{-0.02}$	$0.24^{+0.01}_{-0.01}$	$8.8^{+0.2}_{-0.1}$	1.08
...	$0.09^{+0.03}_{-0.02}$	$0.035^{+0.001}_{-0.001}$
HBoötes02	[0.0]	$0.010^{+0.001}_{-0.001}$	$7.6^{+1}_{-0.4}$	1.75
...	$0.4^{+0.1}_{-0.1}$	$0.33^{+0.05}_{-0.03}$
G09v1.40	$0.51^{+0.03}_{-0.1}$	$0.18^{+0.01}_{-0.01}$	10^{+1}_{-1}	0.63
HLock04	$0.3^{+0.1}_{-0.1}$	$0.38^{+0.04}_{-0.04}$	$4.2^{+0.5}_{-0.2}$	1.27

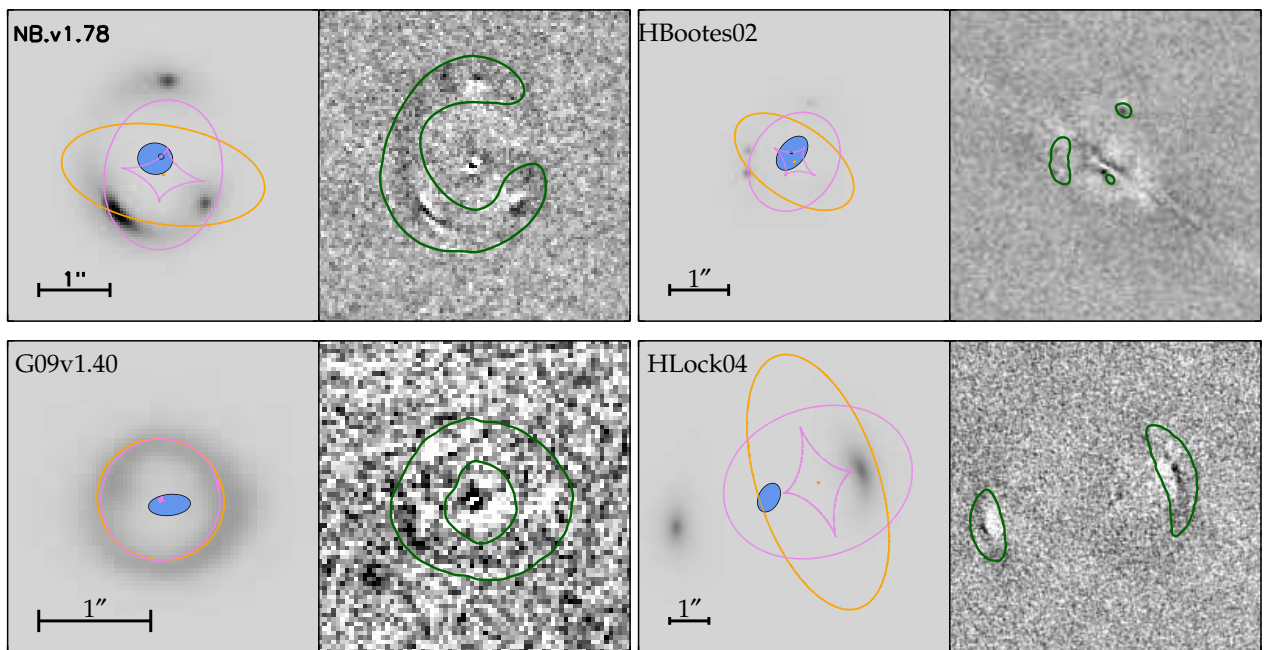


Figure A.1: Lens models of Grade 1 sources with sub-mm data.

The images are displayed at the same scale as their Fig. 3.4 counterparts. North is up and east is left for all the panels. Using the sub-mm lens parameters typically yielded worse fits but was still able to reproduce the observed configurations.

A.3 Supplementary Near-IR Images

In Figures A.2 and A.3 we show high-resolution near-IR images of Grade 2 and 3 sources, respectively. Figure A.4 shows the currently available high-resolution multi-wavelength near-IR data for Grade 1 sources, which we use to measure near-IR photometry.

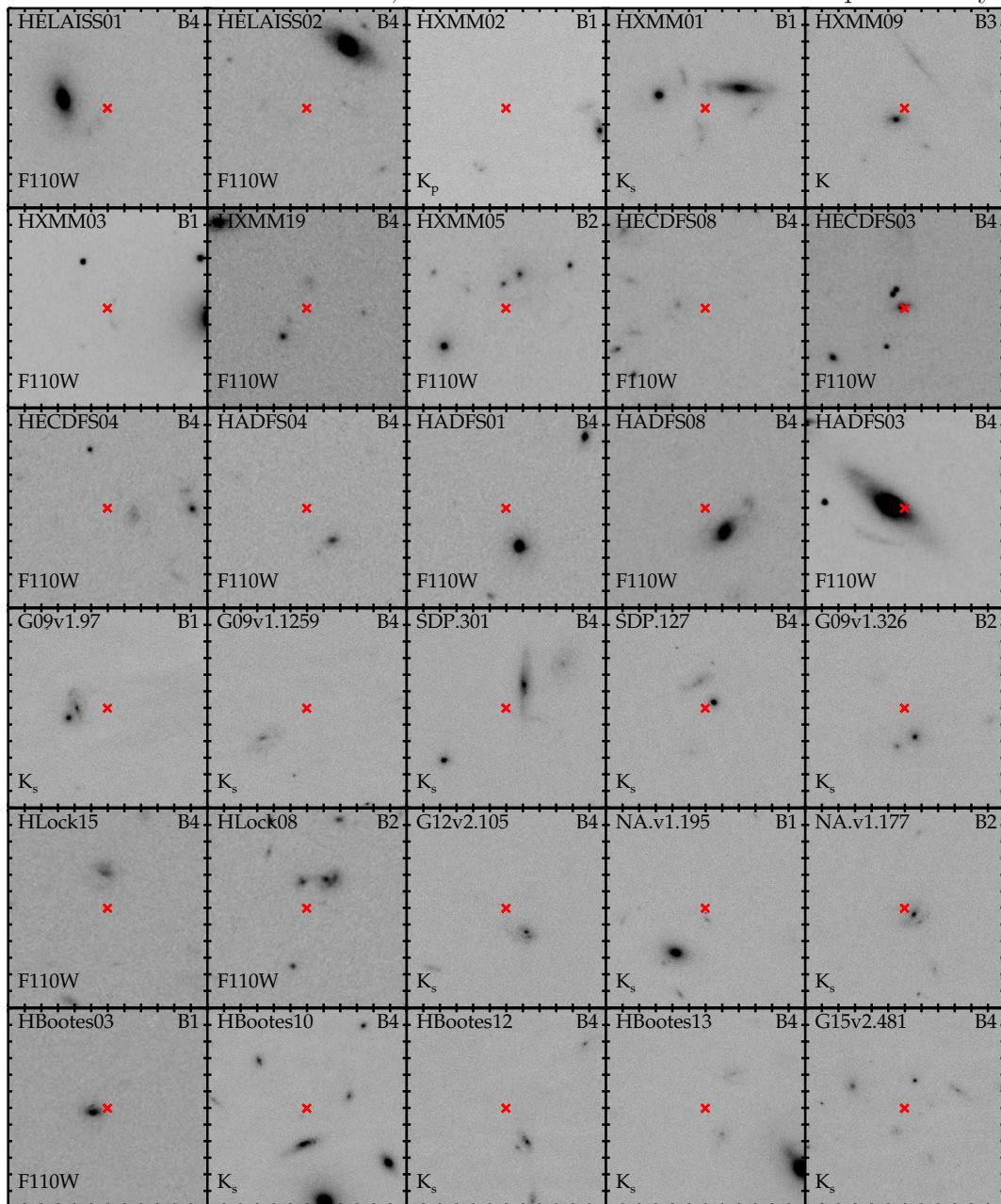


Figure A.2: Near-IR images of Grade 2 sources.

North is up and east is left for all images. Each tick mark is $1''$ and the size of each panel is $12''$. The near-IR band and the complete lens grade are shown in the lower left and upper right corners, respectively. The red \times represents the measured *Herschel* position.

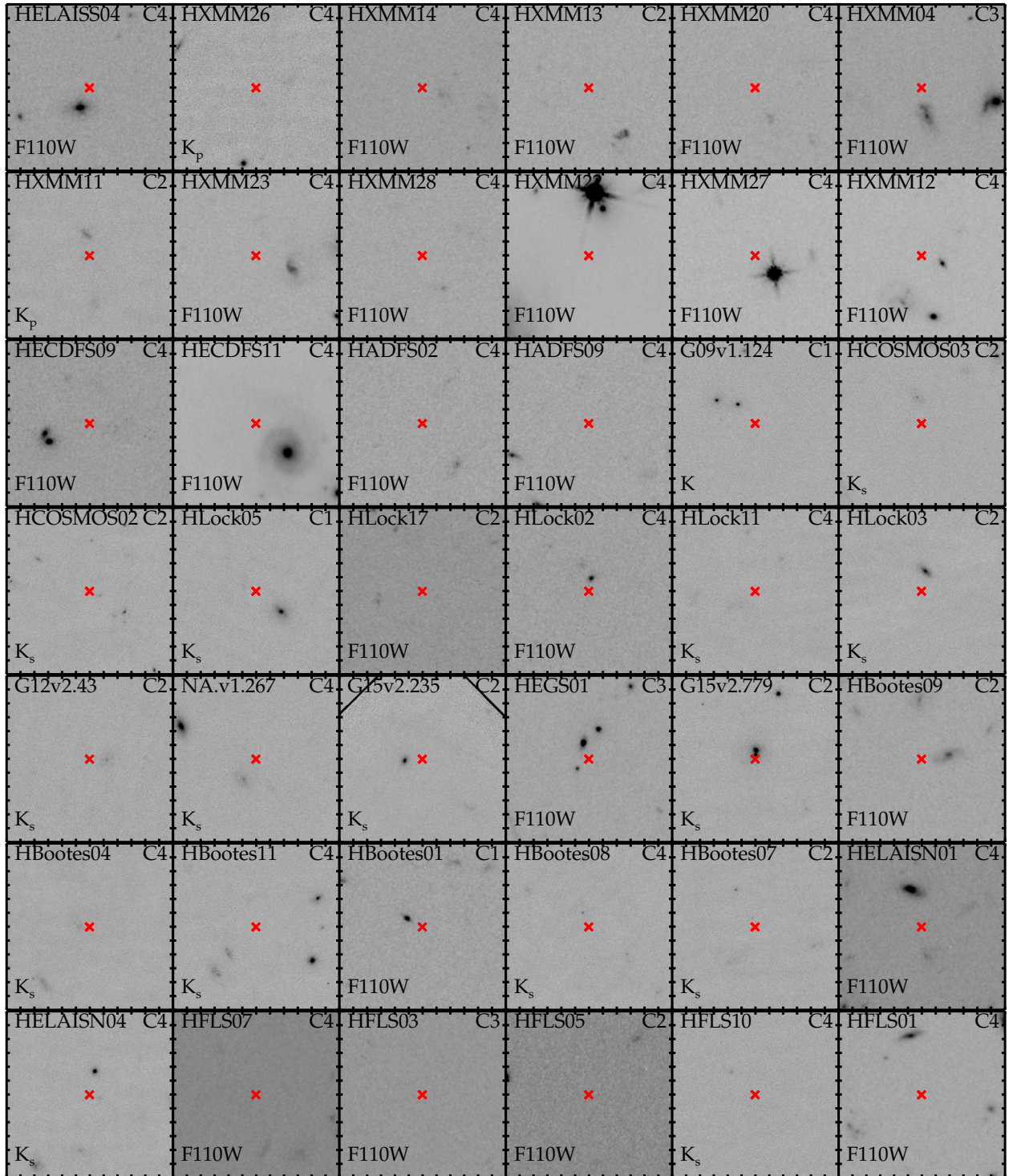


Figure A.3: Near-IR images of Grade 3 sources

North is up and east is left for all images. Each tick mark is $1''$ and the size of each panel is $12''$. The near-IR band and the complete lens grade are shown in the lower left and upper right corners, respectively. The red \times represents the measured *Herschel* position.

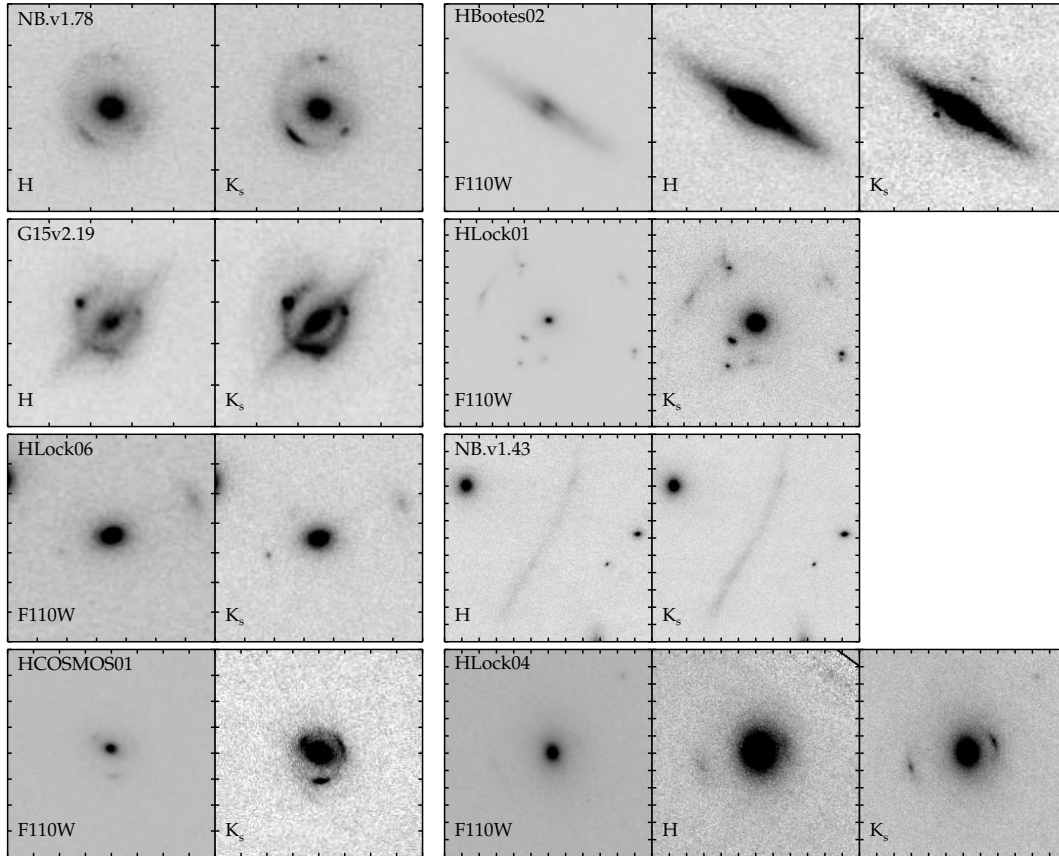


Figure A.4: Multi-wavelength high-resolution near-IR for Grade 1 Lensed SMGs North is up, east is left for all images. The near-IR band is labeled on the lower left corner. Each tick mark represents $1''$. All images are scaled to have consistent brightness units.